Master Thesis

Modeling, Simulation and Failure Analysis of the Natural Circulation System at Ridham Docks

carried out for the purpose of obtaining the degree of Dipl.-Ing., submitted at TU Wien, Faculty of Mechanical and Industrial Engineering, by

Stefan THANHEISER

Mat.Nr.: 9471365

under the supervision of

Univ.Prof. Dipl.-Ing. Dr.techn. Markus HAIDER

Institute of Energy Systems and Thermodynamics, E302

reviewed by

Ao.Univ.Prof. Andreas WERNER

E302

Getreidemarkt 9, 1060 Vienna, Austria

Ao.Univ.Prof. Heimo WALTER

E302

Getreidemarkt 9, 1060 Vienna, Austria

This work was supported by Constructions industrielles de la Méditerranée (CNIM).

I confirm that going to press of this thesis needs the confirmation of the examination committee.

Affidavit

I declare in lieu of oath that I wrote this thesis and performed the associated research myself, using only literature cited in this volume. If text passages from sources are used literally, they are marked as such.

I confirm that this work is original and has not been submitted elsewhere for any examination, nor is it currently under consideration for a thesis elsewhere.

Vienna, March 2017

Signature

Table of Contents

Nomenclature

In general, symbols and their indices are explained where they appear. Some of the units may vary in magnitude (bar might become mbar, etc.) depending on context.

Symbol	Unit	Description
A	m^2	Area
d	m	(Hydraulic) Diameter
e	varying	Error (General)
F	N	Force
f	-	Factor, Fouling Factor
Fr	-	Froude Number
g	$\mathrm{m/s}^2$	Gravitational Acceleration
h	$\mathrm{kJ/kg}$	Specific Enthalpy
h	m	Height, Valve Position
i	-	Index
K	-	Controller Constant
k	$\mathrm{W/m^2K}$	Thermal Transmittance
l	m	Length
M	$\mathrm{g/mol}$	Molar Mass
$\dot{m}$	$\mathrm{kg/s}$	Mass Flow
n	-	Air Excess / Numbering Index (General)
Nu	-	Nusselt Number
P	-	Dimensionless Temperature Change
P , p	bar	Pressure
Pr	-	Prandtl Number
$\dot{Q}$	kW	Heat Flux
$\dot{q}$	$\mathrm{kW/m}^2$	Heat Flux Density
R	-	Total Number of Rows
r	-	Row Number (Index)
Re	-	Reynolds Number
S	varying	Source Term (General)
T	$\mathrm{°C}$	Temperature
t	s	Time
u	varying	Manipulating Variable (General)
v	m^3/kg	Specific Volume
w	$\mathrm{m/s}$	Velocity
w	m	Width
X	varying	Placeholder Variable

Symbol	Unit	Description
X_{H2O}	-	Mass Fraction of Water in Dry Air
x	-	Steam Quality (Mass Fraction of Steam)
α	-	Volume Fraction of Steam
α	W/m^2K	Heat Transfer Coefficient
Γ	kg/s	Mass Flow between Phases
γ	-	Mass Fraction of Fuel Component
Δ	-	Difference (as a Prefix)
δ	-	Equivalent Roughness
ζ	-	Form Loss Coefficient
λ	-	Resistance Coefficient
μ	-	Specific Mass Flow in respect to Fuel Consumption
ν	m^2/s	Kinematic Viscosity
ξ	-	Mass Fraction of Air or Flue Gas Component
π	-	Circular Number
ρ	kg/m^3	Density
φ	deg	Angle
φ	-	Relative Humidity
ψ	-	Void Fraction

Indices are separated by commas when multiple indices are used at the same time.

Index	Description
0	Stoichiometric
$2\,ph$	Two Phase
A	Air, Acceleration, Alignment
add	Additional
amb	Ambient
Ar	Argon (Representative for all Noble Gases)
Ash	Ash
at	Atmosphere
b	Bottom
$BEND$	Pipe Inflection
$bundle$	Bundle as a Whole
C	Carbon
$CO2$	Carbon Dioxide
cr	Critical
d	Dry, Differential
$down$	Down Comer
ECO	Economizer
F	Friction
$Fuel$	Fuel
G	Flue Gas, Gas Node
gas	Gas Phase
geo	Geodesic
H	Static, Hydrogen
h	Horizontal
$H2O$	Water
$hangers$	Hanger Tubes
$HEADER$	Header (Manifold)
i	Interface, Index
in	Entering
k	Phase Indicator
lam	Laminar
liq	Liquid Phase
m	Mean
mix	Water / Steam Mixture
n	Node
nb	Nucleate Boiling

Index	Description
nom	Nominal
N2	Nitrogen
O , *O2*	Oxygen
out	Leaving
p	Pipe, Proportional
Pass3out	Outlet of Third Pass
r	Row
riser	Riser
S	Sulfur
SH	Superheater
SO2	Sulfur Dioxide
sat	Saturated State
single	Single Tube inside a Bundle
sub	Subcooled (below Saturation Temperature)
t	Top
turb	Turbulent
v	Vertical
vap	Vapor
w	Tube Wall
wall	Water Wall
ψ	Void Fraction
$'$	Saturated Liquid
$''$	Saturated Vapor

1 Abstract and Executive Summary

This master thesis investigates the circulation issues that were encountered at a natural circulation steam generator at the Ridham Docks site (England), causing heat damage. The evaporator of the steam generator was modeled in detail and numerically simulated using state of the art calculation software. While no conclusive evidence was found that could explain the damages unambiguously, other instabilities were discovered that may have contributed to the phenomenon. General design guidelines were deducted as possible solutions to the problem.

The damages occurred at a convective evaporator of the steam generator. Investigations identified the cause of the damages to be overheating. Measurements showed increased tube wall temperatures at several locations of the convective evaporator. They only occurred after system startups and also disappeared after another shutdown and restart.

The convective evaporator was modeled with the highest attention to detail; the rest of the evaporator (residual heat exchangers) was modeled with less precision to investigate its influence on the convective part. Model parameters were introduced to investigate different configurations of the model, like different designs of the convective evaporator.

The calculation software Apros was used to simulate the model. It uses a state of the art six equation model, capable of simulating liquid and gas flows separately in an axially discretized network of pipes.

Simulation of the stationary status already revealed flow oscillations in one of the residual heat exchangers. A sudden increase in heat flux can stabilize these oscillations. Integrating that heat exchanger into other parts of the evaporator is likely to suppress the instabilities.

Numerous experiments were conducted with the model. The investigations included uneven heating conditions, pressure variations, heat flux variations in one of the residual heat exchangers, hot startups with different configurations, the influence of foreign objects and the possibility of local flow circulations within the convective evaporator. Except for hot startups, all experiments led to stable systems.

Hot startup experiments showed severe oscillations under specific model configurations. They are illustrated in figure 1.

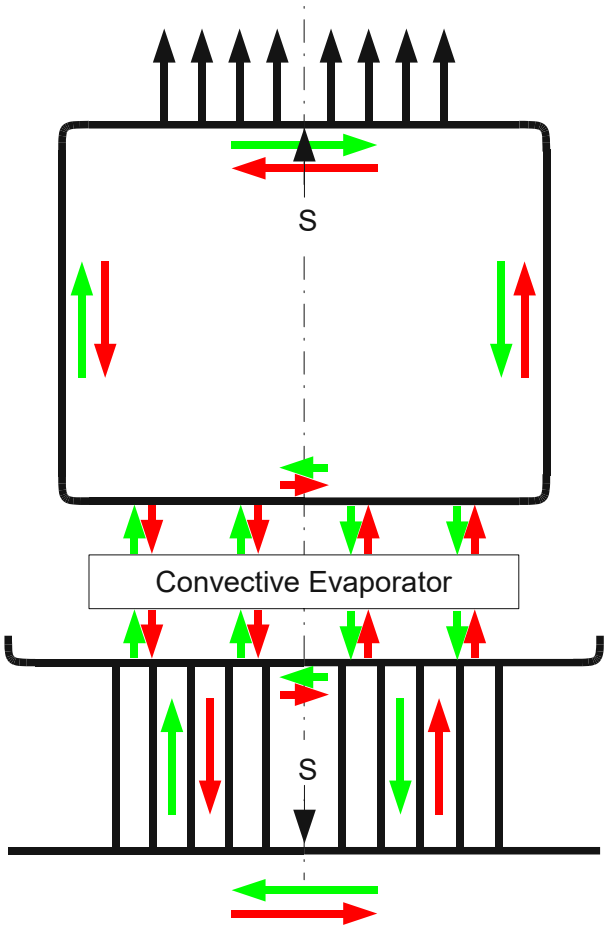

Figure 1: Illustration of the Main Instability encountered

Every color (red / green) represents a possible flow path. During a hot startup, the mass flow starts to oscillate between the two modes when the two sides of the system are not separated at the points marked with S. It could be shown that pressure systems such as the one at the top point of separation generally pose a threat to stability. Simple disks suppressing the mass flows between the sides are a very simple and cost effective way to reliably stop this kind of instability.

However, the only small temperature variations of the tube walls of the convective evaporator during those oscillations do not agree with the temperature excursions that were experienced. They are most likely caused by stratified flow that leaves the top of the tubes poorly cooled. The other oscillations can only contribute to increased fatigue of the tubes. Increased wall temperatures in radial direction of the tubes due to stratification can-not be simulated by the simulation software used which is why it was not possible to conclusively name them as the cause for the temperature excursions. A modified arrangement of the bundle with convective evaporator and hanger tubes in series is likely to suppress stratification and lead to stable tube temperatures.

2 Theoretical Aspects

2.1 Natural Circulation Steam Generators

This section is according to [1] if not marked otherwise. Steam is used in thermal power stations to transform the thermal energy of fuel (coal, biomass, etc.) into rotary energy in a steam turbine, which powers an electrical generator. A simplified cycle of water / steam to produce electricity is illustrated in figure 2.

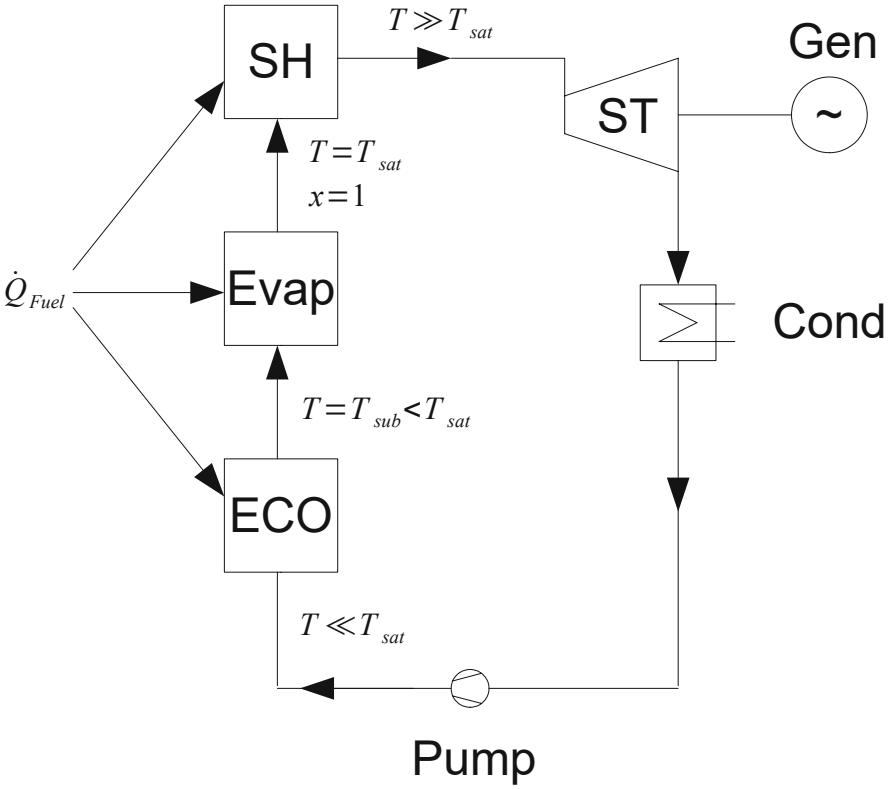

Figure 2: Simplified Water / Steam Cycle in a Thermal Power Station

Cold water is pumped through the economizer (ECO) to be heated to a temperature slightly below the saturation temperature T_{sat} , the so called subcooling temperature T_{sub} . The evaporator (Evap) then heats the liquid to its saturation temperature and produces saturated steam which gets further heated in the superheater (SH). The steam is then expanded in the steam turbine (ST), which is connected to an electrical generator (Gen) by a shaft. The steam leaves the turbine and is liquified in the condenser (Cond), and the cycle starts again. The economizer, evaporator and superheater together form the steam generator. The heat flux into the steam generator derives from the burning of fuel $\dot{Q}_{Fuel}$. The mechanism of heat exchange can be dominated by radiation or convection.

The way the water flows through the steam generator is called its *water side*. The way that hot flue gas produced by burning fuel travels through the steam generator is called the *gas side*, illustrated

in figure 3.

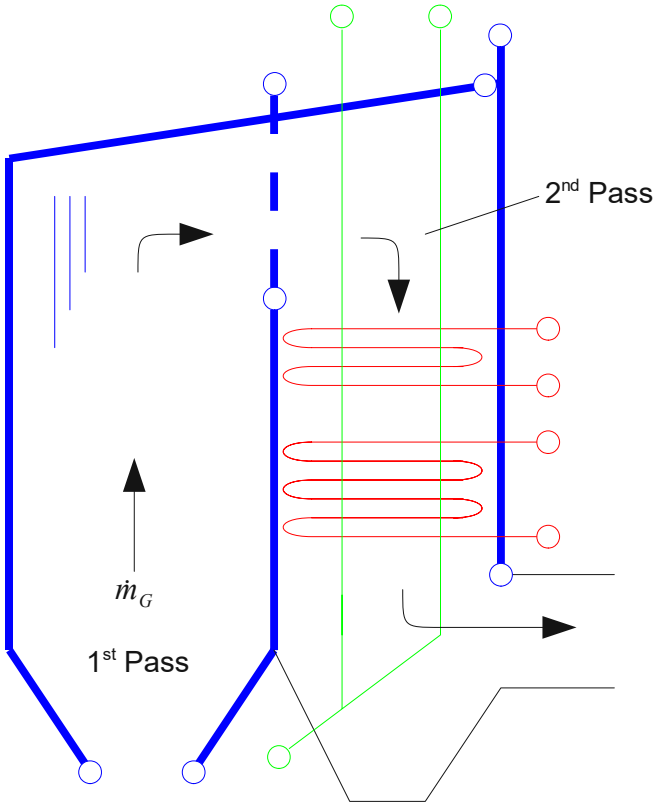

Figure 3: Simple Gas Side of a Steam Generator

The flue gas $\dot{m}_G$ travels through *passes* of the steam generator. They are surrounded by *water walls* (blue lines in figure 3). Water walls are essentially parallel pipes connected with each other, building a gas tight wall. Figure 4 shows a cross section of such a wall. Water walls are part of the evaporator and are therefore fed by preheated water. Between the passes, the pipes of the water wall leave space between them so the flue gas can pass through it, building a *grid* (dashed blue line). Most of the heat flux into the water walls is transferred by radiation, especially in the first pass, where the fuel is burned and the flue gas is the hottest.

Figure 4: Cross Section of a Water Wall [1]

Superheaters and economizers, sometimes also evaporators, are primarily designed as *bundles* of tubes (red structures in figure 3). They consist of many parallel pipes reaching into the pass. The flue gas passing through the bundle heats the fluid inside the pipes via convective heat transfer. The *hanger tubes* (green) carry the weight of the bundle tubes. They can be part of the economizer, evaporator or superheater.

The main focus of this work lies on the evaporator. There are several ways how an evaporator can be operated, one of the most widely used is natural circulation. Figure 5 shows an illustration of the working principle.

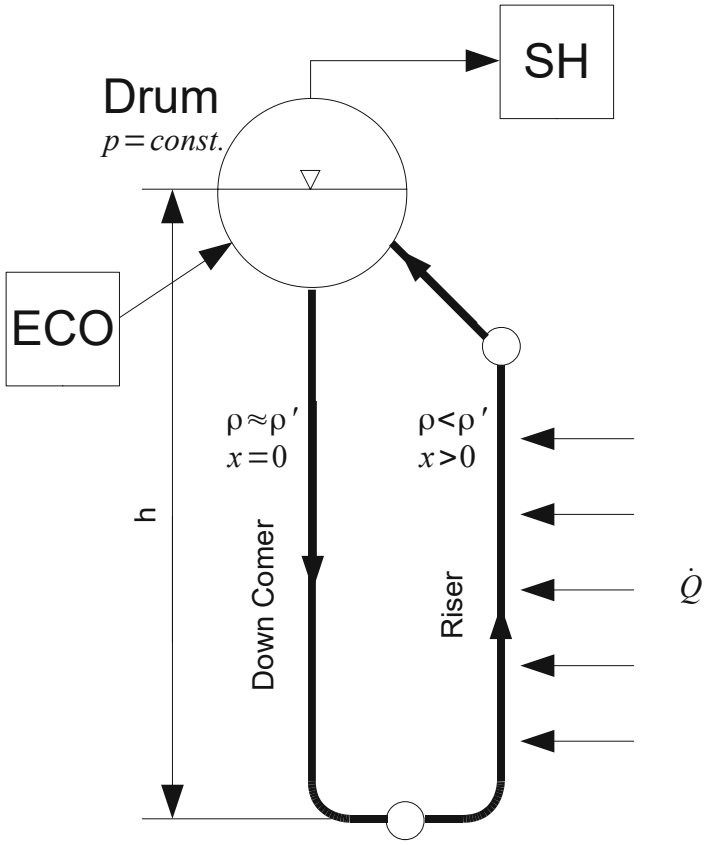

Figure 5: Illustration of Natural Circulation

The most prominent part of a natural circulation system is the steam drum. Its main purpose is the separation of water and steam: subcooled liquid from the economizer leads into it and saturated steam leaves it towards the superheater. In between, the fluid needs to pass through the evaporator. In its simplest form, an evaporator based on natural circulation consists of two parts: an unheated (or only slightly heated) down comer and a heated riser. Risers can be designed as water walls, tube bundles, hanger tubes, etc. Saturated (slightly subcooled) liquid enters the down comer and flows to the bottom of the system. The connection between the down comer and riser is called a *header*. A header is essentially a tube with radially connected smaller tubes. It collects the mass flow of ingoing pipes and distributes it to the outgoing pipes.

After entering the riser, the fluid is heated and partially evaporates. The lower density of the steam compared to the liquid results in a lower (absolute) static pressure difference in the riser:

$$\Delta p_{H,down} = -\rho' \cdot g \cdot h$$

$$\Delta p_{H,riser} = \rho_{mix} \cdot g \cdot h \; < \; |\Delta p_{H,down}|$$

Height differences h are positive when the flow goes upwards. As both the down comer and the riser are connected to the same drum, they both have the same pressure at their boundaries. This means that the sum of all pressure differences from the liquid level of the drum, through the down comer, back up the riser to the liquid level again, has to equal zero:

$$\sum \Delta p = 0$$

Because the static pressure differences are unequal in the down comer and riser due to the different fluid densities, additional dynamic pressure losses have to occur to satisfy the equilibrium:

$$\left(\rho_{mix} - \rho'\right) g\, h + \Delta p_F + \Delta p_A = 0$$

The dynamic pressure losses consist of the ones due to friction Δp_F and acceleration Δp_A. The acceleration pressure loss takes the change of momentum flux of the gas and liquid phases into account [2] and is rather small. The friction pressure loss represents the energy dissipation due to friction between the fluid and the tube wall. In one phase flow it is directly proportional to the square of fluid velocity:

$$\Delta p_F \sim w^2$$

In two phase flow the dependency can be of third order [3]. So, the velocity of the fluid has to be high enough so that the frictional pressure losses (together with the smaller acceleration losses) compensate the discrepancy in static pressure differences between the down comer and the riser. A current through the loop is created “naturally” without the need for pumps.

The difference in static pressure losses is seen as the “driving force” and the dynamic pressure losses as the “resisting force” of the natural circulation system. Since the gravitational acceleration g and the height difference h are constant, the driving force is determined by the difference in fluid densities caused by the heating, which in turn depends on the system pressure, see figure 6.

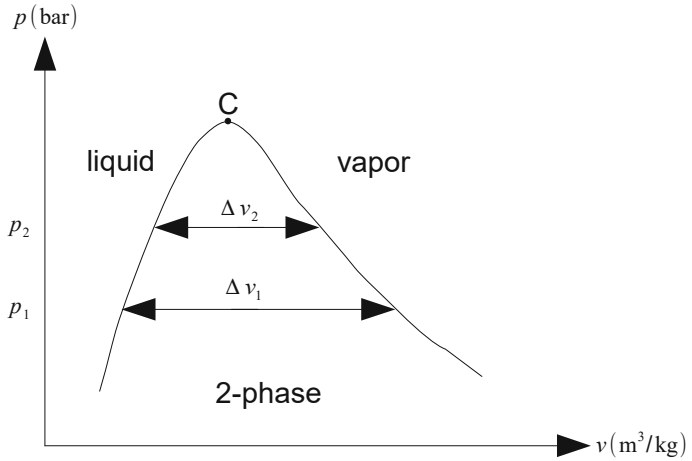

Figure 6: Schematic p-v-Diagram of Water

Figure 6 shows that the difference in density (reciprocal value of specific volume v) between liquid and vapor becomes smaller at higher pressures and vanishes at the critical point C. Because the difference in density between liquid and vapor is the main source for the driving force in a natural circulation system, the physical limit of operation is the critical pressure of about 220 bar. The practical limit lies at 185 bar.

In reality, the design of steam drums is more complicated than the sketch in figure 5 suggests. Although gravity does most of the work, additional installations have to be added to support the separation of water and steam and to ensure that no water drops are carried into the superheaters. Any substance solved in the liquid (salts) would contaminate the inside of the superheater tubes (called scaling) after the water drop evaporated. The solubility of salts in steam is very low. The use of cyclones and demisters is very common for this purpose, as shown in figure 7.

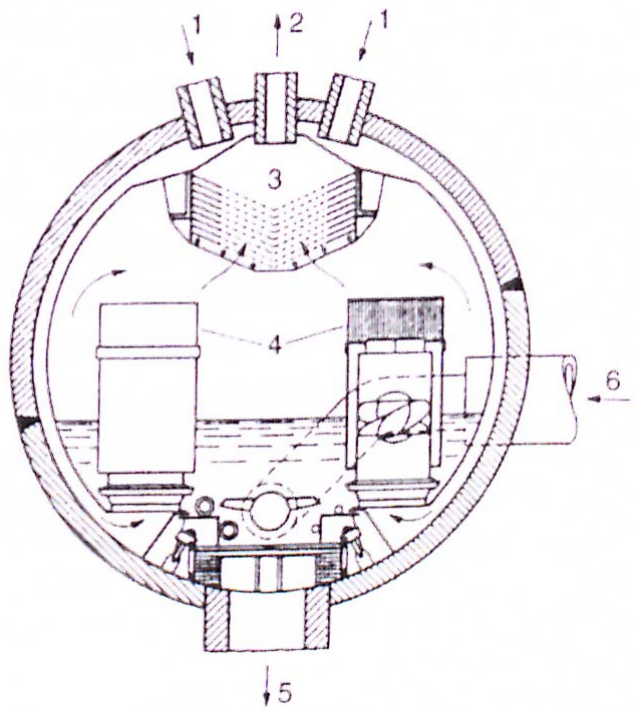

Figure 7: Steam Drum with Installations [1]

Figure 7 shows: *1* additional inlet of water-steam mixture (optional), *2* steam outlet, *3* demister, *4* cyclones, *5* down comer, *6* feed water (from economizer).

The pressure losses inside the cyclones have to be taken into account when calculating the parameters of natural circulation.

2.2 Boiling and Two Phase Flow Regimes

This section is according to [4] if not marked otherwise. When saturated liquid in a tube is heated, it starts to evaporate. Depending on the mass flow and mass (volume) fraction of steam, there are several ways liquid and gas can be distributed inside the tube. These so called *flow regimes* are shown in figure 8 for vertical pipes.

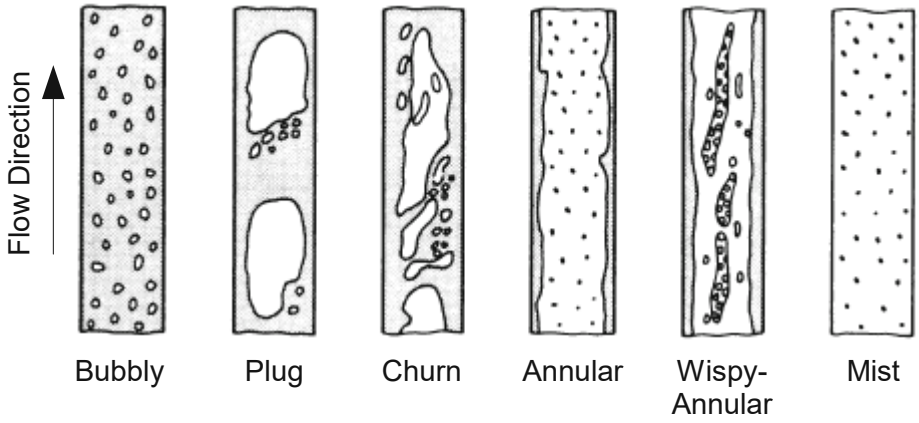

Figure 8: Two Phase Flow Regimes in Vertical Tubes [4]

The heat transfer coefficient between the wall and fluid is very high and equal for all flow regimes with a wetted wall (covered with liquid). Of all the flow regimes shown only the mist-flow does not have a wetted wall. It only occurs at very high steam qualities. So as long as the mass fraction of steam is not too high, the heat transfer is independent of the flow regime, so knowledge of the specific flow regime is not necessarily important.

The situation is different when dealing with horizontal pipes. Here, the influence of gravity can lead to only partially wetted walls at certain flow regimes, see figure 9. At stratified and wavy-stratified flow the fluid phases are separated. All the steam is at the top of the tube while all the liquid remains at the bottom. The problem with that is that the “dry” wall only covered with steam is cooled less efficiently (the heat transfer coefficient between the wall and steam is much lower) compared to the part covered with saturated liquid, which can lead to excessive tube wall temperatures and heat damages. At surge-flow, the liquid and gas phases are separated as well, but the top of the tube is regularly wetted by gushes of liquid, cooling the wall effectively enough to prevent overheating.

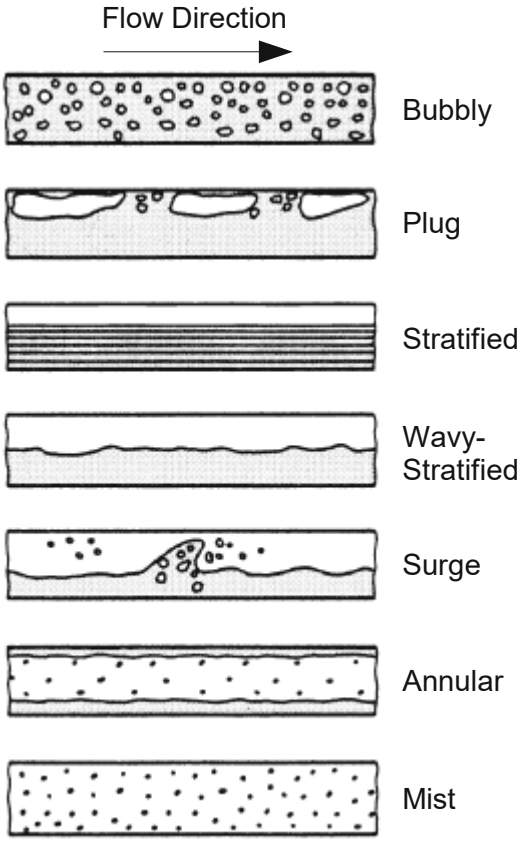

Figure 9: Two Phase Flow Regimes in Horizontal Tubes [4]

The phenomenon when the wall of a heated tube is not wetted during evaporation is called a *boiling crisis*. The much lower heat transfer coefficient between the wall and steam compared to the one between wall and saturated liquid leaves the dry wall inadequately cooled and prone to overheating. There are two mechanisms of boiling crisis in a vertical tube, illustrated in figure 10.

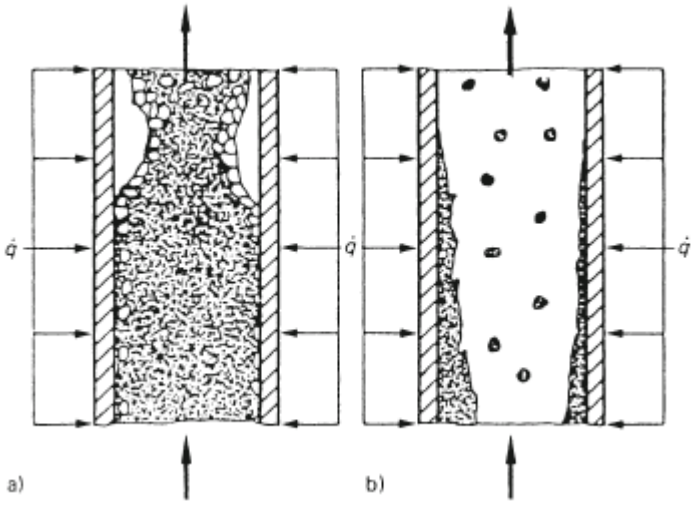

Figure 10: Mechanisms of Boiling Crisis [4]

When the volume fraction of steam is low (left case in figure 10), a layer of steam separates the liquid from the wall. This is called *Departure from Nucleate Boiling (DNB)*. When the volume fraction is high (right case), the remaining layer of liquid (annular flow regime) evaporates and a *Dryout* occurs. A Dryout does not impair the heat transfer as much as a departure from nucleate boiling because the high fraction of steam can still cool the wall via convection. In the case of low specific heat fluxes, liquid droplets can adhere at the wall again, which is then called *Deposition Controlled Burnout*.

The appearance of the respective modes of boiling crisis depends on the heat flux density and the steam mass fraction, shown in figure 11.

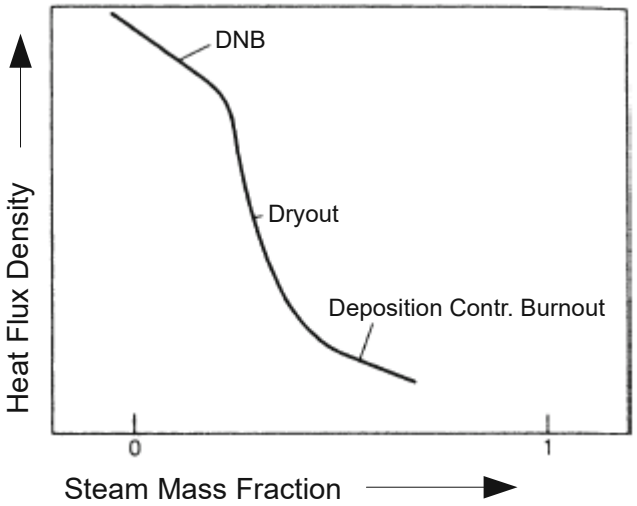

Figure 11: Boiling Crisis Modes at different Heat Flux Densities and Steam Mass Fractions [4]

The line in the graph represents the *critical heat flux* or *critical steam mass fraction* at which boiling crisis occurs when one of them is exceeded. At low mass fractions of steam, boiling crisis leads to a heavy temperature excursion of the tube wall and a destruction of the heat exchanger. The danger becomes less severe at higher mass fractions of steam.

There are several correlations for calculating the critical heat flux and critical steam mass fraction. The one used in this work is from *Katto/Ohno* [5].

For horizontal tubes, the possibility of stratification has to be taken into account. This usually leads to a lower critical steam mass fraction and an earlier onset of boiling crisis at the upper part of the tube. A modified Froude number, putting the inertia of the steam in relation to its buoyancy, can be used to describe stratification in horizontal tubes:

$$\mathrm{Fr} = \frac{\frac{x_{cr}\dot{m}}{\sqrt{\rho''}}}{\sqrt{g\,d\,(\rho' - \rho'')\cos(\varphi)}}$$

Wherein, x_{cr} is the critical steam mass fraction for vertical tubes according to *Katto/Ohno* and ϕ is the angle of the tube to the horizontal. Froude numbers greater than 10 suggest no stratification, whereas, Froude numbers below 3 suggest heavy stratification effects.

The difference in critical steam mass fraction between the top and bottom side of the tube can be calculated using the Froude number from before:

$$\Delta x_{cr} = x_{cr,t} - x_{cr,b} = \frac{16}{(2+\mathrm{Fr})^2}$$

$x_{cr,t}$ and $x_{cr,b}$ are the critical steam mass fractions at the top and bottom of the tube respectively. When regarding x_{cr} as a mean value of the critical steam mass fraction for a horizontal pipe, the critical values at the top and bottom can be calculated as follows:

$$x_{cr,t} = x_{cr} - \frac{\Delta x_{cr}}{2}$$

$$x_{cr,b} = x_{cr} + \frac{\Delta x_{cr}}{2}$$

In general, when boiling crisis occurs due to stratified flow in a horizontal tube, the tube wall temperatures are not increased as much as when boiling crisis occurs in a vertical tube. The reason for this is that a horizontal tube containing stratified flow is still partly wetted (and therefore, properly cooled) at the bottom. Heat conduction between the hot top and cool bottom can limit the temperature excursions at the top of the tube.

2.3 Important Instabilities in Two Phase Natural Circulation Systems

2.3.1 Ledinegg Instability

This section is according to [3]. Ledinegg instabilities are named after the person who first discovered and discussed them. They result from a non-monotonous increase in pressure difference over mass flow (the so called characteristic curve) of a two phase flow in a pipe (generally a flow channel), see figure 12.

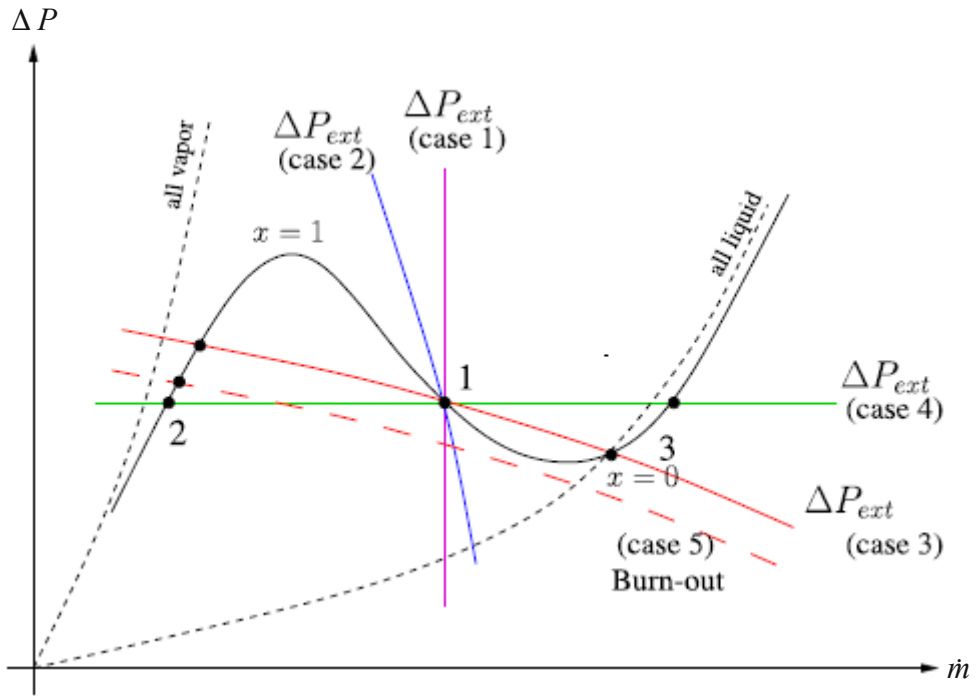

Figure 12: Characteristic Curve of a Two Phase Flow Channel [3]

The “external” curve represents the pressure drop characteristic imprinted by the system, while the “internal” curve shows the pressure drop of the fluid in the flow channel due to gravity, wall friction and change of momentum. The intersection of the two curves marks the steady state operation point. When the mass flow is within the right corridor and the slope of the external curve is greater than the one of the internal curve, more than one intersection between the two curves is possible and the point of operation can change abruptly from one state to another, making the flow unstable.

2.3.2 Density Wave Oscillations

The basic mechanism of density wave oscillations is described in [6] and illustrated in figure 13.

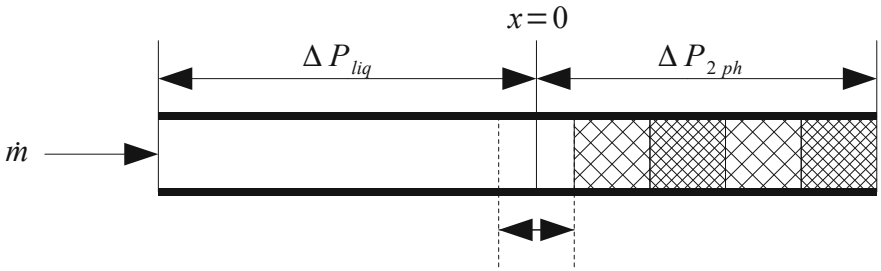

Figure 13: Illustration of Density Wave Oscillations (DWO)

Density Wave Oscillations (DWO) are the result of several feedback systems complementing each other. A perturbation of mass flow at the inlet of a heated tube leads to a shift of the starting point of evaporation. That changes the length of the part of the tube containing two phases and the local steam qualities (illustrated by the rectangular patterns with different density in figure 13). That has an impact on the pressure drop in the two phase region $\Delta P_{2\,ph}$. When the total pressure difference between the inlet and outlet of the tube is constant (as a boundary condition imprinted by the system), the pressure drop in the liquid phase has to adapt to the pressure drop in the two phase region, which in turn has an impact on the mass flow coming into the tube. Because the propagation of disturbances is significantly delayed in the two phase region, the adaptations of mass flow and two phase pressure drop experience a phase shift that can lead to self-induced oscillations.

Density wave oscillations can be classified based on the primarily affected part of the two phase pressure drop [3]: the static part due to the influence of gravity (type I), the frictional part (type II) or the change of momentum (type III). Type I DWOs primarily occur in vertical systems with rather low steam qualities where a long unheated section, a so called chimney, follows the heated section. Such a configuration also promotes *flash induced instabilities* where the static pressure loss induces additional evaporation in the unheated section. The mechanism of propagation and the retroactive influence on mass flow is similar to density wave oscillations.

3 Introduction to the Main Problem

This master thesis was written to fulfill a task assigned to the Technical University of Vienna (TU Vienna) by *Constructions industrielles de la Méditerranée* (CNIM), a French engineering company. CNIM encountered a leak in a convective evaporator in one of their steam generators at the Ridham Docks near Sittingbourne, England, and instructed TU Vienna to examine the circulation system.

The steam generator at the Ridham Docks is part of a combined heat and power plant. It fires about 172 000 tonnes of waste wood per year gathered from the surrounding region, including chipboard, fibreboard, old furniture and wood from building sites and demolished buildings, generating about 188 million kWh of electric energy at a net electrical capacity of 23 MW [7]. The boiler has a thermal capacity of 80 MW and generates 104 tonnes of superheated steam per hour at a temperature of 460 °C and a pressure of 75 bar [8].

The convective evaporator to be investigated is located in the third pass of the steam generator, as highlighted in figure 14.

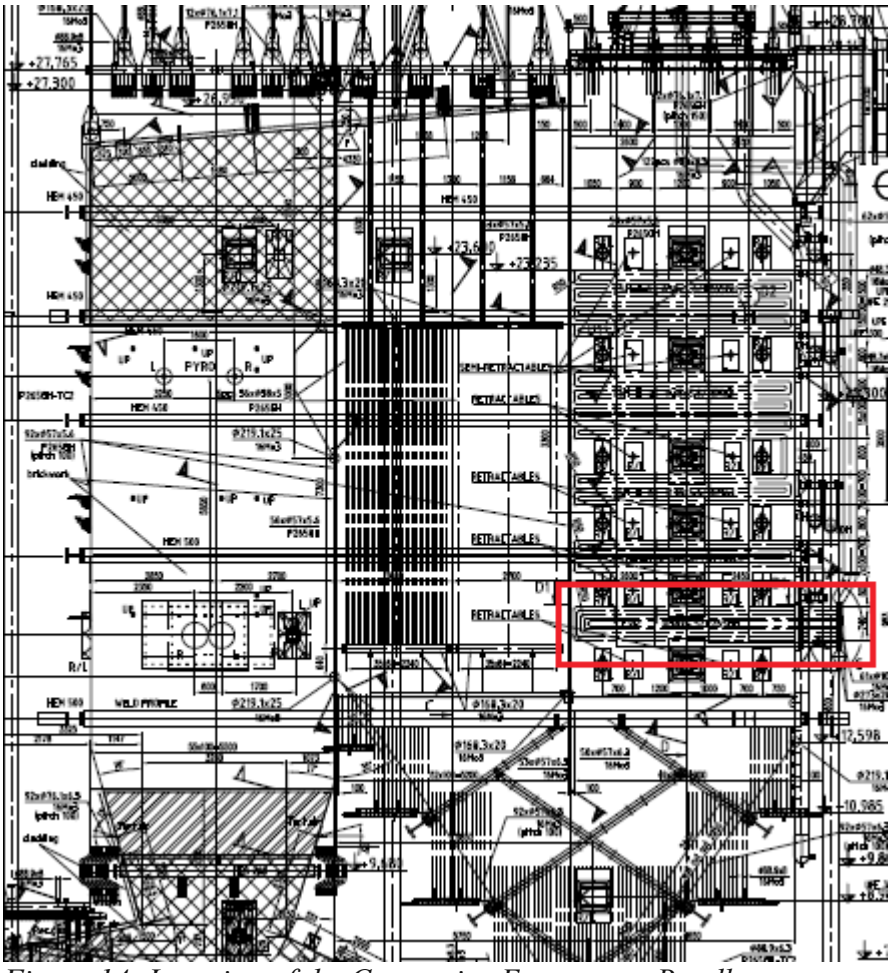

Figure 14: Location of the Convective Evaporator Bundle

The bundle consists of 5 tubes, going through the pass only twice (in and out). The first leak and tube deformations occurred on October 20th 2015 [9] at the locations illustrated in figure 15.

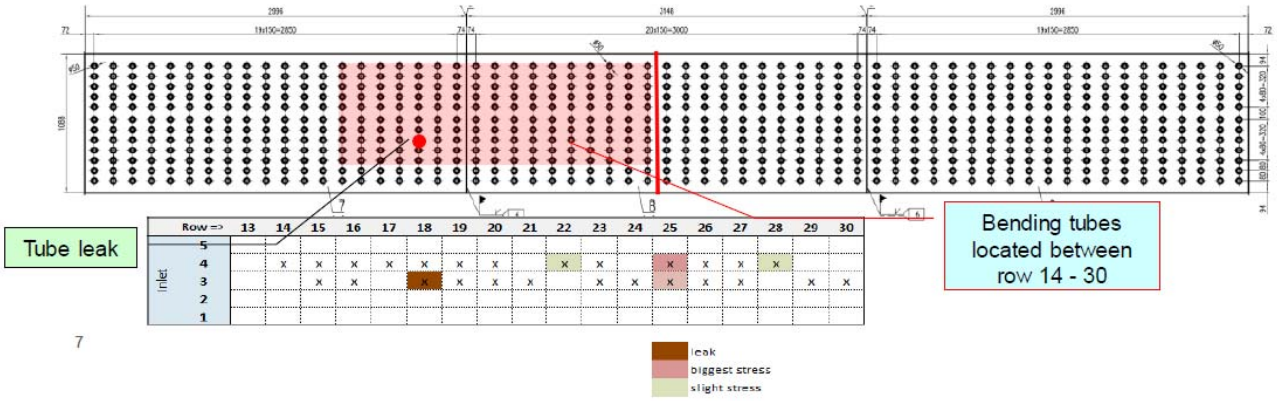

Figure 15: Locations of the Damages in the Convective Evaporator Bundle [9]

The two bottom rows of tubes are the hanger tubes of the third pass and are not part of the convective evaporator bundle itself. The bundles geometry and its modeling will be explained in detail in chapter 6.2.1 . One can see that the damages primarily occurred on the left side of the bundle. Both sides are separated and (largely) independent of each other, shown by the red line in the middle. Only the bottom parts of tubes 3 and 4 (i.e. the horizontal tube rows with numbers 3 and 4 in figure 15) experienced problems. Refer to figure 26 on page 40 for bundle nomenclature.

The bundle suffered new damages in December 2015 and March 2016, still at the bottom parts of tubes 3 and 4, but this time on the right side of the bundle [9]. Following that, the geometry of the bundle was modified: the tubes in the middle (4 and 5) were removed and the other tubes received a slight inclination (2.3 °). Figure 27 on page 41 shows a sketch of it. However, the new bundle geometry did not manage to solve the problems and new issues arose in July 2016, still on the right side of the bundle, but this time on the upper parts of tubes 2 and 3.

Investigation of the damages [9] revealed that they were all caused by overheating, likely due to bad circulation and therefore poor cooling of the tubes.

Figure 16 shows an illustration of the feeding and rising system of the bundle [10].

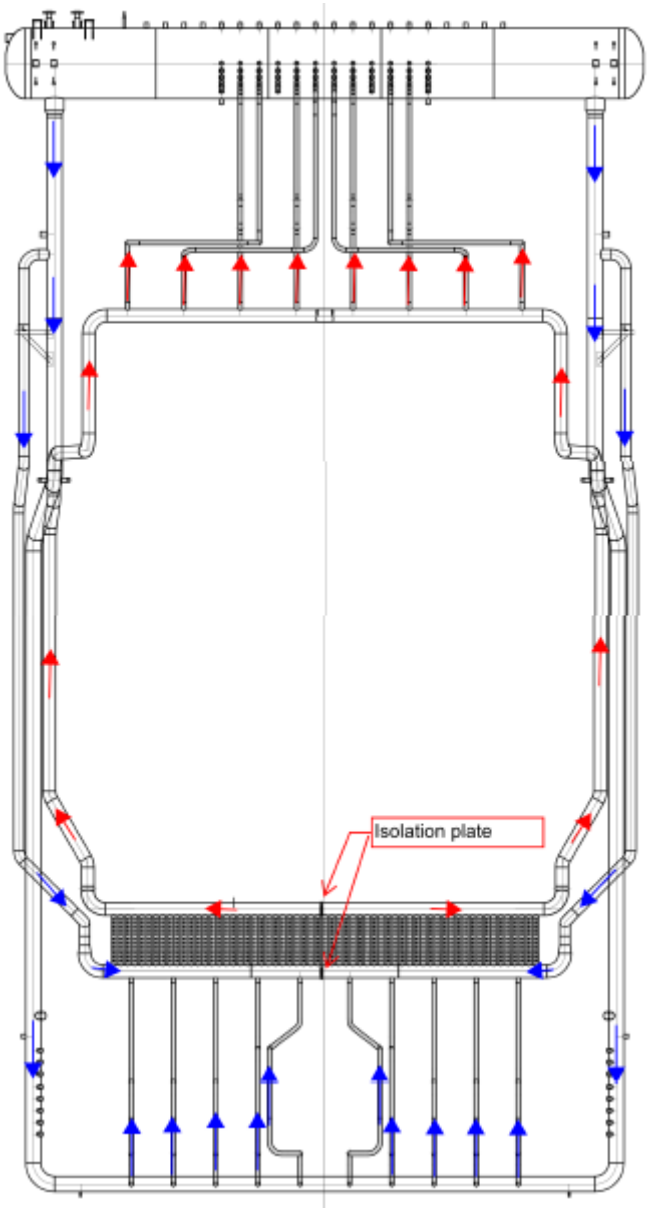

Figure 16: Feeding and Rising System of the Convective Evaporator Bundle [10]

Blue arrows denote saturated (slightly subcooled) liquid and red arrows a mixture of liquid and gas (partially evaporated). Two main down comers leave the drum and split into two separate feeding tubes each. One on each side leads directly to the bottom horizontal header located directly below the convective evaporator bundle. The other ones lead further downwards and connect at the horizontal header at the very bottom. The two lower horizontal headers are connected with each other via 10 feeding tubes.

After the fluid passes through the bundle and evaporates partially, it is gathered again in the horizontal header right above the bundle. From there, two risers on each side lead the mixture of liquid and gas to the very top horizontal header, where it flows through 8 smaller risers back to the steam drum.

The horizontal headers directly above and below the bundle are separated by blind plates ("isolation plates" in figure 16) which separate the left and right side of the bundle, as already mentioned before and illustrated in figure 15. The blind plates, however, are not "perfect", meaning that a small mass flow can still go through them. There is some concern [9] that this can contribute to instabilities, as this that makes it possible that mass flow can circulate between the two top horizontal headers through their connections with each other. The other horizontal headers at the very top and bottom are not separated at all. This will turn out to be of significance.

In addition to the convective evaporator bundle, the two main down comers also feed several other heat exchangers that are part of the natural circulation system. An overview of the whole system will be given in chapter 4 .

Measurements of tube and flue gas temperatures were performed in July 2016 with the new bundle geometry [9]. They showed the following two major effects:

- Tube temperatures can rise significantly above the saturation temperature, suggesting that the fluid in the tubes is either stratified or superheated, leaving the tubes insufficiently cooled. These temperature excursions can be of different magnitudes and show irregular oscillations. They always appear after a startup and can disappear after another shutdown and startup of the steam generator. All of this suggests local instabilities in the tubes.
- Flue gas temperatures are significantly lower than expected: they can go as low as 500 °C at the outlet of the convective evaporator bundle, while the expected temperature is 670 °C.

The description of the system and the occurring damages and instabilities so far can be used to derive the main subjects of investigation to find the cause for the instabilities:

- An uneven distribution of flue gas temperature across the width of the pass could be an explanation why heat damages only occur at specific sections of the bundle.
- As additional heat exchangers are attached to the down comers of the convective evaporator bundle, an increase in heat flux in one of those would also increase the mass flow into it, which could leave the convective evaporator with insufficient fluid to be properly cooled.
- Startups obviously play an important role in the emergence of instabilities, as the measurements show.
- As all startups (load transients in general) are accompanied by pressure variations, they should be investigated as well.
- Circulations between single tubes of the bundle could generally explain local instabilities.

- Foreign objects inside the bundle, partially blocking mass flow and possibly causing Ledinegg instabilities, could be another explanation for the heat damages and instabilities.
- The influence of different system configurations, such as, bundle geometry or flue gas temperatures.

To investigate all those possibilities, the natural circulation system was modeled and simulated using the simulation software Apros. The inner workings of that software are described in chapter 5.1 . The details on modeling the natural circulation system can be found in chapter 6 . The model was verified by comparing the results of the stationary status to the results of Flowtran (chapter 7). Flowtran is an in-house calculation software by CNIM designed to calculate the parameters (mass flow, steam quality, etc) of a natural circulation system in a stationary status (non transient). The configurations and results of the simulations (experiments) are then presented in chapter 8 and discussed in chapter 9 . That chapter also includes some suggestions relating to how to resolve the issues that were encountered.

4 General Design of the Natural Circulation System

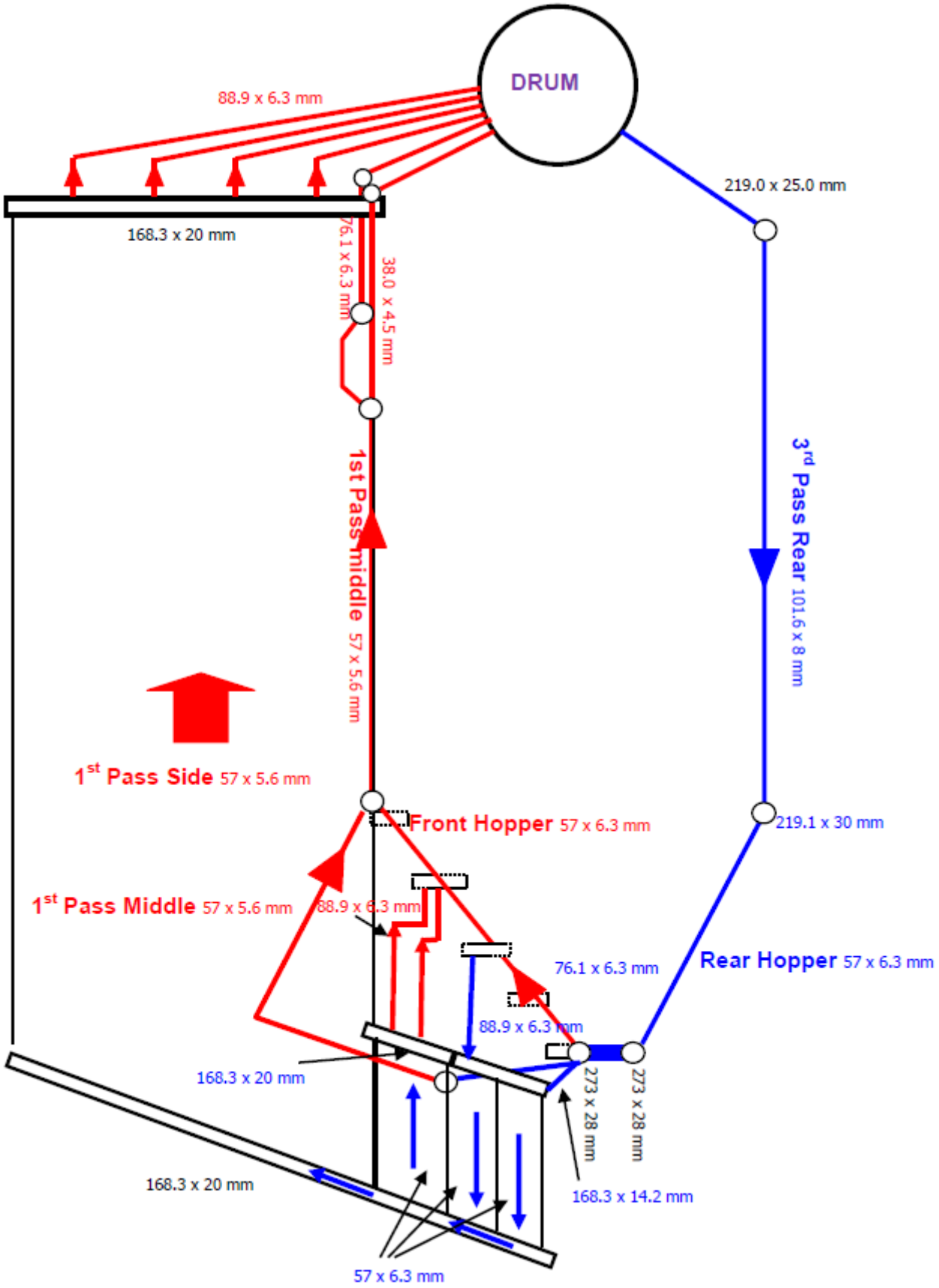

Figure 17: Flow Diagram of Flow Loop 1 [11]

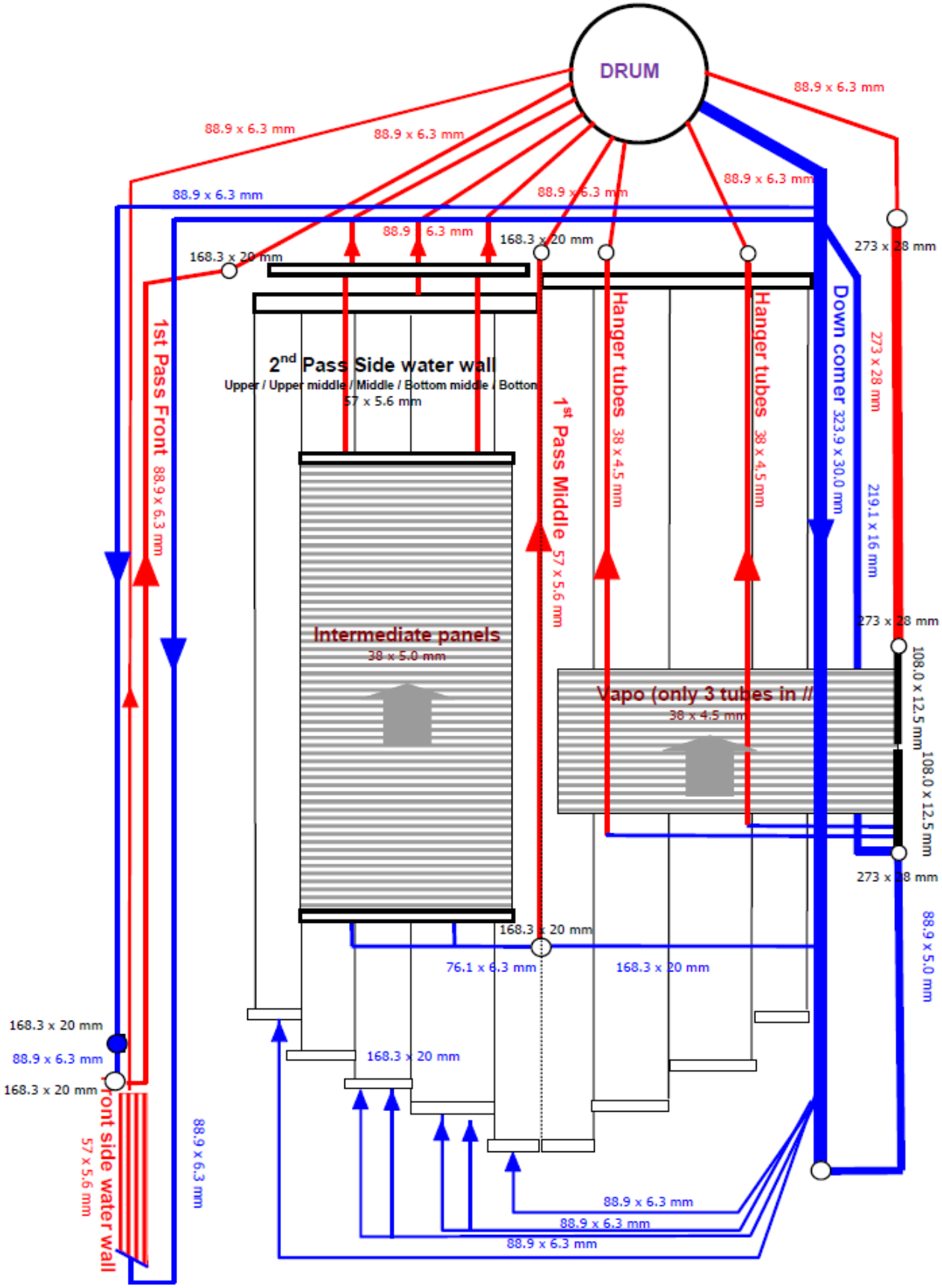

Figure 18: Flow Diagram of Flow Loops 2-5 [11]

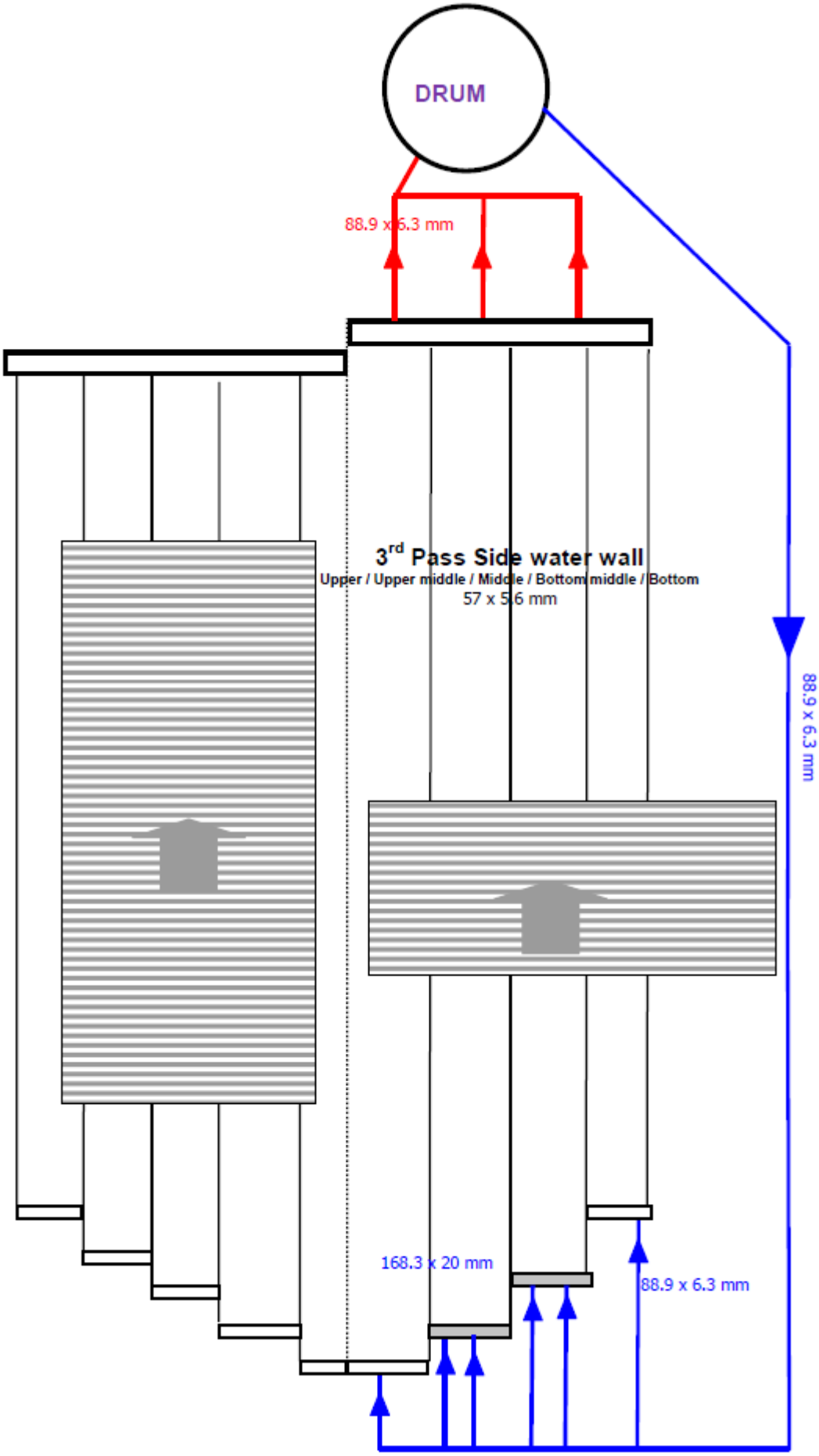

Figure 19: Flow Diagram of Flow Loop 6 [11]

The natural circulation system includes the first 3 passes of the steam generator and is divided into 6 flow loops. Their respective illustrations are shown in figures 17-19. Elements on the left side of the illustrations are seen as being in the front, and elements on the right are at the rear. Blue arrows in figures 17-19 denote pure liquid mass flows (usually not or only slightly heated), whereas red arrows show mass flows with a steam quality greater than 0.

Flow loop 1 is mainly fed by the rear water wall of the third pass, which makes it a heated down comer. Additional feeding is provided by a connection from one of the feed headers of the side water wall of the second pass, as the blue arrow in the bottom middle of figure 17 shows. The rising system of this flow loop comprises of the side water walls of the first pass, including the smaller parts in the rear, the separating water wall between first and second pass called "1st Pass Middle" in figure 17 including the grid, as well as the front hopper of the second pass. The top headers of the rear side water walls of the first pass are each divided into two parts with a diaphragm for steam venting in between them, as illustrated by the little black bar in figure 17. Flow loop 1 is described in detail in chapter 6.5.1 .

Flow loops 2, 3, 4 and 5, in figure 18, all share the same down comers. Flow loop 2 consists of the side and rear water walls of the second pass, as well as the intermediate panels. Please note that the rear water wall of the second pass is wrongly marked as "1st Pass Middle" in figure 18. Parts of the side water walls, "Upper Middle" in figure 18, are fed via connections from the top headers of the rear side water walls of the first pass, see figure 17. The intermediate panels consist of 12 modules each containing 36 vertical pipes, hanging in the second pass. They provide additional cooling of the flue gas in the second pass.

Flow loop 3 only contains the front water wall of the first pass including its roof. Flow loop 4 consists of the convective evaporator bundle in the third pass ("Vapo" in figure 18), as well as the hanger tubes of that pass. Flow loop 5 only includes a small part of the side water walls in the front of the first pass called "Front Side Water Wall" in figure 18.

Figure 19 shows the flow loop diagram of flow loop 6, which only consists of the side water walls of the third pass. It is important to note that this is the only part of the circulation system that is completely separated from the rest, apart from the steam drum of course. Flow loop 1 is interconnected with flow loops 2-5 via the connections between the side water walls of the second pass (flow loop 2) and the top headers of the rear side water walls of the first pass.

5 Basic Methodology and Calculations

5.1 Inner Workings of Apros

5.1.1 Six Equation Model

The *Advanced Process Simulator*, Apros, is the software used for modeling and simulating the natural circulation system in Ridham. It is capable of calculating dynamic two phase flows in pipe networks. This section describes the general calculation principles of Apros according to [12].

The calculation of transient processes with two phase flows in Apros is based on the so called six equation model. These six equations are the one dimensional conservation equations for mass, momentum and energy, each for liquid and gas separately. They can all be derived from the general transport equation. Figure 20 shows a sketch of a finite volume inside a pipe and all the variables that have to be considered.

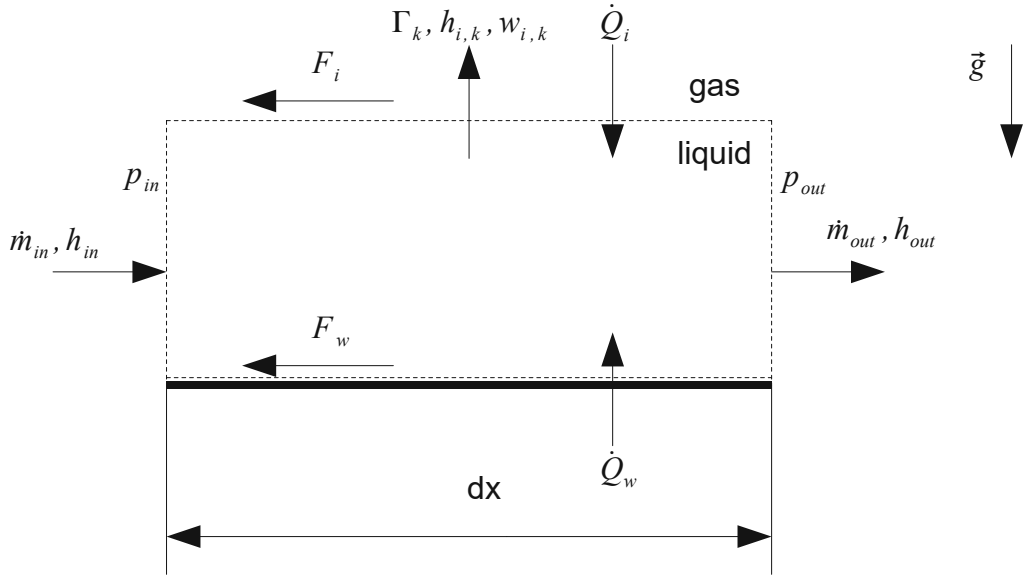

Figure 20: Sketch of a finite Volume with calculation variables

The general transport equation has the following form when neglecting diffusive terms:

$$\frac{\partial \rho X}{\partial t} + \frac{\partial \rho w X}{\partial x} = S_X$$

This is the differential form of the transport equation. X stands for an arbitrary variable that is transported through the control volume. The first term on the left side describes the accumulation of X in the control volume over time. The second term describes its convective transport in and out of the volume. S_X sums up all source terms that create or annihilate X inside the volume.

The *mass balance* has a very simple form:

$$\frac{\partial \alpha_k \rho_k}{\partial t} + \frac{\partial \alpha_k \rho_k w_k}{\partial x} = \Gamma_k$$

The index k stands for either liquid or gas. α_k is the volume fraction of the individual phase. The only source term Γ_k represents evaporation or condensation of water.

The *momentum balance* has the following form:

$$\frac{\partial \alpha_k \rho_k w_k}{\partial t} + \frac{\partial \alpha_k \rho_k w_k^2}{\partial x} + \alpha_k \frac{\partial p}{\partial x} = \Gamma_k w_{i,k} + \alpha_k \rho_k \vec{g} + F_{w,k} + F_{i,k}$$

The third term on the left side takes the pressure change over the volume into account and is a source term. The first term on the right side represents the momentum transfer from one phase to the other. The second term considers the hydrostatic pressure. $F_{w,k}$ is the friction between the phase and the wall and $F_{i,k}$ is the friction between the two phases at their interface. Other source terms on the right side can include friction caused by valves, friction due to form loss and pressure differences caused by pumps, but are not shown in the equation above for simplicity.

The *energy balance* has the form:

$$\frac{\partial \alpha_k \rho_k h_k}{\partial t} + \frac{\partial \alpha_k \rho_k w_k h_k}{\partial x} = \alpha_k \frac{\partial p}{\partial t} + \Gamma_k h_{i,k} + \dot{Q}_{i,k} + \dot{Q}_{w,k} + F_{i,k} w_{i,k}$$

h_k is the total enthalpy which includes the kinetic energy of the stream. The first term on the right side is the change of pressure due to technical work. The second term describes the enthalpy flow from one phase to the other. $\dot{Q}_{i,k}$ and $\dot{Q}_{w,k}$ are the heat fluxes at the interface between the phases and at the wall. The last term represents the heat generation caused by friction between the two phases at their interface.

To couple the equations, constitutive equations are used for the otherwise unknown friction and heat flux terms at the interface and the walls. They contain mainly empirical correlations. Only short descriptions of the constitutive equations will be presented in this work, please consider [12] for more detailed information.

Some of the constitutive equations are dependent on the current flow regime. Apros distinguishes between 4 different flow regimes: bubbly flow (at a low volume fraction of the gas phase), annular flow (high volume fraction, liquid covers the whole circumference of the pipe), droplet flow (high volume fraction, liquid as droplets in gas phase) and stratified flow (liquid and gas phase separated). To determine the current flow regime, the *rate of stratification* and *rate of entrainment* are used. The rate of stratification uses the Kelvin-Helmholtz criterion and additional experimental correlations to identify stratified flow. The rate of entrainment determines the fraction of liquid droplets in the gas phase. It is based on the Steen parameter and other experimental correlations.

Both the rate of stratification and entrainment, as well as the volume fraction of gas are used as weighting coefficients to ensure a smooth transition between the different flow regimes.

The wall friction is calculated using the following equation:

$$F_{w,k} = f_k \frac{\lambda_k \rho_k w_k^2}{2d}$$

d is the hydraulic diameter (inner diameter for a circular cross section) of the flow channel. The resistance coefficient λ is calculated using the correlations by Colebrook (also see section 6.1.4 and the Colebrook diagram in figure 25). The factor f_k is a two phase friction multiplier. It expands the pressure drop calculations from single phase flow and estimates the phase distribution on the pipe wall. Chapter 6.1.4 provides a more detailed description of the calculation of pipe roughness by Apros.

For the friction between the phases (interfacial friction), different correlations are used for different flow regimes and the interfacial friction is calculated as a weighted average of those correlations. The most important parameters are the velocity difference between the phases, the void fraction and the rates of entrainment and stratification. The last two are used to determine the flow regime, as described before.

Heat transfer between the pipe wall and the fluid is calculated depending on the heat transfer zone: dry wall (void fraction greater than 0.99999 or at boiling crisis), transition zone (critical heat flux for boiling crisis is exceeded but minimum film boiling temperature is not) and wet wall (otherwise). A combination of Zuber-Griffith and Biasi correlations are used to calculate the critical heat flux and the Groeneveld-Stewart correlation is used for the minimum film boiling temperature. Heat transfer on a wetted wall is split into two parts: The heat transfer coefficient for forced convection is calculated using the correlation by Dittus-Boelter:

$$\mathrm{Nu} = 0.023\,\mathrm{Re}^{0.8} + \mathrm{Pr}^{0.4}$$

Additionally, when the wall temperature is greater than the saturation temperature, the heat transfer coefficient during nucleate boiling is calculated with the Thom correlation:

$$\alpha_{nb} = 1971.2 \exp(2p/8687000)\left(T_w - T_{sat}\right)$$

The heat transfer between the phases is calculated separately for each phase:

$$\dot{Q}_{i,gas} = -\alpha_{i,gas}\left(h_{gas} - h''\right)$$

$$\dot{Q}_{i,liq} = \alpha_{i,liq}\left(h_{liq} - h'\right)$$

$\alpha_{i,k}$ are the heat transfer coefficients for the individual phases. The Lee-Ryley correlation is used to calculate $\alpha_{i,gas}$ both for superheated and subcooled steam and the Shah correlation with the

Vierow-Schrock correction is used to calculate $\alpha_{i,liq}$ for the liquid phase.

The interfacial heat fluxes are also used to calculate the mass flow between the phases by forming the energy balance for the interface:

$$\Gamma_{gas} = -\Gamma_{liq} = \frac{-\dot{Q}_{i,liq} - \dot{Q}_{i,gas}}{h'' - h'}$$

5.1.2 Discretization Scheme

Space discretization in Apros is using a so called staggered grid consisting of nodes and branches. Nodes are finite volumes that are subdivisions of larger volumes, for example parts of a pipe. Usually, space is only discretized in one direction (e.g. the axis of the pipe) using these nodes. Branches are connections between the nodes. State variables, such as, enthalpy or pressure are calculated in the nodes and flow variables, as flow velocity, are calculated in the branches. Figure 21 shows the basic one dimensional discretization of a pipe.

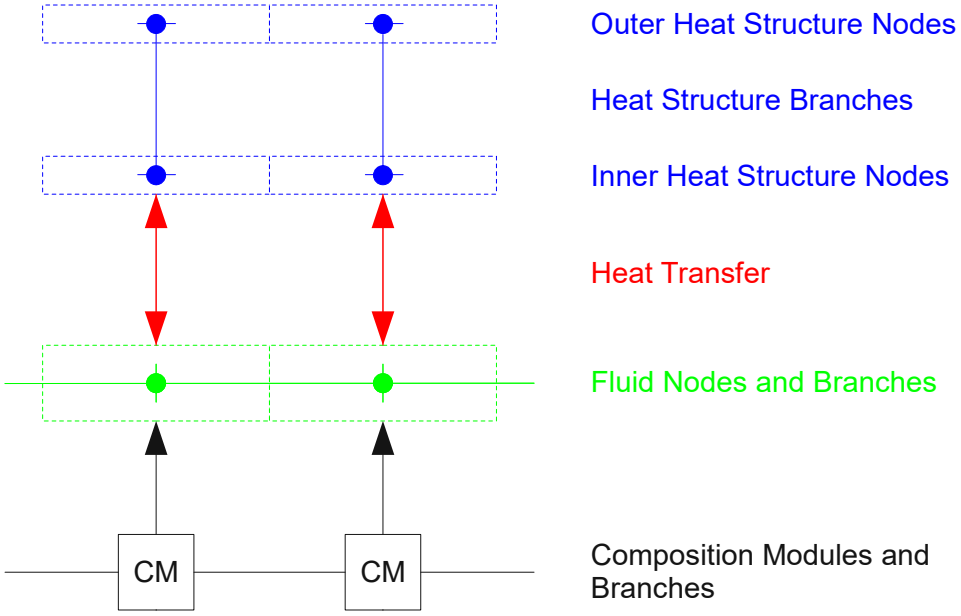

Figure 21: Discretization of a Pipe in Apros

The inner volume of the pipe is split into nodes that are connected axially by branches. The composition modules store fluid characteristics and are directly connected to their respective fluid nodes. They are also connected with each other axially via composition branches. The composition modules and branches form a parallel grid to the one built by the fluid nodes and their branches. By changing the composition modules the simulated fluid can be easily altered.

The heat structure nodes represent the pipe wall. They are actually not volumes but areas: the inner heat structure nodes represent the inner surface of the pipe wall and the outer ones the outer surface. They are connected with each other radially with heat structure branches in which heat conduction between the inner and outer side is calculated. Axial heat structure branches for the calculation of axial heat conduction are also possible but because its influence is expected to be negligible they were not implemented in the model.

It is important to note that the heat structure nodes are also axial subdivisions of the pipe wall. One heat structure node represents the pipe wall over the whole circumference of the pipe (either inside

or outside), meaning that the temperature is assumed to be equal for the whole represented area. In reality, this is not the case for stratified flow in a horizontal pipe: Then the top half is only in contact with the steam phase and is not cooled as well as the bottom half in contact with the liquid phase.

Fluid nodes and heat structure nodes are interconnected with heat transfer modules, calculating the heat flux from the fluid to the inner pipe wall (or the other way around) as described in the previous chapter. It is also possible to connect fluid nodes to the outer pipe wall with heat transfer modules to calculate heat fluxes on the shell side of the pipe.

As natural circulation systems are essentially pipe networks, almost the entire system was modeled using pipes such as the one described above. One exception is the steam drum shown in figure 22. A more general description of the steam drum model used in the simulations including the drum level control can be found in chapter 6.6 .

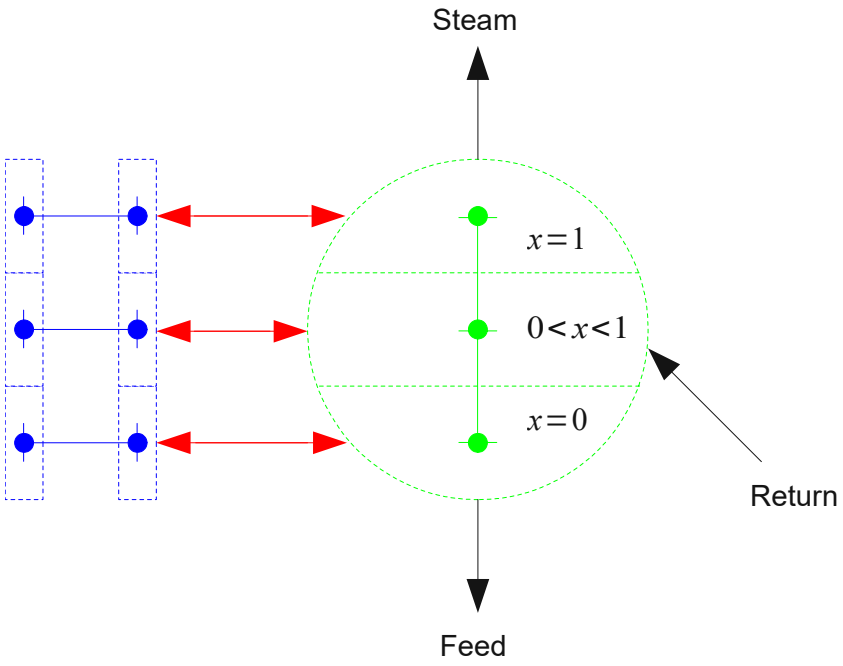

Figure 22: Discretization of the Steam Drum in Apros

The steam drum is not divided axially but vertically into 3 fluid nodes connected with branches. The composition modules and branches are not shown in this figure but of course exist parallel to the network of fluid nodes. Each fluid node is connected to its own heat structure nodes via a heat transfer module.

The vertical division makes it possible to separate the water and steam phases within the steam drum: the bottom node only contains liquid and the top node only gas. Contrary to reality, the middle node does not contain separated liquid and gas phases but a homogenous mixture. The

branches ensure that only liquid is transferred between the bottom and the middle node and only gas is transferred between the top and the middle node. So the actual separation between liquid and gas is accomplished in the branches connected to the middle node, which is why the return mass flow (which is a mixture of water and steam) is connected to the middle node. All feeding pipes (pure liquid) are connected to the bottom node and steam leaves the drum from the top node. Of course, all those connections also include branches to the fluid nodes in the steam drum.

The liquid level in the drum is calculated automatically as a function of the void fraction in the middle node. The liquid level is important for the calculation of hydrostatic pressure differences in the connected pipes.

Besides the steam drum, the only other component that was not modeled as a pipe with heat structures is the gas side flow channel for the convective evaporator bundle. There the flow channel was divided into 4 parallel parts, which were also modeled as pipes, but with a rectangular cross section and no heat structures connected to the fluid nodes. Chapter 6.2.2 describes modeling of the gas side in more detail.

5.2 Combustion Calculation

Combustion calculations had to be done to obtain the composition of flue gas, which the simulation software requires in order to calculate the state variables of flue gas as a function of pressure and specific enthalpy, such as temperature or heat capacity.

First, the fuel composition is needed, which was obtained from [8]:

Component	Mass Fraction
Carbon	$\gamma_C = 0.41$
Oxygen	$\gamma_O = 0.232$
Hydrogen	$\gamma_H = 0.04$
Nitrogen	$\gamma_N = 0.006$
Sulfur	$\gamma_S = 0.001$
Water	$\gamma_{H2O} = 0.25$
Ash	$\gamma_{Ash} = 0.061$

Table 1: Fuel Composition [8]

Using the geodetic height of the steam generator [7],

$$h_{geo} = 4\,\mathrm{m}$$

the atmospheric pressure at site can be calculated using the barometric formula:

$$p_{at} = 1.013\,\mathrm{bar}\left(1 - \frac{6.5\,h_{geo}}{288000\,\mathrm{m}}\right)^{5.225} = 1.013\,\mathrm{bar}$$

Assuming the ambient air temperature [8]

$$T_{amb} = 15\,^{\circ}\mathrm{C}\,,$$

vapor pressure can be calculated using the Antoine equation:

$$p_{vap} = \exp\left(19.016 - \frac{4064.95}{T_{amb}/^{\circ}\mathrm{C} + 236.25}\right) = 17.066\,\mathrm{mbar}$$

Atmospheric pressure, vapor pressure and relative humidity [8]

$$\varphi = 0.7$$

were then used to calculate the mass fraction of water in dry air:

$$X_{H2O} = \frac{m_{H2O}}{m_{A,d}} = 0.6216\,\frac{\varphi\, p_{vap}}{p_{at} - p_{vap}} = 7.4597 \cdot 10^{-3}$$

Table 2 lists some molar masses and mass fractions of air components [13] that will be used in the following calculations.

Substance	Molar Mass
Carbon	$M_C = 12.011 \frac{\text{g}}{\text{mol}}$
Hydrogen	$M_H = 1.008 \frac{\text{g}}{\text{mol}}$
Oxygen	$M_O = 15.999 \frac{\text{g}}{\text{mol}}$
Sulfur	$M_S = 32.06 \frac{\text{g}}{\text{mol}}$

Substance	Mass Fraction in dry Air
Nitrogen	$\xi_{A,N2} = 0.755425$
Oxygen	$\xi_{A,O2} = 0.231414$
Carbon Dioxide	$\xi_{A,CO2} = 0.000505$
Noble Gases (Argon)	$\xi_{A,Ar} = 0.012653$

Table 2: Molar Masses and Mass Fractions of Air Components [13]

Now the specific flue gas mass flow can be calculated, which is the mass flow of flue gas divided by the mass flow of fuel. First, the specific mass flow of oxygen:

$$\mu_{O2} = \left(\frac{\gamma_C}{M_C} + \frac{\gamma_H}{4 M_H} + \frac{\gamma_S}{M_S} - \frac{\gamma_O}{2 M_O} \right) 2 M_O = 1.179 \frac{\text{kg O}_2}{\text{kg Fuel}}$$

The formula derives from the stoichiometric equations for burning each (combustible) fuel component. From that, the specific mass flow of dry air (without air excess) follows:

$$\mu_{A,0,d} = \frac{\mu_{O2}}{\xi_{A,O2}} = 5.095 \frac{\text{kg Air (stoich,dry)}}{\text{kg Fuel}}$$

The requirement of ambient air is then calculated considering its mass fraction of water:

$$\mu_{A,0} = \mu_{A,0,d} \left(1 + X_{H2O} \right) = 5.133 \frac{\text{kg Air (stoich)}}{\text{kg Fuel}}$$

The total requirement of air considering an air excess [8] of

$$n = 1.4$$

then follows to:

$$\mu_A = n \mu_{A,0} = 7.186 \frac{\text{kg Air}}{\text{kg Fuel}}$$

The air excess takes into account that a higher mass flow of air than the stoichiometric one is needed to achieve sufficient combustion of fuel. It usually comes from experience. The specific mass flow of flue gas is then easily calculated considering the non-combustible fraction (ash) of the fuel:

$$\mu_G = \mu_A + 1 - \gamma_{Ash} = 8.125 \frac{\text{kg Flue Gas}}{\text{kg Fuel}}$$

Now the mass fraction of each component of flue gas can be calculated:

$$\xi_{G,CO2} = \frac{1}{\mu_G}\left(\frac{M_C + 2M_O}{M_C}\gamma_C + \xi_{A,CO2}\mu_{A,0,d}\,n\right) = 0.185348$$

$$\xi_{G,H2O} = \frac{1}{\mu_G}\left(\frac{2M_H + M_O}{2M_H}\gamma_H + \gamma_{H2O} + X_{H2O}\mu_{A,0,d}\,n\right) = 0.081315$$

$$\xi_{G,O2} = \frac{1}{\mu_G}\left(\xi_{A,O2}\mu_{A,0,d}\,(n-1)\right) = 0.058047$$

$$\xi_{G,SO2} = \frac{1}{\mu_G}\frac{M_S + 2M_O}{M_S}\gamma_S = 0.000246$$

$$\xi_{G,N2} = \frac{1}{\mu_G}\left(\gamma_N + \xi_{A,N2}\mu_{A,0,d}\,n\right) = 0.663936$$

$$\xi_{G,Ar} = \frac{1}{\mu_G}\left(\xi_{A,Ar}\mu_{A,0,d}\,n\right) = 0.011108$$

The equations derive from stoichiometric equations and considering air components.

6 Modeling of the Circulation System

6.1 General

6.1.1 Levels of Precision

For the model, the circulation system was divided into three parts, each modeled at different levels of discretization and precision.

- ***Level 1*** includes flow loops 1 and 6. Since they are expected to have little influence on the convective evaporator bundle, they were modeled in the simplest way. Parallel tubes are combined into single components, meaning that uniform flow between parallel tubes is assumed. There is no distinction between left and right side components, meaning that mass flows are equal in both sides of side water walls. Only the side water walls of the first pass were modeled separately because of their interconnection with the side water walls of the second pass, which are also modeled separately (see level 2). Heat fluxes can be set variably as functions over time, for example as a ramp or sine function.

  There are two reasons flow loops 1 and 6 were even modeled at all: First, flow loop 1 is interconnected to flow loops 2-5, as explained in section 4 , this required flow loop 1 to be modeled as well. Second, when considering pressure variations in the steam drum, the heat capacity of the water and steel in flow loops 1 and 6 constitutes an inertia regarding temperature changes in the whole system that can-not be neglected.

- ***Level 2*** includes all components connected to the same down comer as the convective evaporator bundle, which are flow loops 2, 3 and 5. Compared to level 1, left and right side components were modeled separately.

- Finally, ***level 3*** contains the convective evaporator bundle, the hanger tubes of the third pass and all their feeding and rising systems. Since those components are the main subject of the investigation, they were modeled with the highest accuracy. Every tube was modeled separately on its own, and node lengths can be as small as 0.5 m. The details of modeling this level are described in sections 6.2 - 6.4 .

6.1.2 Numbering Scheme

In general, numbering each part of the steam generator was done in the same way as in the Flowtran calculations conducted by CNIM. However, some of the sections that Flowtran considers as single sections were modeled as multiple independent sections to improve model accuracy. For example, the left and right side water walls of the first pass appear as a single section in Flowtran with the section number 101. In the model, each side was modeled separately. To preserve the original section numbers, each side was given a subsection number based on the original section number, so the left and right side water walls have the section numbers 101.1 and 101.2 in the model.

Sections in the model were numbered from left to right first, followed by outside to inside. This was done to utilize the symmetry of the steam generator to make modeling it with the simulation software easier. For example, take a look at figure 23. It shows a smaller detail of figure 34 on page 53.

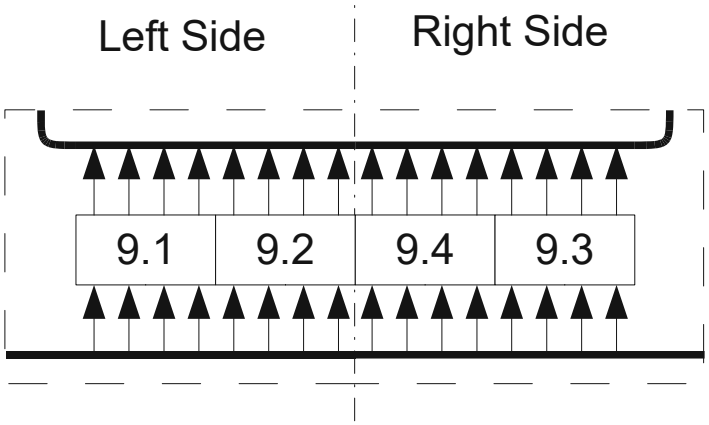

Figure 23: Detail of Figure 34 showing the Numbering Scheme

The 4 parts marked with the section numbers 9.1-9.4 are subdivisions of the convective evaporator bundle. Notice that the lower section numbers are the ones on the *left* side (*left before right*) and within the left side, the outside section is the first one (*outside before inside*). After numbering all the sections on the left side, numbering continues on the *outer* right side.

Some sections are modeled with more detail than others, see chapter 6.1.1 . Therefore, their section numbers can include more subsections. For example, section 9.3.12.1 is the 1st tube in the 12th row of the 3rd subdivision of section 9, being the convective evaporator bundle. Usually, only the first level of section numbers will be used in this work. If other levels are used, they will be explained separately.

6.1.3 Model Parameters

Some characteristics of the steam generator are uncertain and, as the following chapters will show, some parts can have different configurations. Every uncertainty or possible configuration is equal to a parameter in the model. Changing a parameter changes the general behavior of the model. Those parameters are:

- *Bundle configuration*: The configuration of the convective evaporator bundle was changed after the circulation issues and overheating occurred, as mentioned in chapter 3 . Investigations were conducted for both the old and the new bundle geometry. Chapter 6.2.1 describes both versions in detail.
- *Flue gas temperature*: As [9] shows, temperatures at the outlet of the convective evaporator bundle (new configuration) can be as low as 500 °C, which is much lower than the expected outlet temperature of 670 °C. Lower flue gas temperatures lead to lower mass flows in the convective evaporator bundle, which promotes instability. Therefore, investigations were conducted with flue gas temperatures at the inlet of the bundle of 710 °C (design value [8]), 630 °C and 550 °C.
- *Blind Plates*: Those are plates separating parts of the feeding and rising system of the convective evaporator bundle, as mentioned in chapter 3 and explained in detail in section 6.4 . They were considered to be perfect separators for major parts of the design process, meaning that the mass flow between the separated parts was assumed to be 0. In reality, a small mass flow through the blind plates is possible, and there have been some concerns [9] that this might contribute to the emergence of instabilities. This is why investigations were conducted with both perfect (no mass flow) and imperfect (mass flow possible with a form loss coefficient of 350) blind plates.
- *Separated Feeding and Rising Systems*: When hot startups were investigated, major oscillations in mass flow occurred between the left and right side of the convective evaporator bundle, see chapter 8.2.4 . To suppress those, the left and right sides were completely separated by separating their common feeding and rising header (section 6.4 explains the main feeding and rising system). To investigate the influence of such a separation in different situations, experiments were conducted for both separated and non-separated feeding and rising systems of the convective evaporator bundle.

Table 3 shows all possible combinations of model parameters, called permutation matrix:

perm#	Bundle Con.	T_G	Blind Plates	Sep. System
1	1	710	0	0
2	1	710	0	1
3	1	710	1	0
4	1	710	1	1
5	1	630	0	0
6	1	630	0	1
7	1	630	1	0
8	1	630	1	1
9	1	550	0	0
10	1	550	0	1
11	1	550	1	0
12	1	550	1	1
13	2	710	0	0
14	2	710	0	1
15	2	710	1	0
16	2	710	1	1
17	2	630	0	0
18	2	630	0	1
19	2	630	1	0
20	2	630	1	1
21	2	550	0	0
22	2	550	0	1
23	2	550	1	0
24	2	550	1	1

Table 3: Permutation Matrix

perm#	Permutation number
Bundle Con.	1=old, 2=new convective evaporator bundle configuration
T_G	Flue gas temperature at the inlet of the convective evaporator bundle
Blind Plates	0=perfect blind plates (no mass flow), 1=imperfect blind plates
Sep. System	0=separated feeding / rising system (no mass flow), 1=not separated

6.1.4 Pipe Roughness and Form Loss Coefficients

Pipe roughness and form loss coefficients are used by the simulation software to determine pressure losses due to friction and other dissipating processes in a pipe network. For a specific section, the pressure loss Δp_F is calculated using the following equation:

$$\Delta p_F = \left(\lambda \frac{l}{d} + \zeta \right) \rho \frac{w^2}{2}$$

The first term, $\lambda \frac{l}{d}$, describes the pressure loss due to skin friction, that is the friction between the liquid or gas and the pipe wall, in a straight tube. It is composed of the so called resistance coefficient λ, the length of the tube l and its inner (hydraulic) diameter d. The resistance coefficient is a function of the Reynolds number and the pipes relative roughness:

$$\lambda = \mathrm{f}\left(\mathrm{Re}, \frac{\delta}{d} \right)$$

δ is the so called equivalent roughness. It is an empirical factor used to scale friction losses for different pipe materials or under different operating conditions. According to [14], it was set to

$$\delta = 0.1\,\mathrm{mm}$$

for “water pipes of heating systems with deaeration and chemical treatment of running water”. The simulation software automatically calculates the resistance coefficient based on the Reynolds number and relative roughness using the Colebrook equations (also see figure 25) for single phase flow.

An additional multiplier is used to expand the single phase friction to two phase flow, as already mentioned in chapter 5.1.1 . In the case of stratified flow, the multiplier considers the flow area of the pipe each phase occupies. Additional correlations exist for non-stratified flow with and without entrainment of liquid droplets based on the volume fraction of gas and the ratios of density, dynamic viscosity and mass flow between the phases. Please consider [12] for more detailed information.

The second term in the equation above, ζ, is the form loss coefficient. It describes the pressure loss due to bends, orifices, sudden expansions of tube diameter, etc. They were set in different ways depending on the level of precision (chapter 6.1.1): On levels 1 and 2, sections were mostly modeled as straight vertical parts (see chapter 6.5). There, form loss coefficients were used to calibrate the mass flows in all sections so they would match the Flowtran results in stationary states (chapter 7).

On level 3, form loss coefficients were set with more attention to detail:

- Form loss coefficients at headers were set to 1 for converging headers and 0.5 for diverging headers. These values are based on experience. The very complex geometry of the headers and possible flow paths prohibited more accurate estimations.
- The bends of the tubes inside the convective evaporator bundle and of the hanger tubes were set using figure 24 [2]:

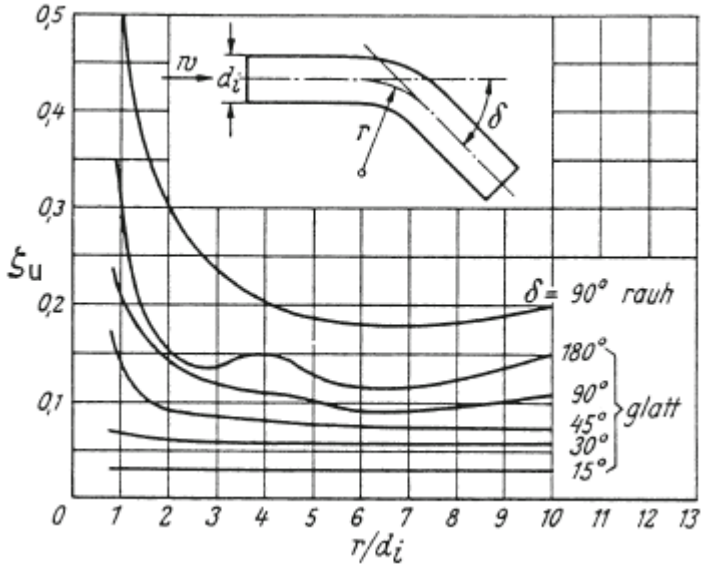

Figure 24: Form Loss Coefficients of Bends [2]

Figure 24 shows form loss coefficients ζ_u for rough ("rauh") and smooth ("glatt") bends with different bend angles δ for high Reynolds numbers $\mathrm{Re}>10^5$. In a stationary state all bends fulfill this requirement regarding the Reynolds number. Bends can show much higher form loss coefficients for lower Reynolds numbers [2], which was not considered (form loss coefficients are constant).
All bends were considered to be rough. For bend angles other than 90° the form loss coefficients were approximated as being 2 times the form loss coefficient of a smooth bend with the same bend angle.

- For the main feeding and rising system (chapter 6.4), where the feeding pipes right below the convective evaporator bundle and the riser tubes above the bundle were also modeled as straight vertical tubes, the form loss coefficients of all bends in a pipe were added up. The additional length l_{add} of the pipe compared to its length in the model was also taken into account, leading to the following equation for the total form loss coefficient:

$$\zeta = \lambda \frac{l_{add}}{d} + \sum \zeta_{BEND}$$

Figure 25 [2] was used to estimate the resistance coefficient λ :

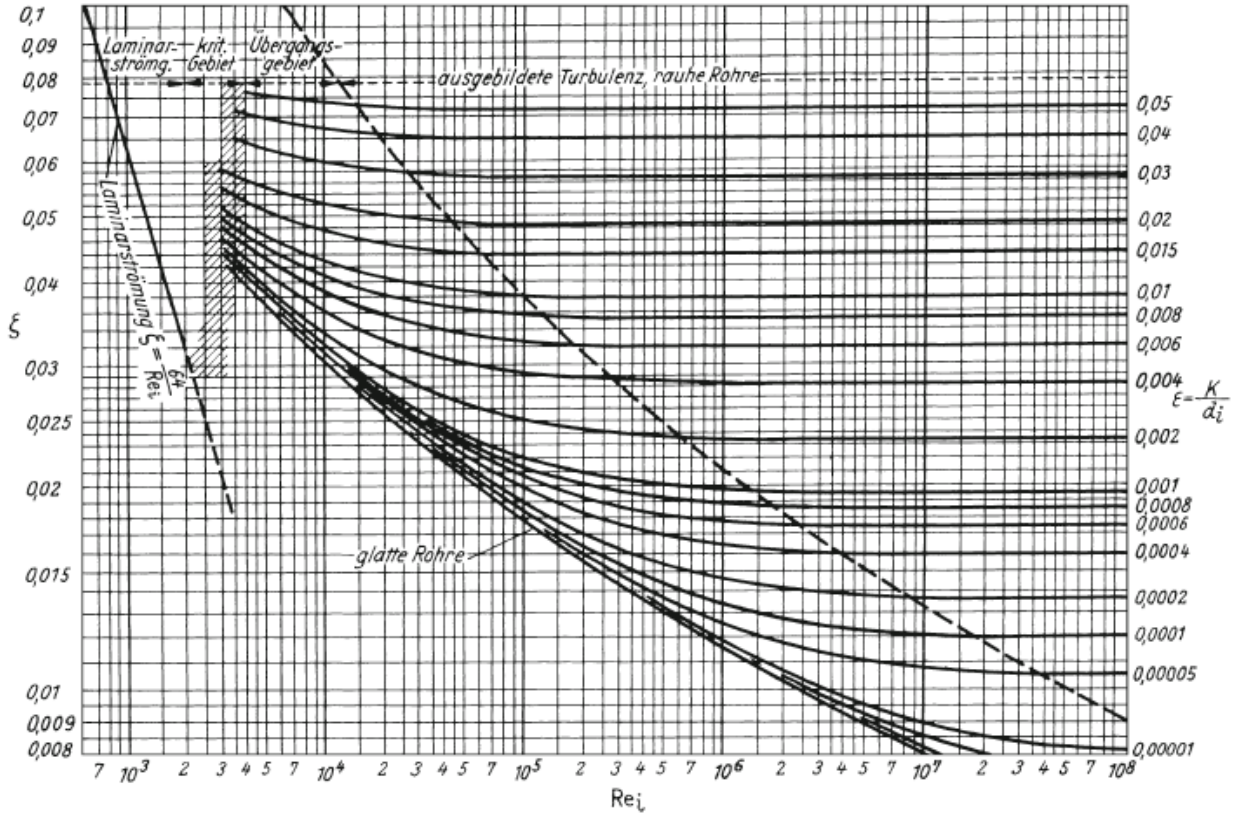

Figure 25: Resistance Coefficients [2]

Figure 25 is also known as a *Colebrook diagram*. The ξ -values on its left side are the resistance coefficients as a function of Reynolds number Re_i (in respect to the inner diameter of the pipe) and relative roughness ε . The resistance coefficients for the equation above were taken for Reynolds numbers in a stationary state.

- Form loss coefficients for cyclones inside the steam drum were set to 1.

6.2 Convective Evaporator Bundle

6.2.1 Water Side: Old and New Configuration

There are two different configurations of the convective evaporator bundle, an “old” one and a “new“ one. The new one was introduced by CNIM as a first try for solving the instability problems, which unfortunately did not help. Figure 26 shows a sketch of a single row of the old configuration and how it was modeled.

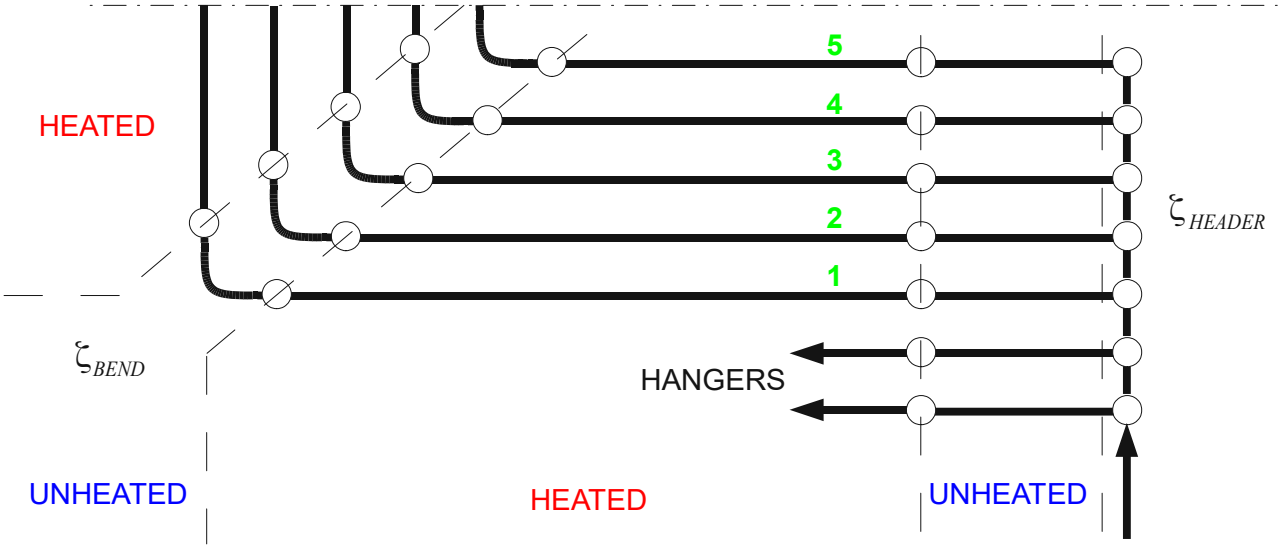

Figure 26: Sketch of a single row of the old configuration of the convective evaporator bundle

Bold lines represent pipes and circles depict connection points (nodes) between pipes with different characteristics such as flow direction, loss coefficient or whether it is a heated or an unheated part. The figure only shows the bottom half of one row of the bundle. Besides the hanger tubes, which do not exist on the top half, the top half is symmetrical to the bottom half of the row. The whole bundle consists of 61 rows such as this one.

A specific characteristic of the bundle are its vertical headers on the far right of figure 26. They are connected to the feeding system on the bottom right, which will be explained in section 6.4 . The first (bottom) two pipes leaving the vertical header are the hanger tubes of the third pass. Section 6.3 explains how they were modeled. The following pipes, numbered 1 to 5, make up the actual convective evaporator. The pressure loss that occurs at the intersection between a pipe and the vertical header is considered using the form loss coefficient ζ_{HEADER} .

All pipes leaving the vertical header first have an unheated section of equal length before entering the third pass through the water wall. Inside the pass, the horizontal and vertical parts of the pipes are heated. The bends, which are only a very small part of each pipe, are not heated in the model, since modeling this would have required an unreasonable effort. Pressure loss in the bends is

considered using the form loss coefficient ζ_{BEND} .

A sketch of the new configuration of the convective evaporator bundle is shown in figure 27.

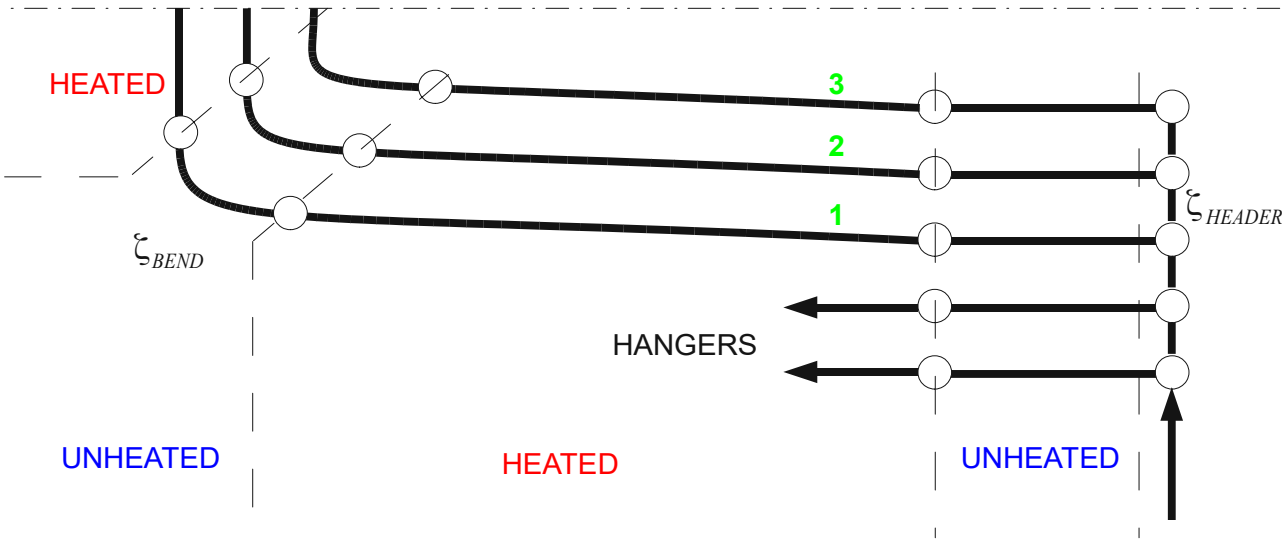

Figure 27: Sketch of a single row of the new configuration of the convective evaporator bundle

Compared to the old configuration, the new one only has 3 pipes (numbered 1 to 3) in each row and they are slightly inclined with an angle of 2.3° to the horizontal. A smaller number of tubes decreases the total heat flux into the bundle by decreasing the heat transfer area, but it increases heat flux density (heat flux per pipe / per heat transfer area) because the now higher flue gas temperatures inside the bundle result in higher temperature differences to the outer wall temperatures of the pipes. In a natural circulation system, higher heat flux densities lead to higher mass flow densities (mass flow per pipe), as long as the heat flux does not exceed the critical heat flux.

The inclination of the pipes helps steam bubbles to flow in the right direction (upwards). Both the inclination and the higher mass flow density improve stability in the bundle by making it harder for the mass flow to ever change direction. Every change of direction is accompanied by a period of time where the mass flow is very small or zero. During this time, the pipe is poorly cooled which can result in heat damages.

Other than the number of pipes and their inclination, everything stays the same as in the old configuration.

6.2.2 Gas Side

Figure 28 shows the gas side model for the old bundle configuration (5 pipes per row). Modeling of the gas side for the new bundle configuration was done using the same method.

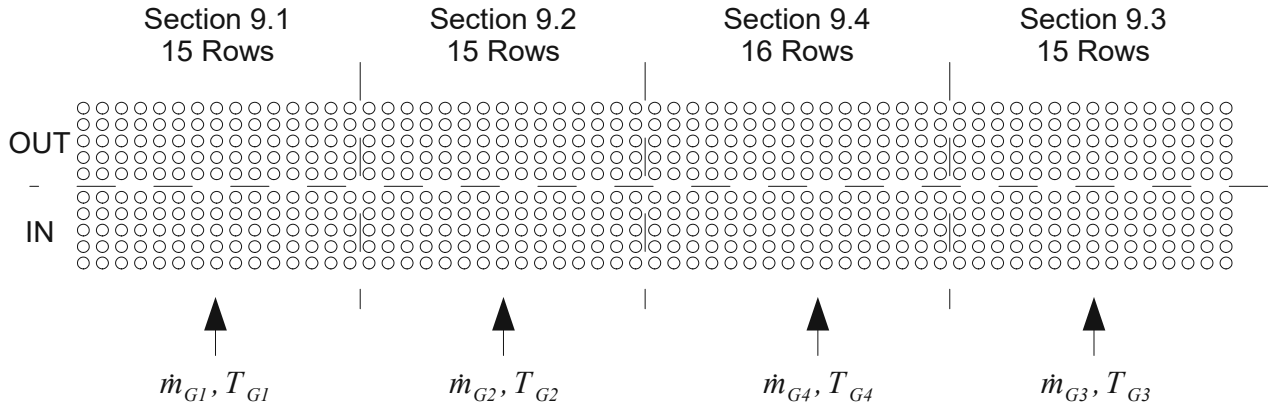

Figure 28: Sketch of the gas side model of the convective evaporator bundle

The bundle was split horizontally into 4 parts. As explained in section 6.1.2 , the subsections of the bundle (section number 9 in the Flowtran calculations by CNIM) were numbered from left to right first, followed by outside to inside, resulting in the numbers shown above. Since the total number of rows in the bundle is 61, one subsection (9.4) contains 16 rows, whereas, all the other ones only contain 15 rows.

This horizontal division of the bundle made it possible to investigate the influence of different flue gas temperatures at the inlet of parts of the convective evaporator bundle. The flue gas mass flow can be different at different subsections as well, but it is usually considered to be uniformly distributed over the whole width of the bundle.

The bundle was also split vertically into a lower and upper half. Every vertical / horizontal subdivision of the bundle is equal to a calculation node on the gas side, so the gas side of the bundle consists of 8 nodes total, equal to the divisions defined by dashed lines in figure 28.

6.2.3 Heat Transfer between Water and Gas Side

6.2.3.1 Overview

To calculate the heat transfer from a gas node to each node of every pipe within that gas node, the following general formula was used:

$$\dot{Q}_{G,n} = A_n \alpha_r \left(T_{G,n} - T_{w,n} \right) f_p$$

The meaning and calculation of each variable will be explained using the sketch in figure 29.

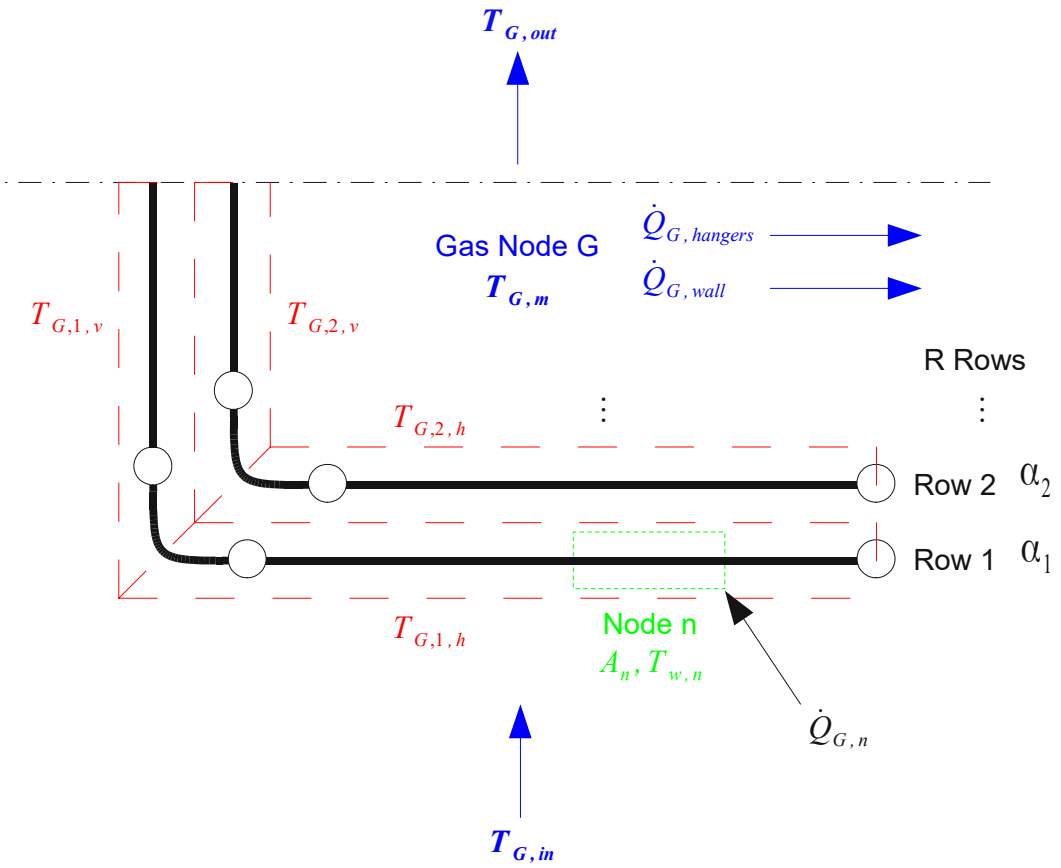

Figure 29: Sketch of calculation variables for calculating heat flux from flue gas to bundle

Please note that, in the following context, a “row” is a horizontal arrangement of tubes, as opposed to a vertical arrangement such as in figure 28. Although confusing, it is common in this field, and therefore will be used in this work as well.

$\dot{Q}_{G,n}$ is the heat flux from the gas node “G” into a node “n”. Nodes are subdivisions of pipes with a length of about 0.5 m each. Each node has its own outer wall temperature $T_{w,n}$ and heat transfer area A_n, which is the outer surface area of the pipe. Both the outer wall temperature and the heat transfer area are calculated automatically by the simulation software.

$T_{G,n}$ is the gas temperature at node n. Depending on the location of the node, the gas temperature is linearly interpolated between the inlet and outlet gas temperatures of the gas node. For a horizontal node in row “r” with a total number of “R” rows in the gas node, the formula goes:

$$T_{G,n} = T_{G,r,h} = \left(\frac{R-r}{R} + \frac{1}{2R} \right) \left(T_{G,in} - T_{G,out} \right)$$

For a vertical node, the formula is:

$$T_{G,n} = T_{G,r,v} = \left(\frac{R-r}{2R} + \frac{1}{2R} \right) \left(T_{G,in} - T_{G,out} \right)$$

Both formulas are used for the old as well as the new bundle configuration by changing the parameter R. This interpolation made it possible to take the gas temperature gradient within the gas node into account, resulting in different heat fluxes at different rows.

To get the correct outlet temperature of a gas node, the heat fluxes from that gas node to the hanger tubes and water walls, $\dot{Q}_{hangers}$ and $\dot{Q}_{wall}$, have to be considered as well. Their calculation will be explained in section 6.2.3.3 .

The fouling factor f_p is used to calibrate and control the heat flux into the nodes. It can be different for every pipe in the gas node. For example, by setting the fouling factors of all pipes to 0, the heat flux into all nodes can be “turned off”.

α_r is the heat transfer coefficient between the flue gas and the outer wall of the pipe. It can be different for every row. Its calculation is described in the following chapter.

6.2.3.2 Calculation of Heat Transfer Coefficients

This section according to [15]. In general, the outer heat transfer coefficient α of parallel pipes in a bundle can be calculated from its Nusselt number:

$$\mathrm{Nu}_{bundle} = \frac{\alpha l}{\lambda}$$

In this definition, $l = \frac{\pi}{2} d$ is the characteristic length (d being the outer pipe diameter) and λ is the thermal conductivity of the flue gas. The Nusselt number of the bundle can be calculated from the Nusselt number of a single pipe

$$\mathrm{Nu}_{bundle} = f_A \mathrm{Nu}_{single}$$

wherein f_A is a constant factor considering the arrangement of single tubes in the bundle. It is calculated using the geometrical parameters shown in figure 30.

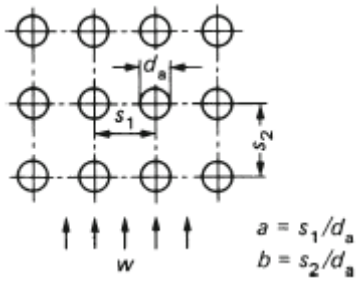

Figure 30: Geometrical Parameters for the arrangement Factor

$$f_A = 1 + \frac{0.7(b/a - 0.3)}{\psi^{1.5}(b/a + 0.7)^2}$$

$$\psi = 1 - \frac{\pi}{4a}$$

ψ is the ratio of empty space to total volume and will be called “void fraction” from this point on. The arrangement factor f_A takes into account the higher gas turbulence within the bundle compared to a single tube, which decreases the boundary layer thickness at the tube walls and therefore improves heat transfer. Because of that, f_A is always greater than 1.

This higher turbulence at a certain location inside the bundle is caused by the rows of tubes arranged before that point. From the first to about the fifth row, turbulence (and therefore the heat transfer coefficient) increases and stays constant after that. In that sense, the given formula for f_A is only valid from the fifth row onward and f_A is lower before that. It is suggested by [15] that the mean arrangement factor for bundles with less than 10 rows is approximately:

$$f_{A,m} = \frac{1+(R-1)f_A}{R}$$

Where R is the total number of rows. This implies that the arrangement factor is increasing by an order of 2 from row 1 to row 5, as shown in figure 31.

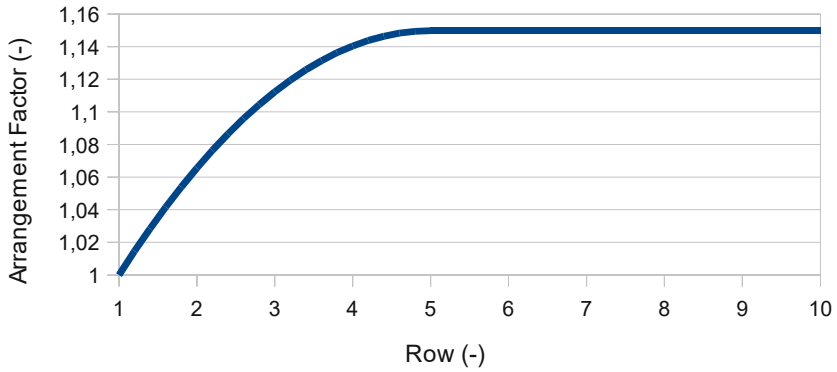

Figure 31: Arrangement Factor as a Function of Row Number

The graph shows a second order interpolation of the arrangement factor for the first 5 rows with a smooth transition to a constant arrangement factor after that. The corresponding function is:

$$f_{A,r}(r) = \frac{1-f_A}{16}\left(r^2-10r+25\right)+f_A \qquad 1 \le r \le 5$$

$$f_{A,r}(r) = f_A \qquad r > 5$$

This function was used to calculate different arrangement factors $f_{A,r}$ at different rows within the bundle, which causes different heat transfer coefficients at each row, as shown in figure 29.

Back to the Nusselt number. To calculate the Nusselt number of a single pipe Nu_{single}, [15] suggests the equation of Gnielinski:

$$\mathrm{Nu}_{single} = 0.3 + \sqrt{\mathrm{Nu}_{lam}^2 + \mathrm{Nu}_{turb}^2}$$

$$\mathrm{Nu}_{lam} = 0.664\sqrt{\mathrm{Re}_\psi}\sqrt[3]{\mathrm{Pr}}$$

$$\mathrm{Nu}_{turb} = \frac{0.037\,\mathrm{Re}_\psi^{0.8}\,\mathrm{Pr}}{1+2.443\,\mathrm{Re}_\psi^{-0.1}\left(\mathrm{Pr}^{2/3}-1\right)}$$

The Prandtl number Pr is calculated automatically by the simulation software as a substance-specific variable. The Reynolds number Re_ψ has to be calculated with the mean flow velocity of the gas in the empty space around the tubes using the void fraction ψ calculated before:

$$\mathrm{Re}_{\psi}=\frac{w\,l}{\psi\,\nu}\sin(\varphi)$$

Wherein w is the velocity of flue gas before entering the bundle, ν is the kinematic viscosity of the flue gas and φ is the angle at which the flue gas flows in respect to the tube axis. The angle is 90 ° in the case of the old bundle geometry and 92.3 ° for the new bundle geometry. The actual influence on Re_{ψ} is very small.

All substance-specific variables in the equations, which are Pr , λ and ν , have to be calculated at the mean gas temperature in the bundle, $T_{G,m}=\left(T_{G,in}-T_{G,out}\right)/2$.

6.2.3.3 Heat Transfer into Hanger Tubes and Water Walls

The complete energy balance of each gas node does not only include heat transfer to the convective evaporator bundle but also to the hanger tubes and water walls of the third pass. Not considering those heat fluxes would result in incorrect outlet and mean temperatures of the gas nodes, which are required for the correct calculation of heat flux into the bundle.

According to [16], thermal transmittance k between the flue gas and the hanger tubes / water walls can be approximated as a fraction of thermal transmittance between the flue gas and the heated bundle:

$$k_{hangers} \approx 0.6\, k_{bundle}$$

$$k_{wall} \approx 0.4\, k_{bundle}$$

Because the water in the bundle is boiling, its inner heat transfer coefficient is extremely high, making the outer heat transfer coefficient the dominant factor for thermal transmittance. It is therefore approximated as:

$$k_{bundle} \approx 0.97\, \alpha$$

The heat transfer coefficient α was calculated the same way as in section 6.2.3.2 , with the arrangement factor f_A . The factor 0.97 comes from experience.

The heat transfer areas of the hanger tubes and water walls are calculated using the sketch in figure 32:

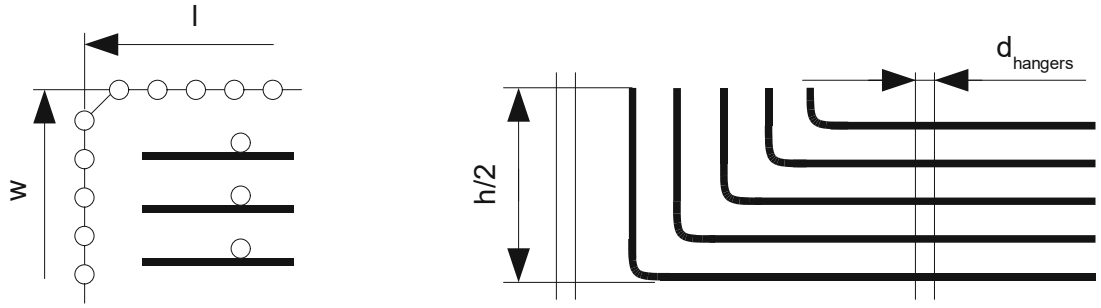

Figure 32: Sketch of hanger tube and water wall geometry

$$A_{hangers} = 122\, d_{hangers}\, \pi\, h$$

$$A_{wall} = 2\, h\, (w + l)$$

With $d_{hangers}$ being the outer diameter of the hanger tubes, h the total height of the bundle, and w as well as l the width and length of the third pass. The factor 122 comes from the total number of hanger tubes in the pass (2 per vertical row of the convective evaporator bundle).

The heat transfer areas of the hanger tubes and water walls were distributed evenly across all gas nodes, even though the inner gas nodes (sections 9.2 and 9.4 in figure 28) only have 2 neighboring water walls as opposed to the outer gas nodes (sections 9.1 and 9.3). This was done to ensure uniform heat fluxes and therefore gas temperatures in all subsections in stationary status when setting equal gas temperatures at their inlets. The actual influence of this is expected to be very small.

Since section 9.4 has one vertical row more than all the other subsections of the bundle (see figure 28), uniform distribution of the heat transfer areas has to be done in the following way:

$$A_{G,hangers/wall} = \frac{1}{2} A_{hangers/wall} \cdot \frac{16}{61} \qquad for\ section\ 9.4$$

$$A_{G,hangers/wall} = \frac{1}{2} A_{hangers/wall} \cdot \frac{15}{61} \qquad else$$

With $A_{G,hangers/wall}$ being the heat transfer area of the hangers / the water wall for gas node G.

Using the previous variables, the heat fluxes into the hanger tubes and water walls can be easily calculated for each gas node:

$$\dot{Q}_{G,hangers} = 0.6 \cdot 0.97\, \alpha\, A_{G,hangers} \frac{T_{G,in} - T_{G,out}}{\ln\left(\frac{T_{G,in} - T_{sat}}{T_{G,out} - T_{sat}}\right)}$$

$$\dot{Q}_{G,wall} = 0.4 \cdot 0.97\, \alpha\, A_{G,wall} \frac{T_{G,in} - T_{G,out}}{\ln\left(\frac{T_{G,in} - T_{sat}}{T_{G,out} - T_{sat}}\right)}$$

The fraction on the right side of both equations is the logarithmic mean temperature difference.

T_{sat} is the saturation temperature at steam drum pressure.

6.2.3.4 Summary and Dynamic Algorithm

To summarize, the following variables can be different at different parts of the convective evaporator bundle, also see figure 29:

- Flue gas inlet and outlet temperatures are different for every gas node.
- Local flue gas temperatures are different for every horizontal row of tubes within a gas node and for vertical and horizontal parts of those tubes.
- Heat transfer coefficients are also different for every horizontal row of tubes within a gas node, but they are identical for the horizontal and vertical parts of tubes within that row.
- Heat transfer areas and outer tube wall temperatures are different for every node within a pipe.
- No heat is transferred to the bends of any pipe, since that would have required an unreasonable effort, as explained in section 6.2.1 .
- Heat transfer areas of hanger tubes and water walls are evenly distributed over the width of the bundle, as explained in section 6.2.3.3 .

During the simulation, the software follows this algorithm to calculate the heat transfer from the flue gas to the convective evaporator bundle:

1) Calculate the heat transfer coefficients α_r and interpolate the flue gas temperature (vertical / horizontal parts) for all horizontal rows in a gas node G.
2) Calculate the heat flux into every node within the gas node, $\dot{Q}_{G,n} = A_n \alpha_r \left(T_{G,n} - T_{w,n} \right) f_p$, considering heat transfer area A_n , fouling factor f_p and current outer wall temperature $T_{w,n}$.
3) Based on that outer heat flux, the current heat flux from the inside of the pipe wall to the water and the heat capacity of the tube wall, the simulation software calculates a new outer wall temperature.
4) Sum up all the heat fluxes into the nodes within the gas node, add the heat fluxes into the hanger tubes and water walls, and subtract all of that from the gas node. Based on the heat capacity of the flue gas, the simulation software calculates a new gas temperature at the outlet of the gas node.
5) Repeat for every gas node.
6) Repeat for every time step.

6.3 Hanger Tubes

The hanger tubes of the third pass (short: hanger tubes) depart from the same vertical headers as the tubes of the convective evaporator bundle (see figures 26 and 27 in chapter 6.2.1) and span across the entire height of the pass. They are divided into the same subsections as the convective evaporator bundle, see figure 33 (compare with figure 28 on page 42):

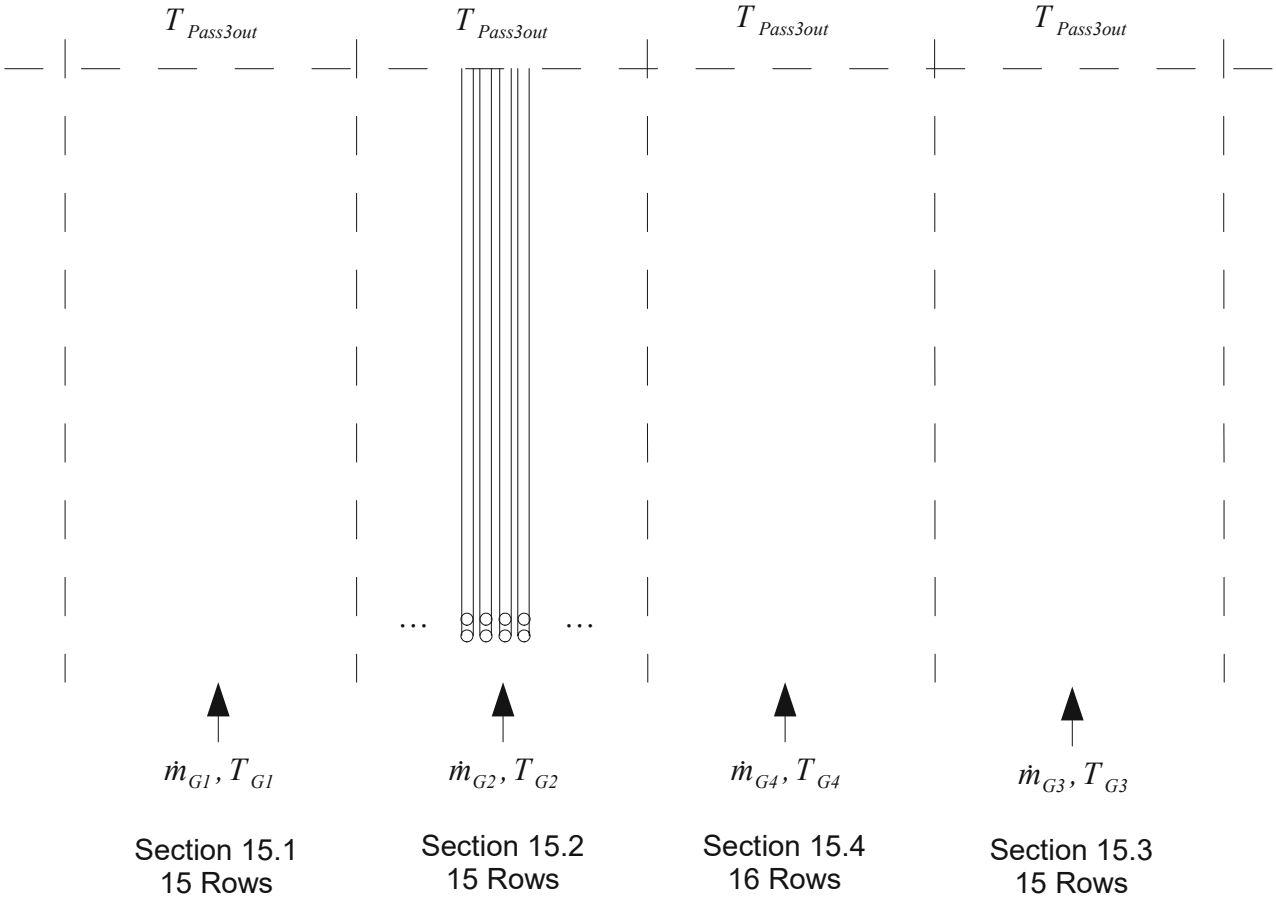

Figure 33: Illustration of the Model for the Hanger Tubes

The parameters of the flue gas at the inlet of each section are the same as at the corresponding sections of the convective evaporator bundle, but the flue gas temperature at the outlet of the third pass $T_{Pass3out}$ is the same for every subsection of hanger tubes. This way it is possible to consider uneven flue gas temperatures at the beginning of the pass, while assuming that mixing of the flue gas along its way through the pass results in a homogenous gas temperature at the end of the pass.

Using the flue gas temperatures at the inlet and outlet of each subsection, a similar approach as in chapter 6.2.3.3 was made to calculate the heat flux into the hanger tubes:

$$\dot{q}_{hangers,i} = 0.6 \cdot 0.97 \, \alpha_i \frac{T_{G,in,i} - T_{Pass3out}}{\ln\left(\frac{T_{G,in,i} - T_{sat}}{T_{Pass3out} - T_{sat}}\right)}$$

$\dot{q}_{hangers,i}$ is the heat flux density (SI unit W/m²) into a subsection of hanger tubes (i = 1..4) in respect to the outer heat transfer area of the tubes. The heat transfer coefficient α_i is approximated to be the same as at the upper side of the corresponding subsection of the convective evaporator bundle. As explained in chapter 6.2.3.3 , the factor $0.6 \cdot 0.97$ turns α_i into an approximation for the thermal transmittance of the hanger tubes. The factor on the far right side is the logarithmic temperature difference, wherein $T_{G,in,i}$ is the gas temperature at the inlet of subsection i and T_{sat} is the saturation temperature at steam drum pressure.

At a gas temperature at the entrance of the third pass of 710 °C the outlet temperature $T_{Pass3out}$ is 500 °C [8]. Assuming a constant dimensionless temperature change P of

$$P = \frac{T_{G,in} - T_{Pass3out}}{T_{G,in} - T_{sat}} = 0.507 \,,$$

the outlet temperature of the third pass can be calculated for different inlet temperatures, specifically for inlet temperatures of 630 °C and 550 °C (model parameters as explained in chapter 6.1.3):

$$T_{G,in} = 630\,°C: \qquad T_{Pass3out} = 460.58\,°C$$

$$T_{G,in} = 550\,°C: \qquad T_{Pass3out} = 421.16\,°C$$

6.4 Main Feeding and Rising System

Figure 34 shows a sketch of the main feeding and rising system, that is the feeding and rising system of the convective evaporator bundle and some other heat exchangers (chapter 6.5) connected to the same down comer as the bundle. A similar overview was shown in figure 16 on page 16, however, this one also demonstrates some specifics of the model.

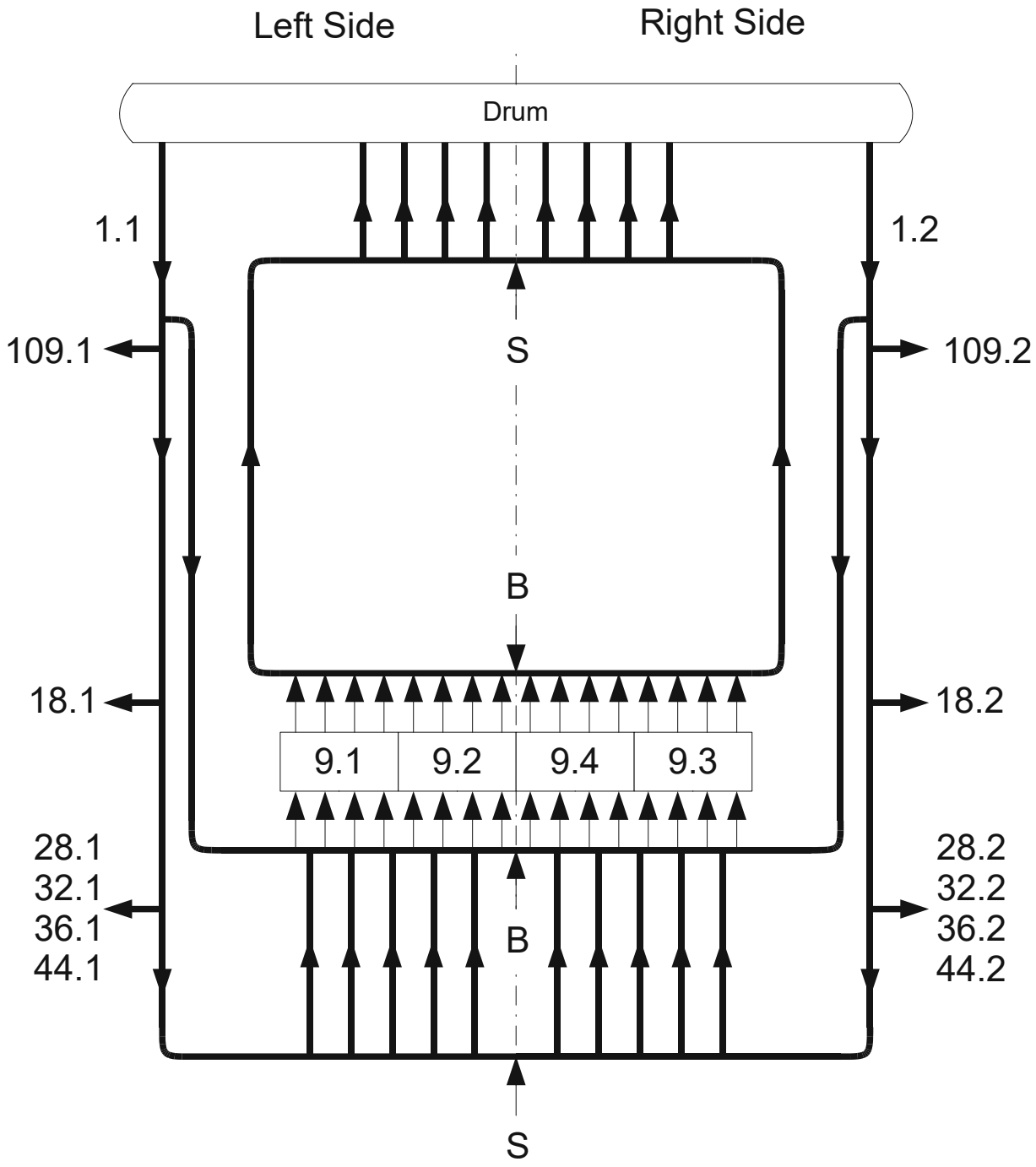

Figure 34: Sketch of the Main Feeding and Rising System

The section numbers are the same as in the Flowtran calculations, numbered using the scheme described in section 6.1.2 . The arrows show flow direction in normal (intended) operation. From each side of the steam drum, down comers (numbers 1.1 and 1.2) lead down to the bottom of the feeding system, where they both join again in a horizontal header. On their way down, several feeding pipes branch off to some of the residual heat exchangers. Additionally, feeding tubes branch off from each down comer and join right below the convective evaporator bundle (numbers 9.1-9.4). They constitute the horizontal header from which the vertical headers of each row of the convective evaporator bundle depart, as explained in section 6.2.1 . The bottom 2 horizontal headers are connected by 5 tubes on each side.

When leaving the convective evaporator bundle, the vertical headers join again in a horizontal header right above the bundle. From there, tubes from both sides of the header lead to another horizontal header higher up, from which riser tubes lead back to the steam drum.

The points marked with “B” in figure 34 are the locations of the blind plates already mentioned in chapter 6.1.3 . They separate the horizontal headers right below and above the convective evaporator bundle into a left and right side. Sections 9.1 and 9.2 are connected to the left side while sections 9.3 and 9.4 are connected to the right side. Figure 35 shows a design drawing of those blind plates.

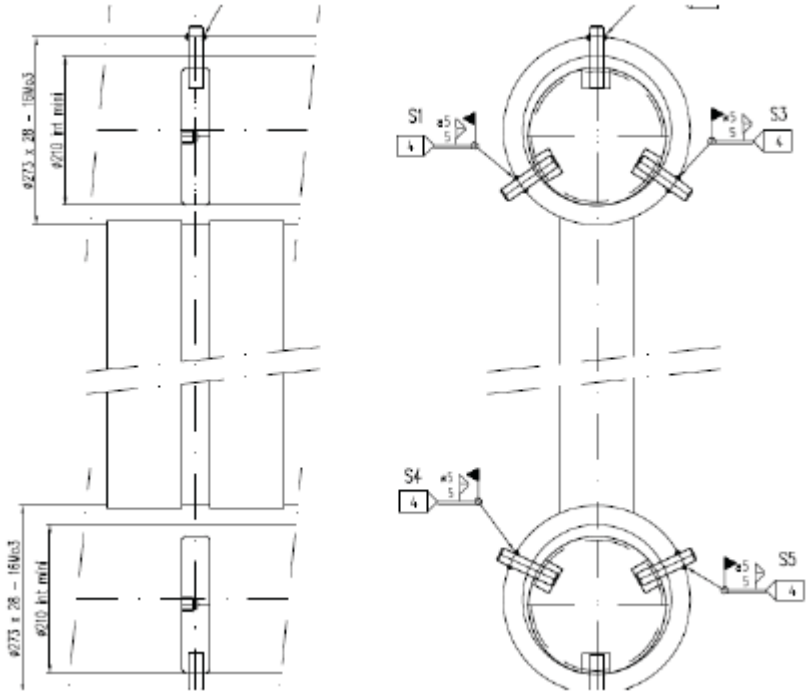

Figure 35: Design Drawing of the Blind Plates [9]

Unfortunately, figure 35 is in poor quality. One can see that the blind plates are actually “imperfect”, meaning that they do not block mass flow between the left and right sides completely. It is

estimated by [9] that the form loss coefficient for flow through the imperfect blind plates is between 200 and 500. The form loss coefficient in the model was set to 350.

The points marked with “S” in figure 34 are the locations where the feeding / rising system was separated after experiencing heavy oscillations during hot startup experiments, as already mentioned in chapter 6.1.3 . To be able to conduct experiments with a separated, as well as a not separated feeding / rising system, a valve was put at these locations in the model.

All vertical pipes of the main feeding / rising system, which are all parts except the horizontal headers, were modeled as straight vertical pipes, even though they all have various numbers of bends in them. This reduced the effort for modeling those parts significantly. The higher pressure losses in those pipes compared to straight pipes were still taken into account, as explained in section 6.1.4 .

6.5 Residual Heat Exchangers

6.5.1 Flow Loop 1

Flow loop 1 was modeled on two different levels of precision (chapter 6.1.1): The *common* part, which includes the front and rear parts of flow loop 1, was modeled on level 1 and the *side* parts were modeled on level 2, which means that both sides were modeled separately. A sketch of the model of the common part is shown in figure 36.

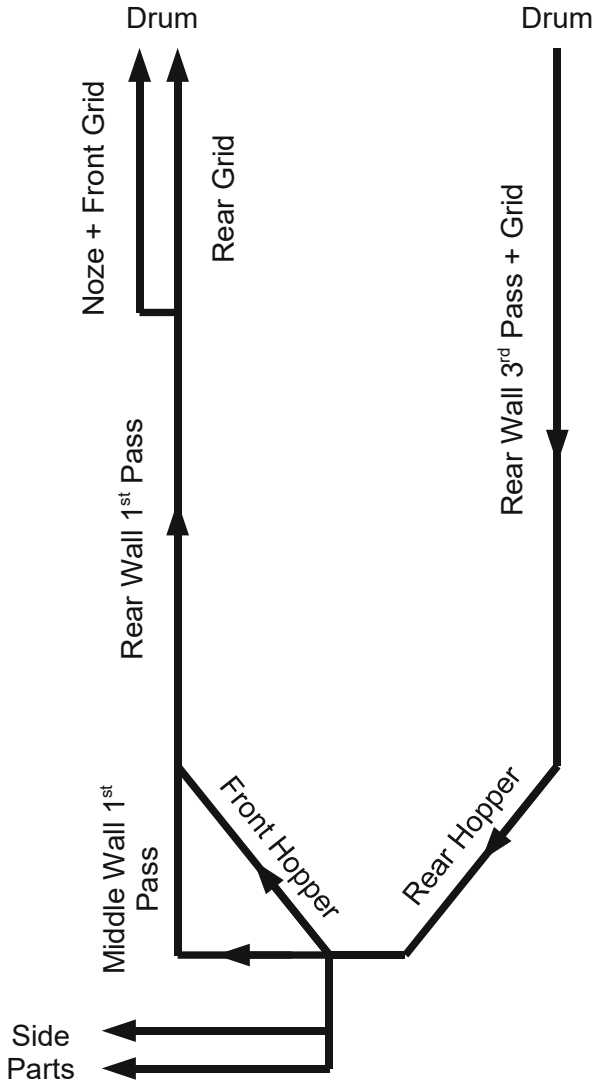

Figure 36: Sketch of the Model of the Common Part of Flow Loop 1

All sections in vertical parts of the sketch were also modeled as vertical parts, so only the rear and front hoppers have an inclination (55°) in the model. Form loss coefficients were set in such a way that mass flow in every section matched the one in the Flowtran results, as explained in chapter 6.1.4 . Of course, all headers between sections were also included in the model.

The side parts were modeled separately (level 2) because of their connection to the side water walls of the second pass, which were also modeled on level 2. Due to their inclined headers they required a little more attention to detail. Figure 37 shows a sketch of the model.

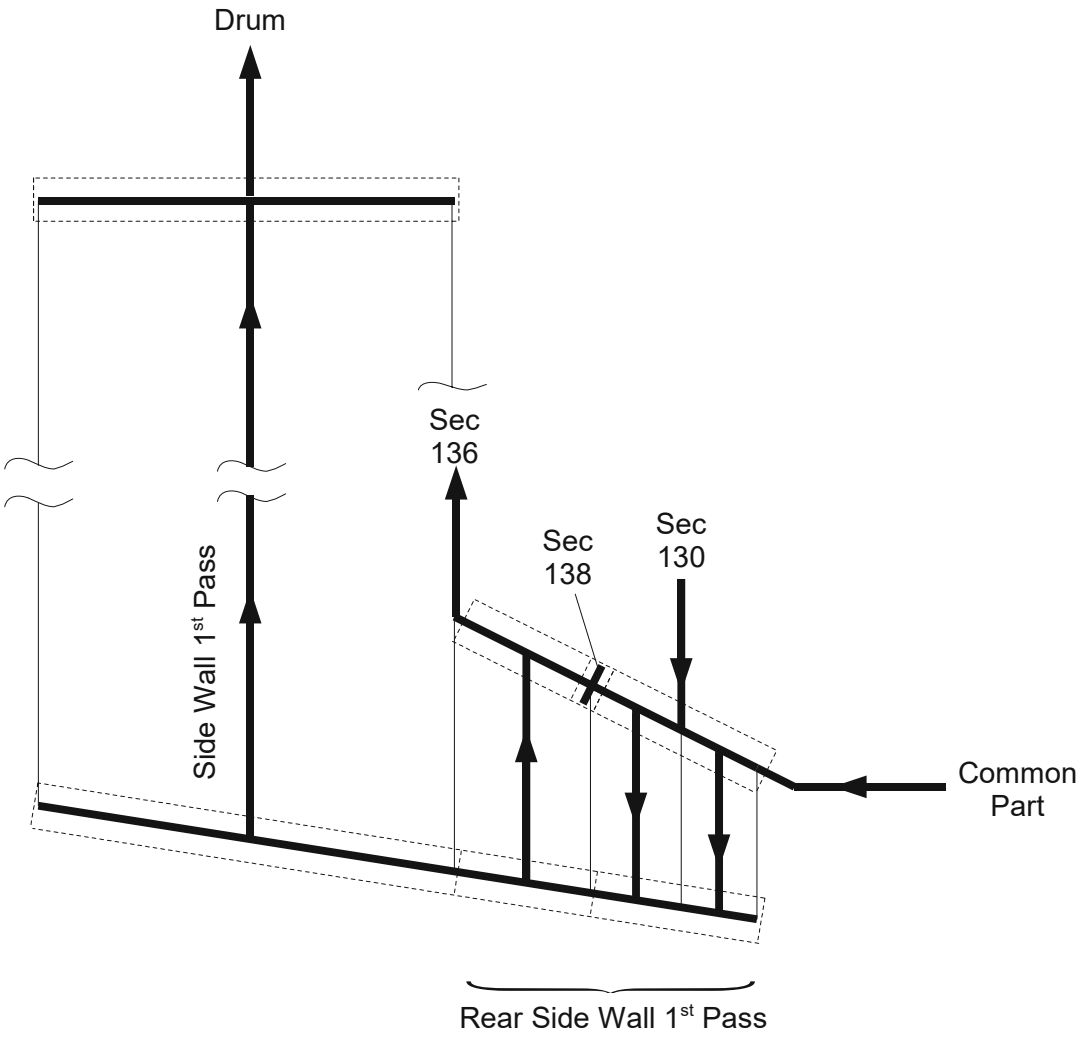

Figure 37: Sketch of the Model of the Side Parts of Flow Loop 1

All parts surrounded by dotted lines are parts of headers that were modeled as single nodes, which means that all parts connected to it are connected at the same elevation. It is not possible to consider smooth transitions of elevation along the length of an inclined header in the simulation software. Only the flow angles inside the nodes can be changed and were set accordingly. The division of headers follows the one in the Flowtran calculations by CNIM.

Lines between the headers represent water walls. The elevation of the headers was set to their middle value and the water walls were connected to them as single components of parallel pipes. The arrows show flow direction in a stationary state.

Section 138 is a diaphragm inside the top header of the rear side water wall of the first pass.

Figure 38 shows a sketch of it.

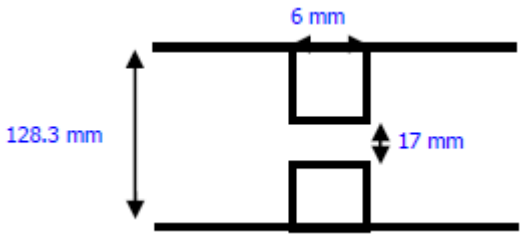

Figure 38: Sketch of Section 138

Its purpose is to evacuate steam accumulating in the lower part of the header to the top part before it enters the rear water wall of the third pass, where it would flow against the intended direction (downwards) and could cause problems with circulation.

Sections 130 and 136 are connections to the side water walls of the second pass connected to flow loop 1 (also see figure 17 on page 19). Section 130 is the connection between the lower part of the top header of the rear water walls of the first pass, and the bottom middle feeder of the side water wall of the second pass. Section 136 is *not* directly connected to the top part of the header (encircled by dotted lines in figure 37) but at a higher elevation at the very end of the header. It leads to the bottom upper middle feeder of the side water wall of the second pass.

As the side part of flow loop 1 is modeled separately, there are two identical parts (left and right side). Therefore, the left side is connected to sections 130.1 and 136.1 and the right side to 130.2 and 136.2.

All heat fluxes into sections of flow loop 1 (common and side parts) can be set as functions of time, but only for all sections at the same time. That means that the ratio of heat flux into a certain section to the total heat flux into all sections of flow loop 1 is constant. Because of that, changes of heat flux in sections further down the flue gas path, for example the rear water wall of the third pass, occur at the same time as at the beginning of the flue gas path, like the side water walls of the first pass. This is somewhat unrealistic, especially in the case of startups, but the influence on overall behavior and stability is assumed to be negligible.

6.5.2 Flow Loop 6

Flow loop 6 only contains the side water walls of the third pass. It was modeled on level 1 (chapter 6.1.1), so both sides of the water wall (left and right) were modeled together as a single component. Figure 39 shows a sketch of the model.

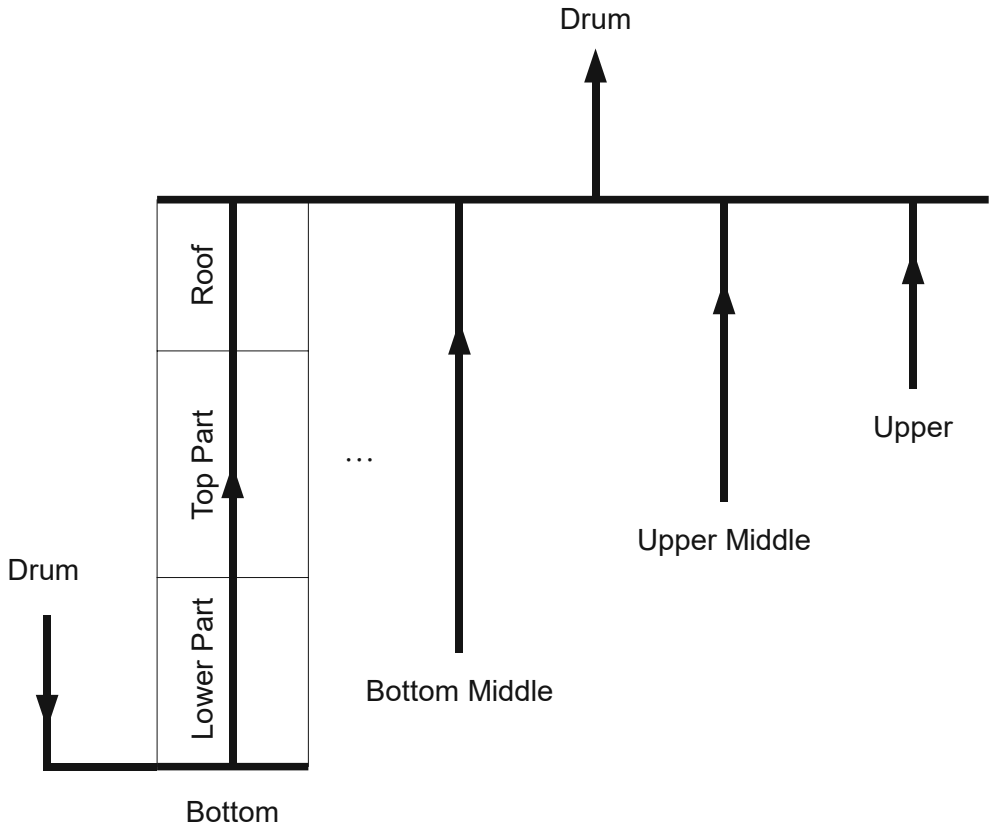

Figure 39: Sketch of the Model for Flow Loop 6

The side water walls of the third pass consist of 4 parts, *Bottom*, *Bottom Middle*, *Upper Middle* and *Upper*. See also figure 19 on page 21. Every one of those parts is divided into 3 parts, the lower and top part and the roof. The lower parts contain the bottom feeders, which are individually fed by the steam drum. They are located at different elevations for each part (Bottom, Bottom Middle,...). From there, the water walls go straight up to the point where they reach the convective evaporator bundle. The top parts then lead up to the beginning of the roof, which then connects to a common header for all 4 parts. The flow loop is closed by connections back to the steam drum.

All parts were divided into lower and top parts because of different heat flux densities (SI unit W/m²) into those parts. The division follows the one in Flowtran by CNIM. The total heat flux into all sections of flow loop 6 can be set as a function of time. The ratio of a sections heat flux to total heat flux is constant.

6.5.3 Others

All other residual heat exchangers are connected to the main feeding / rising system (chapter 6.4) and are modeled on level 2. They all consist of 3 basic components: down comer, heated part and riser, all of them modeled as straight vertical parts.

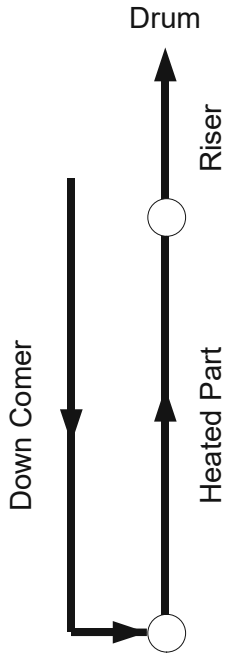

Figure 40: Basic Model of Residual Heat Exchangers

There are some minor differences between residual heat exchangers:

- *Front Water Wall 1st Pass:* One down comer from each of the main down comers both lead to a header, from which additional smaller down comers lead to a second header below. Then the heated part starts from there.
- *Rear Water Wall 2nd Pass:* One down comer from each of the main down comers both lead to a common header from which the heated part departs.
- *Intermediate Panels:* The down comers depart from the same header from which the heated part of the rear water wall of the second pass departs.
- *Side Water Walls 2nd Pass:* Several parallel modules are fed from the same location at the main down comers. Their heated parts lead to a common top header on each side (left and right side). Their model is very similar to the one used for flow loop 6 (figure 39), but they are modeled on level 2 (left and right side separate) and connected to the main down comers instead of the drum.

Heat fluxes of all parts can be set as functions of time.

6.6 Steam Drum

6.6.1 General

Figure 41 shows an overview of the model for the steam drum.

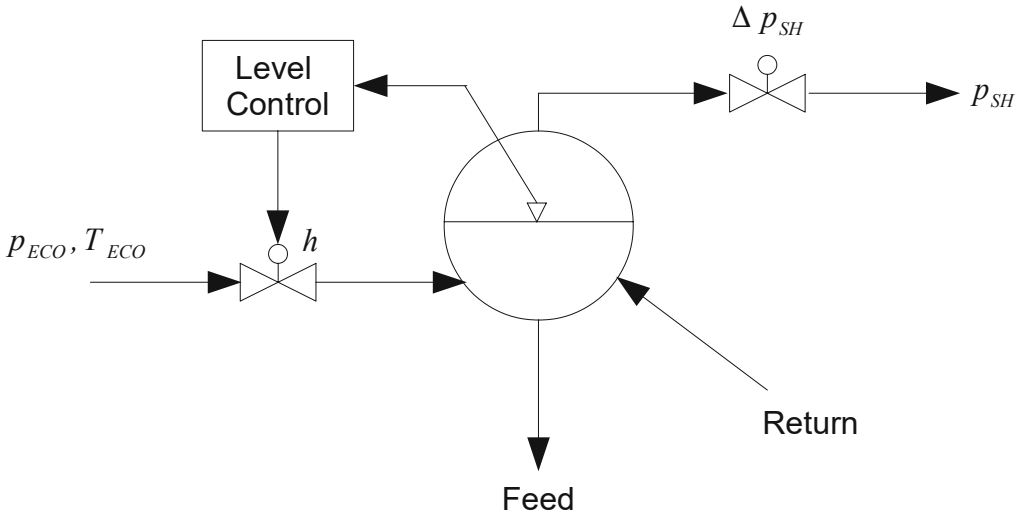

Figure 41: Sketch of the steam drum model

The pressure and temperature of the subcooled water coming from the economizer, as well as the pressure of superheated steam at the outlet of the steam generator are set as boundary conditions. The pressure of the economizer is set to 1 bar above the steam drum pressure to ensure that the pressure difference between the economizer and the steam drum is always positive. The temperature of the water coming from the economizer was set to 264 °C [8].

A valve determines the mass flow from the economizer into the steam drum. Its specific curve is linear, which means that the mass flow through the valve is a linear function of the valve position, as shown schematically in figure 42.

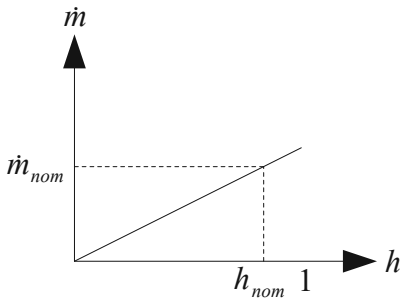

Figure 42: Specific Curve of the Valve controlling the mass flow into the steam drum

The valve position h is normalized between 0 (closed valve) and 1 (fully open valve). The nominal

valve position h_{nom} was set to 0.8 at a nominal mass flow of 30 kg/s, which is approximately the mass flow in stationary status (model parameter permutation 2). Since the pressure of the water coming from the economizer was set to always be 1 bar higher than the steam drum pressure, the nominal pressure loss of the valve was also set to 1 bar.

Level control includes measurement of the liquid level in the steam drum and a PD controller, controlling the valve in such a way that the liquid level is kept at 50% of drum diameter. This is explained in detail in the next chapter.

The pressure of superheated steam at the outlet of the steam generator was set to 75 bar [8]. To avoid modeling all the superheaters, the pressure drop between the steam drum and the outlet of the steam generator is modeled by a valve with a linear specific curve. The nominal pressure loss of the valve at a nominal mass flow of 30 kg/s was set to 7.4 bar, which is the pressure difference between the steam drum and superheated steam at the outlet of the steam generator in stationary state [8]. Variations of the steam drum pressure are performed by varying the pressure at the outlet of the steam generator.

6.6.2 Drum Level Control

Figure 43 shows a diagram of the feedback loop used to control the liquid level in the steam drum.

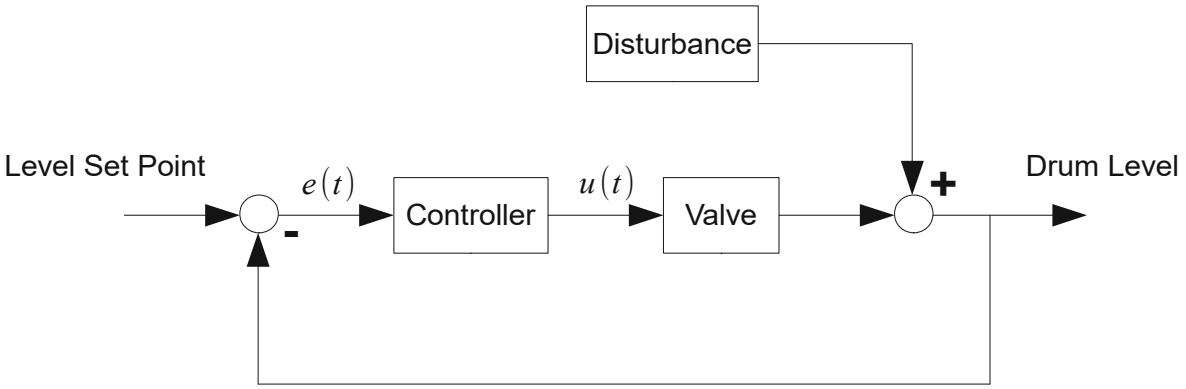

Figure 43: Control Loop for Drum Level Control

The difference between the drum level set point (usually 50% of inner drum diameter) and the current drum level is the error $e(t)$. The controller uses that to determine a manipulating variable $u(t)$ that changes the valve position, which influences the liquid level in the drum. Uncontrollable variables, such as, the returning mass flow from the evaporator, also contribute to the change of the liquid level and are called disturbances.

For the manipulating variable $u(t)$, the speed of change in valve position was chosen. This has the advantage that when in stationary state the error $e(t)$ becomes 0, the change in valve position $u(t)$ becomes 0 as well and the valve stays at its current position, letting through a constant mass flow. This would not be the case if the manipulating variable was chosen to be the valve position itself, because then the valve would be fully closed in stationary state ($e(t)=0$), but maintaining a stationary state requires a constant mass flow through the valve.

The current valve position $h(t)$ can be calculated from the speed of change in valve position $u(t)$:

$$h(t)=h(0)+\int_0^t u(t)\,dt$$

Because the change of liquid level is directly proportional to the valve position, it is already apparent that the valve adds an integral term to the control loop. Due to this, the controller was only given a proportional and a differential term:

$$u(t)=K_p e(t)+K_d\frac{de(t)}{dt}$$

The factors K_p and K_d were set empirically to $K_p=2$ and $K_d=25$. To avoid unrealistically high speeds of change in valve position, $u(t)$ was limited to $\pm 0.2\,\mathrm{s}^{-1}$.

7 Stationary Status

7.1 General

To verify the model, the results of the stationary status are compared with the results from Flowtran provided by CNIM. The configuration of the model has the permutation number 2 in the permutation matrix (table 3). Figures 44 to 47 sum up the comparison in the form of graphs.

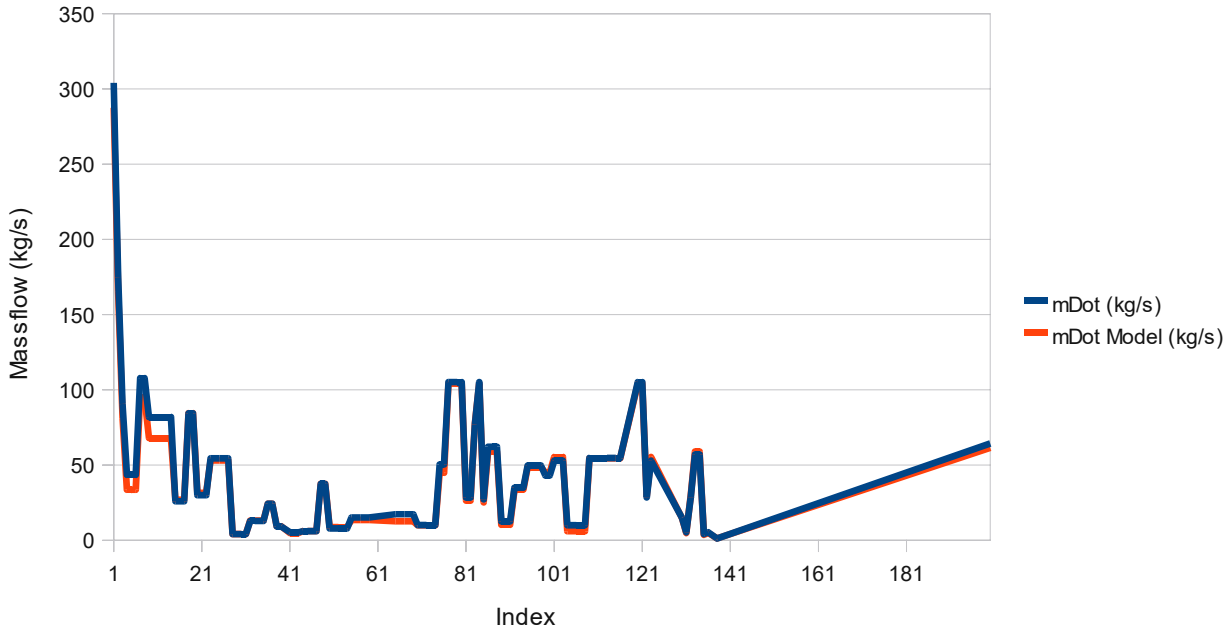

Figure 44: Mass Flow over Section Index for the Stationary Status

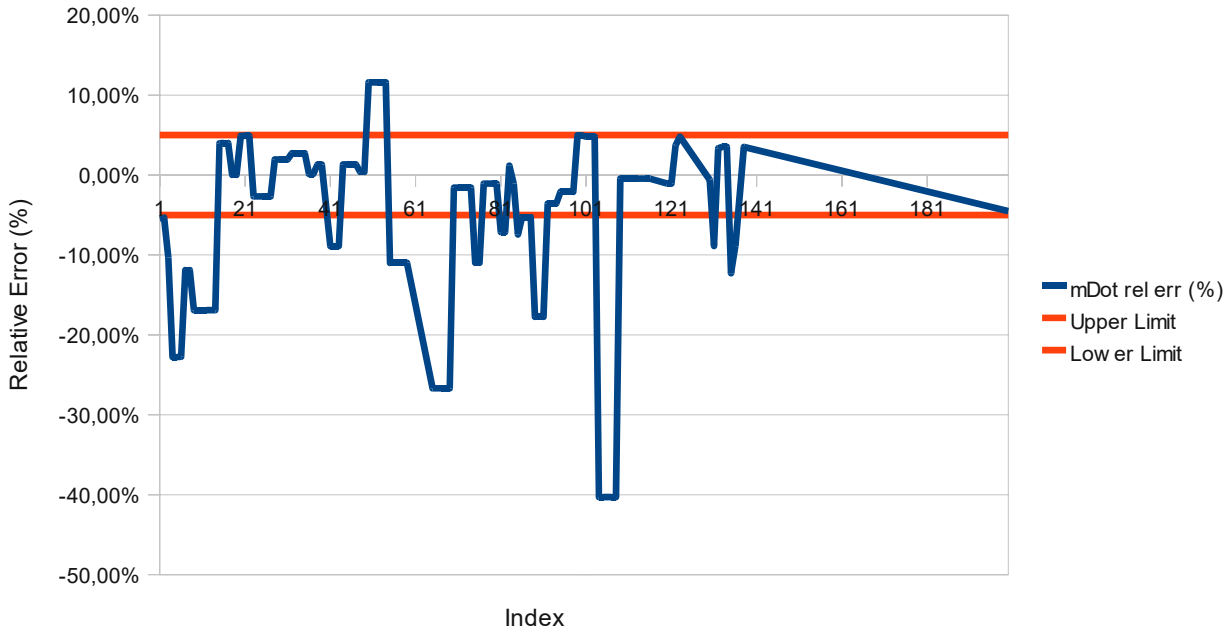

Figure 45: Relative Error of the Mass Flow over Section Index for the Stationary Status

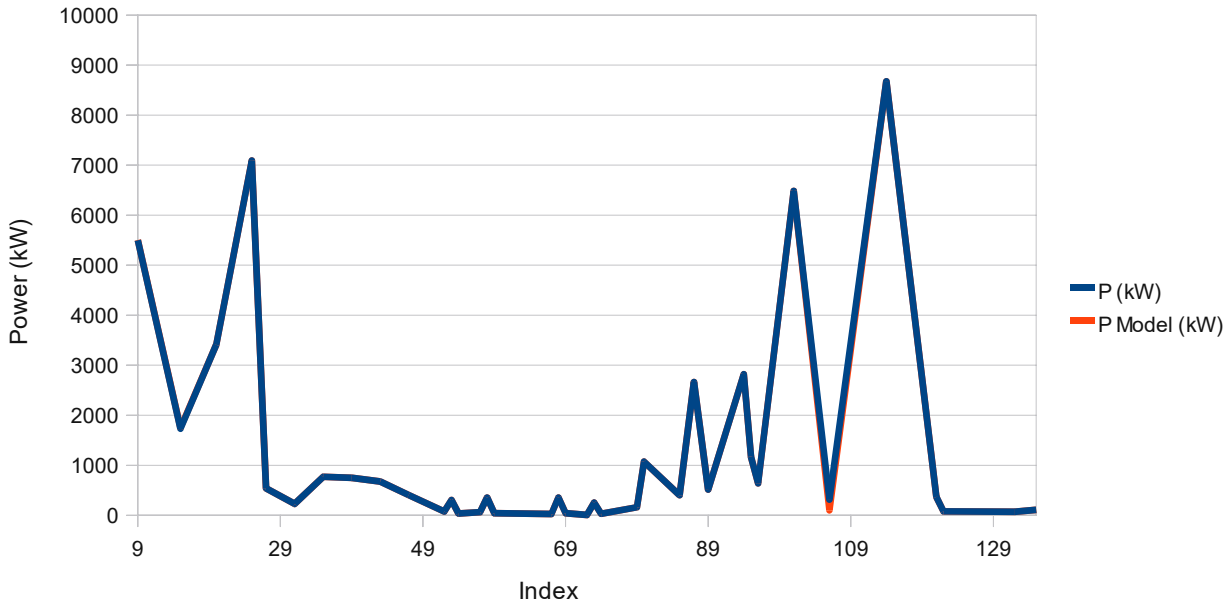

Figure 46: Heating Power over Section Index for the Stationary Status

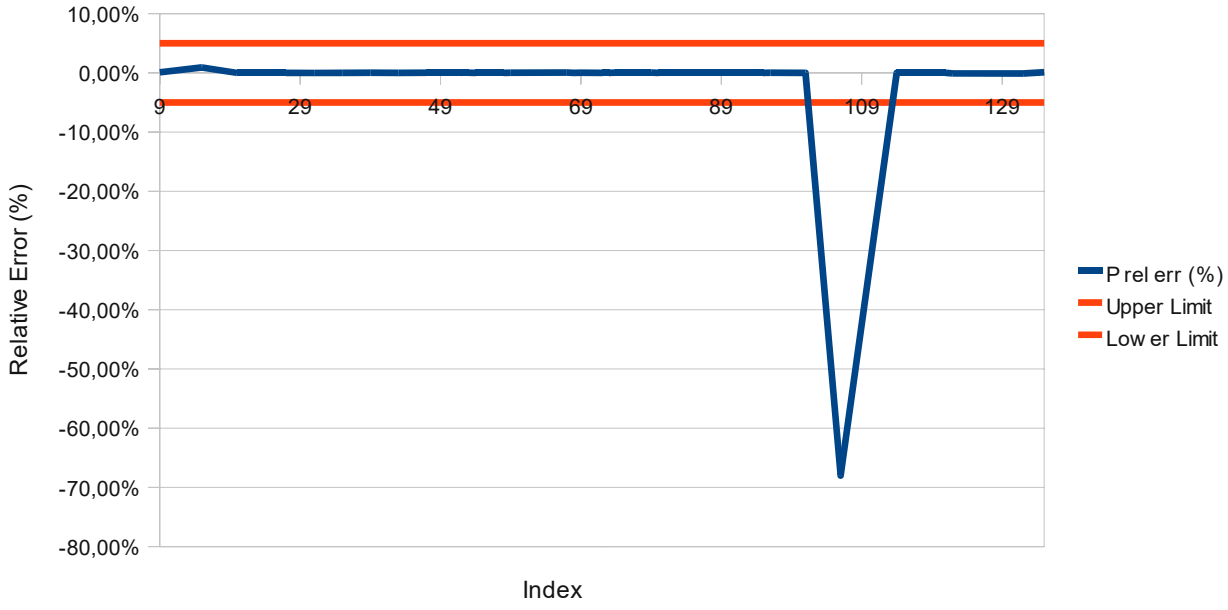

Figure 47: Relative Error of the Heating Power over Section Index for the Stationary Status

Blue lines in figures 44 and 46 represent the results from Flowtran, whereas red lines represent the ones from the model. Indices are the section numbers that were used in the Flowtran calculations. Chapter 6.1.2 explains how the sections were numbered.

Figures 45 and 47 show that the relative errors are quite far away from the +/- 5 % limit represented by the red lines for some sections. There are several reasons for that:

- It seems that Flowtran does not consider pressure losses due to bends (or other form loss) inside of sections, but only pressure losses due to pipe friction and at the border between sections, like headers. All sections on precision level 3, which include all sections with indices 1-15 and 200, directly consider form loss coefficients for bends at their exact locations, as described in chapter 6.1.4 , which causes generally higher friction pressure losses and therefore lower mass flows. Since this is closer to reality and the Flowtran results are not actual measurements, the deviations between the model and the Flowtran results are acceptable here.
- Mass flows in many of the sections are very small, in particular the side water walls of the second pass (indices 28-49), the rear grid of the first pass (indices 89-91), and parts of the rear side water walls of the first pass and their connections to the side water walls of the second pass (indices 130, 131, 135-138). Calibrating such small mass flows turned out to be very difficult and was not successful for some parts. However, because the mass flows are that small, the absolute deviations are very small as well.
- Heat fluxes in Flowtran are set as specific heat fluxes (SI unit W/m²) in respect to the heat transfer area of each section and Flowtran calculates the absolute heat fluxes using the dimensions of the respective sections. Unfortunately, faulty geometrical parameters were used for the Flowtran calculations by CNIM at almost all sections. Specifically, the sum of heights of sections building a loop (from the steam drum – back to the steam drum) does not equal zero. The deviation is fairly small for most loops, but this still leads to physically impossible results that can-not be recreated with the model (nor would it make sense to do so). Because the geometrical input is not correct, the absolute heat fluxes are not correct either. The actual geometry of the steam generator for the model was adopted from design drawings provided by CNIM.

  To preserve the energy balance of the steam generator, it was decided to set the same *absolute* heat fluxes as in Flowtran rather than the specific ones. This has the advantage that the total steam production and drum pressure are still the same as in Flowtran. The combined mass flows of flow loops 1-3 (indices 77, 22, 27, 49 and 116) are also very close to the Flowtran results, only the distribution of mass flow inside the flow loops is different because of the different specific heat fluxes. The experiments (chapter 8) show that drum pressure variations have a higher impact on the convective evaporator bundle than perturbations in the residual heat exchangers. This justifies the decision to set the same absolute heat fluxes (and with that, drum pressure) rather than the specific ones.
- The deviation of geometrical parameters to the actual geometry according to the design drawings is more severe at flow loop 6, which is why the mass flows are far away from the

Flowtran results in those sections (indices 50-76). However, since this part is not directly connected to the rest of the steam generator (besides the steam drum) and it was only modeled to take this part's heat capacity into account, as explained in chapter 6.1.1 , it should not be of major significance.

- The very small "Front Side Water Walls" of the first pass, index 106, start to overheat when setting the same heat flux for it as in Flowtran. To prevent this, the heat flux into them was reduced to about a third of the original heat flux. This is also the reason why the mass flow through them is so much smaller. Details on these oscillations follow in the next chapter.

7.2 Oscillations at Front Side Water Walls

The "Front Side Water Walls" of the first pass were a major source of problem within Apros modeling. They do not only overheat, they also cause mass flow oscillations with amplitudes of about 2.3 kg/s and never really reach a stationary status. This also has an impact on the rest of the circulation system, as figure 48 illustrates.

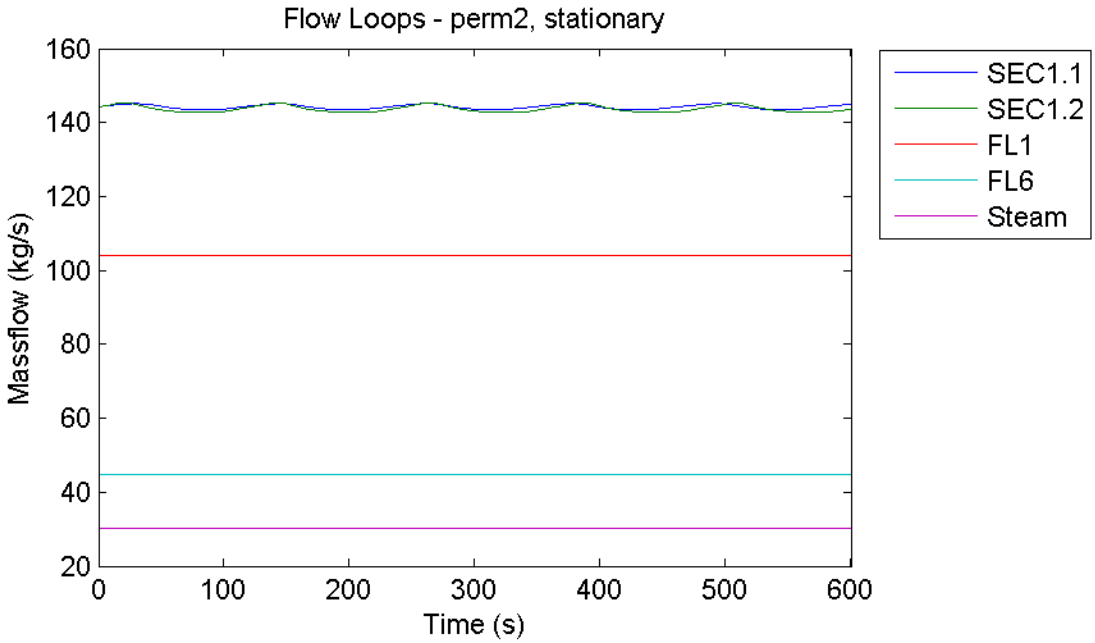

Figure 48: Overview of Mass Flows in Stationary Status

Figure 48 shows a general overview over the mass flows in the steam generator. Sections 1.1 and 1.2 are the common down comers of flow loops 2-5. FL1 is the mass flow of section 77, which is the down comer of that flow loop. FL6 is the mass flow of section 76, which is the rising system of flow loop 6 leading into the steam drum, representing the whole mass flow in this flow loop. The graph also contains the mass flow of saturated steam leaving the steam drum.

One can see that the oscillations in the "Front Side Water Wall" have some impact on the common down comers, sections 1.1 and 1.2, as well. While there is also some impact on flow loops 1 and 6, it is not noticeable in this graph. The effect is similar in the convective evaporator bundle, although with much lower amplitudes, as figure 49 shows.

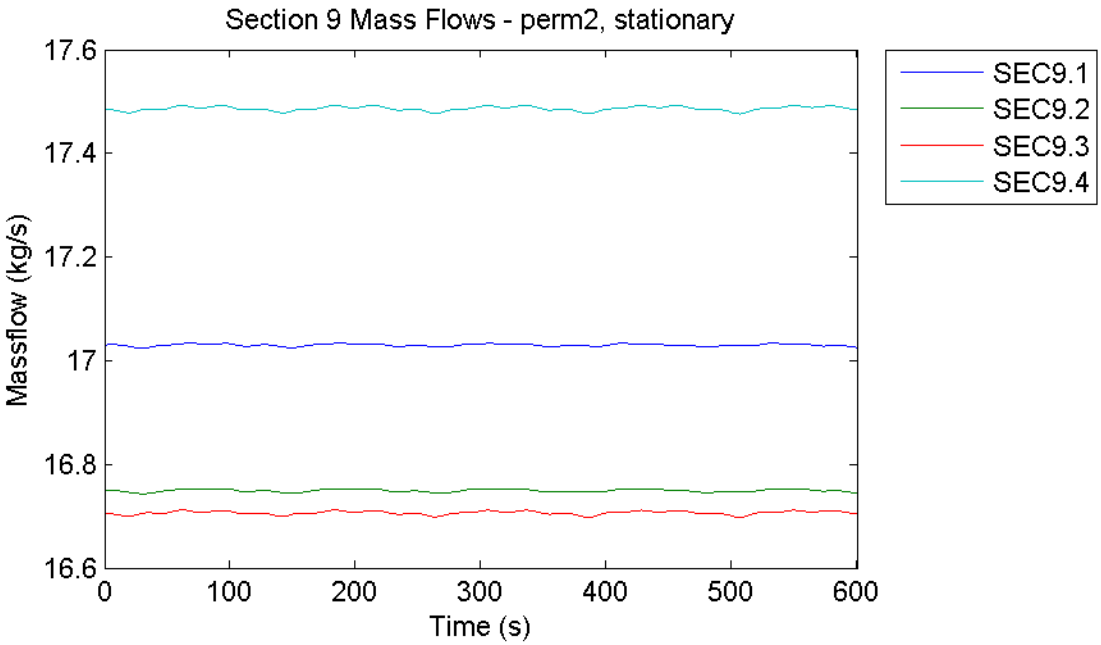

Figure 49: Mass Flow in different Subsections of the Convective Evaporator Bundle in Stationary Status

Figure 49 shows the collective mass flows through all tubes of subsections of the bundle, numbered from 1 to 4. The division follows the same scheme as shown in figure 28 for the gas side. Subsections 9.1 and 9.3 are the outer parts of the bundle on the left and right side respectively, while subsections 9.2 and 9.4 are the inner parts. Note that subsection 4 has one row more than the others, which is also why this part has such a high mass flow compared to the other parts. Graphs like this provide a quick overview over the mass flows inside the bundle without looking at every tube individually, which is of course possible, but often not necessary to detect instabilities.

One can see that the oscillations from the front side water wall of the first pass also affects the convective evaporator bundle, though the influence is very small. Heat fluxes, drum pressure and liquid level in the drum do not show any oscillations. The oscillations are most likely caused by the very long (about 25 m height difference) unheated risers following the front side water walls. Such designs are known to cause density wave oscillations (chapter 2.3.2).

The oscillations also show themselves in the static pressure differences and tube wall temperatures, as highlighted in figures 50 and 51.

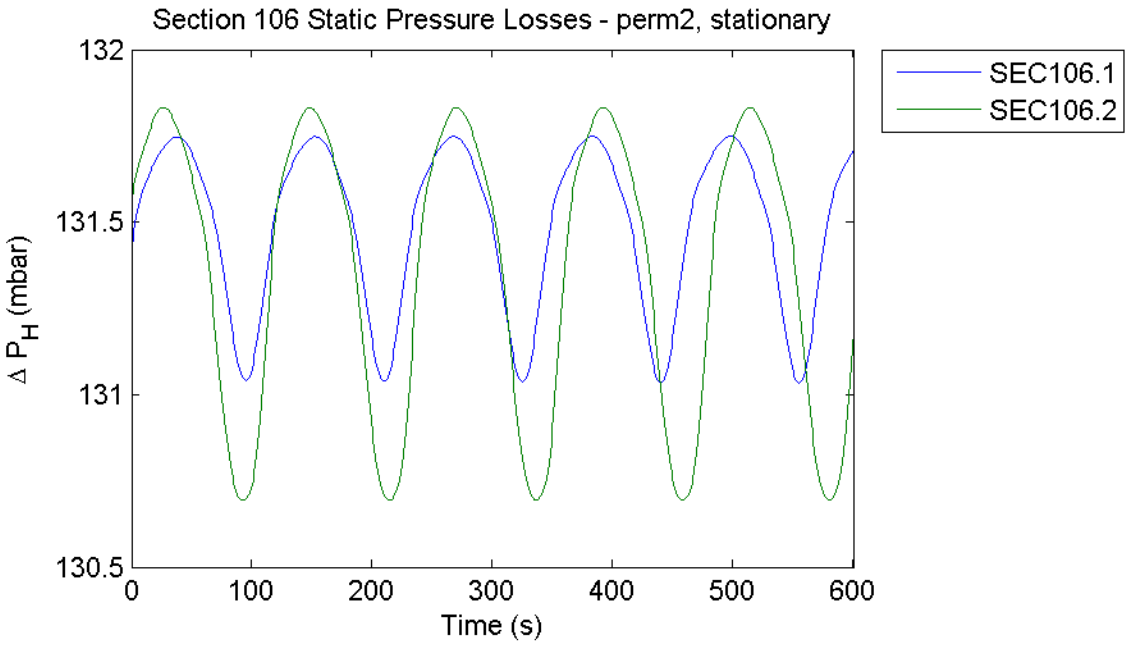

Figure 50: Static Pressure Differences in the Heated Parts of the Front Side Water Walls of the 1st Pass, Stationary Status

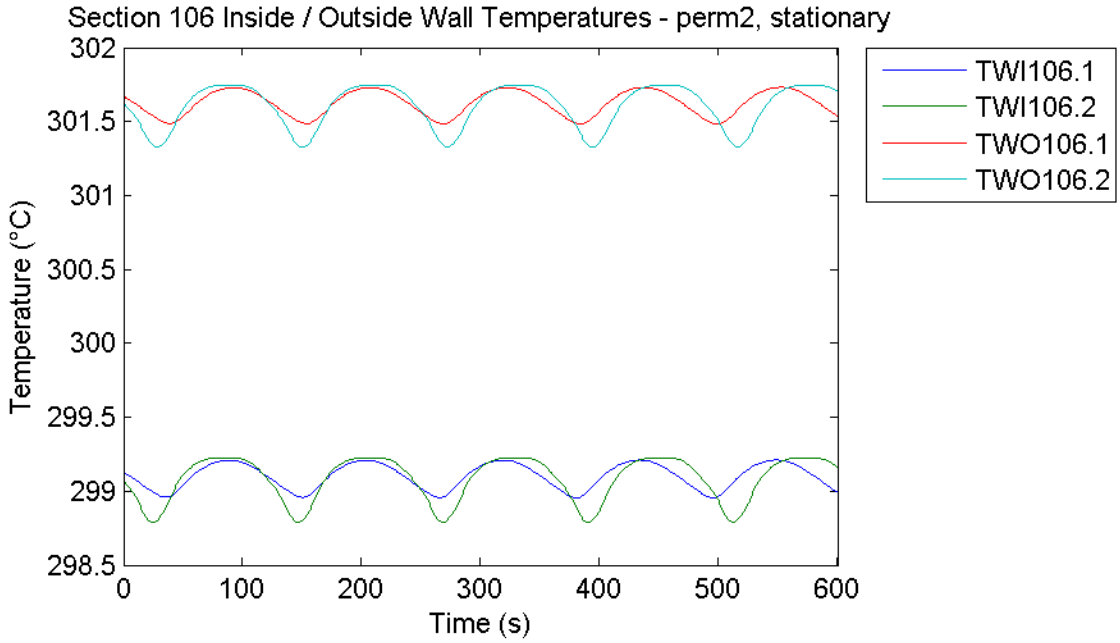

Figure 51: Wall Temperatures in the Heated Parts of the Front Side Water Walls of the 1st Pass, Stationary Status

The first graph shows the static pressure losses of the heated parts (section 106). Since the static pressure difference is only calculated as the product of fluid density, gravitational acceleration and height difference between the inlet and outlet of the section ($\rho g h$), and the gravitational acceleration and height difference are constants, the course of the static pressure loss follows the

course of fluid density. Lower fluid densities suggest higher mass fractions of steam.

First, it is interesting to see that the steam production is different between the both sides of the front side water wall: it is lower on the left side (index 1) than on the right side (higher static pressure differences mean lower steam quality), even though the heating and geometry of both sides is identical. The slow shift between the lines also shows that the frequencies of both oscillations are slightly different. However, overall steam production is very low: the steam quality never goes beyond 0.1 %.

This also serves as an explanation for the oscillations in the tube wall temperatures, figure 51: the rather low heat flux into the front side water walls can almost only be used to heat the subcooled liquid entering the heat exchanger to saturation temperature. For that reason, the tube wall temperatures primarily follow the mass flow oscillations.

When resetting the heat flux into the front side water walls to the one used in Flowtran (100 %) as an immediate step the oscillations stop, as figure 52 shows.

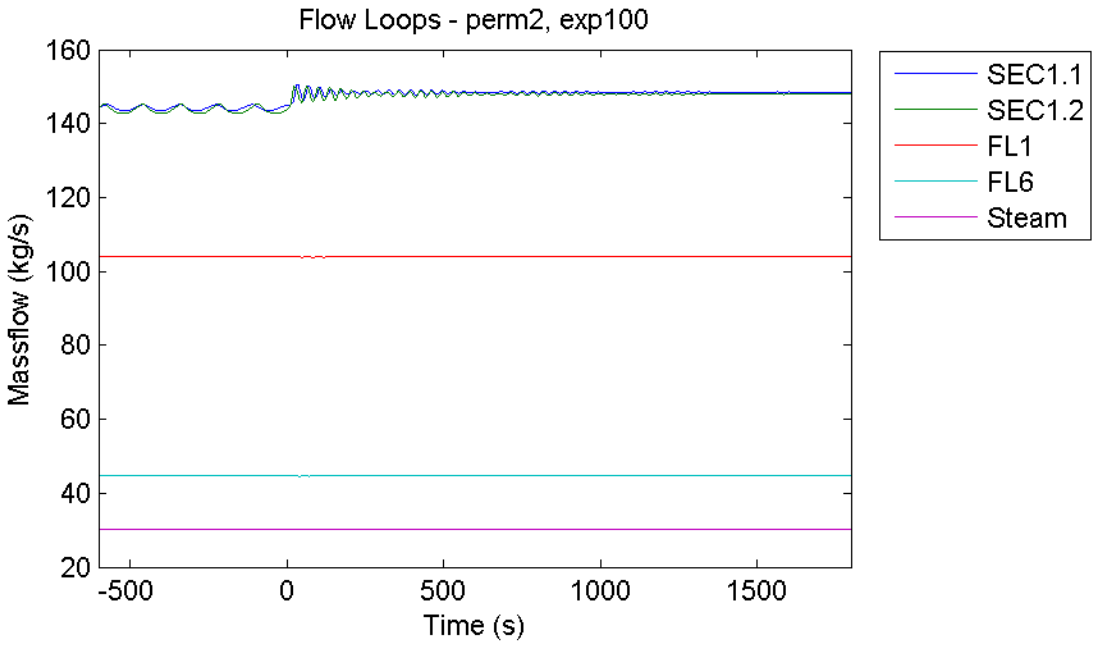

Figure 52: Overview of Mass Flows when resetting the heat flux into the Front Side Water Walls to the Flowtran value (as a step)

This highlights that the front side water walls are generally unstable. When performing a startup, the oscillations always start, independent of the heat flux, but when using the heat flux given in Flowtran the tubes additionally overheat. This is why the heat flux into the front side water walls was reduced to about a third of the original value.

7.3 Other Phenomena

There are some other interesting phenomena that can already be observed in stationary status. First, the mass flow through the convective evaporator bundle is fairly small. This can lead to stratified flow in horizontal pipes, which would leave the upper side of the tubes uncooled and vulnerable to heat damages. As explained in chapter 2.2 , stratification is dependent on a modified Froude number, which puts the inertia of the steam in relation to its buoyancy, figure 53.

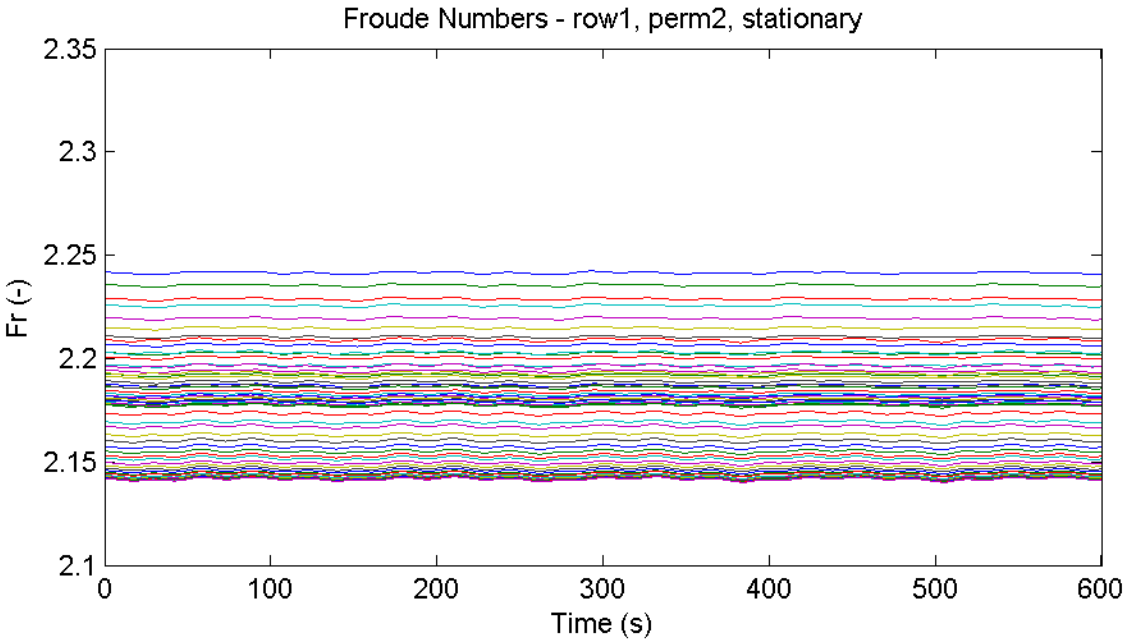

Figure 53: Froude Numbers of Pipes in the first horizontal Row in Stationary Status.

Figure 53 shows the Froude numbers of all tubes in the first horizontal row of the collective evaporator bundle (see figure 26 on page 40). All other rows show higher Froude numbers, so this is the critical case. According to [4], stratification is to be expected for Froude numbers below 3, which is clearly the case here. However, the critical mass fraction of steam for the occurrence of boiling crisis on the upper side of the pipes is at least 14 %, which is well above the actual steam quality of 3.3 % at the outlet of the tubes.

Local turbulence or other effects might still result in a stratified flow [4]. At lower gas temperatures at the inlet of the bundle (for example, model configuration permutation number 10, table 3), Froude numbers are lower (1.88-1.96), critical steam quality too (about 8.4 %), but so is the steam quality at the outlet of the bundle (2.2 %). The new bundle geometry shows generally better parameters (higher Froude numbers, higher critical heat fluxes, lower steam qualities).

Another phenomenon can be observed at the top horizontal header of the feeding and rising system (section number 14, the upper one marked with an S in figure 34 on page 53): because the feed only comes from the side and is a mixture of water and steam, the header essentially

functions as a centrifugal separator. The larger inertia of the liquid compared to the steam causes the liquid to flow further inwards than the steam. Due to this, the steam is primarily flowing from the header into the steam drum through the outer risers rather than the inner ones, as figure 54 shows.

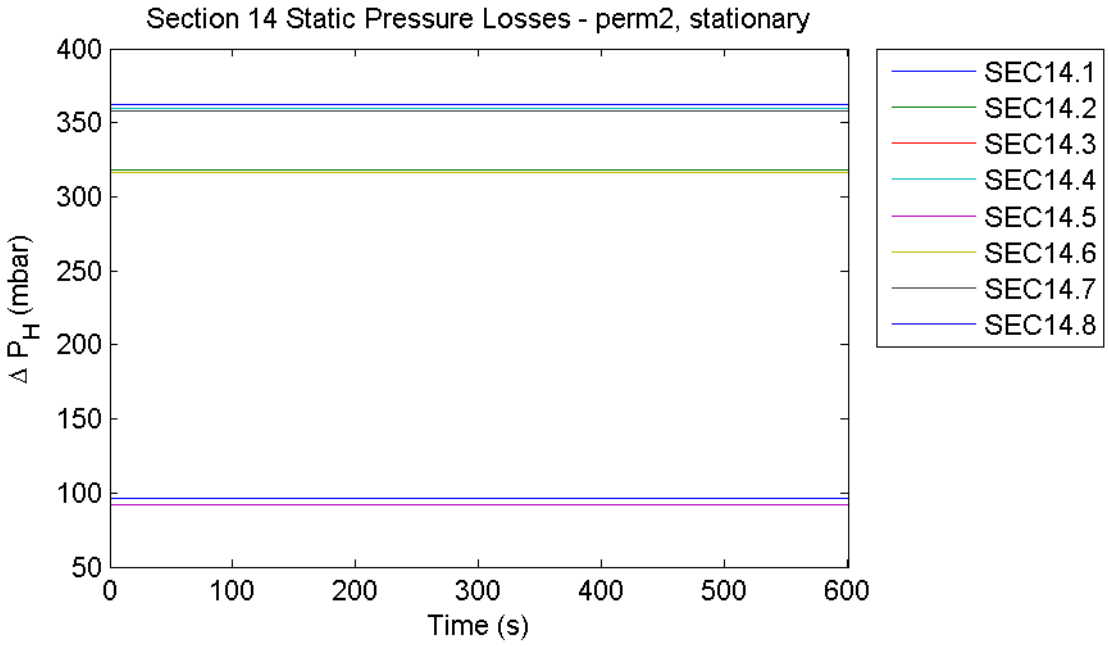

Figure 54: Static Pressure Losses of Top Risers – Perfect Blind Plates, Separated Feeding / Rising System, Final Inlet Gas Temperature 710 °C, Hot Startup over 10 min

The outermost risers, sections 14.1 and 14.5, have the highest mass fraction of steam (lowest density, therefore lowest static pressure losses), followed by the risers one spot to the middle, sections 14.2 and 14.6. The innermost risers, sections 14.3, 14.4, 14.7 and 14.8, transport almost no steam at all. The steam qualities are about 20 %, 1.3 % and 0.4 % respectively. This phenomenon is likely playing a role in the emergence of global circulations during hot startups, chapter 8.2.4 .

8 Experiments

8.1 Experiment Configurations

8.1.1 Basic Experiments

Some basic experiments were conducted for all model parameters (see table 3). They are designed to obtain a first overview over possible instabilities under certain circumstances by disturbing the system in a fairly severe way. If no instabilities occur under such harsh conditions, the system can be considered as being stable. If instabilities do occur, additional experiments can be conducted to further investigate the issue.

The following gives an overview over the conditions of all basic experiments:

- *Partial hot stream of flue gas:* This experiment investigates the influence of an uneven flue gas temperature across the width of the pass containing the convective evaporator bundle. For this, the flue gas temperature at the inlet of one subdivision of the bundle was increased by 100 °C, while the inlet temperatures of all other subdivisions was decreased by 50 °C, both linearly over a time period of 5 minutes. As an example, figure 55 shows an illustration of this for subsection 9.2:

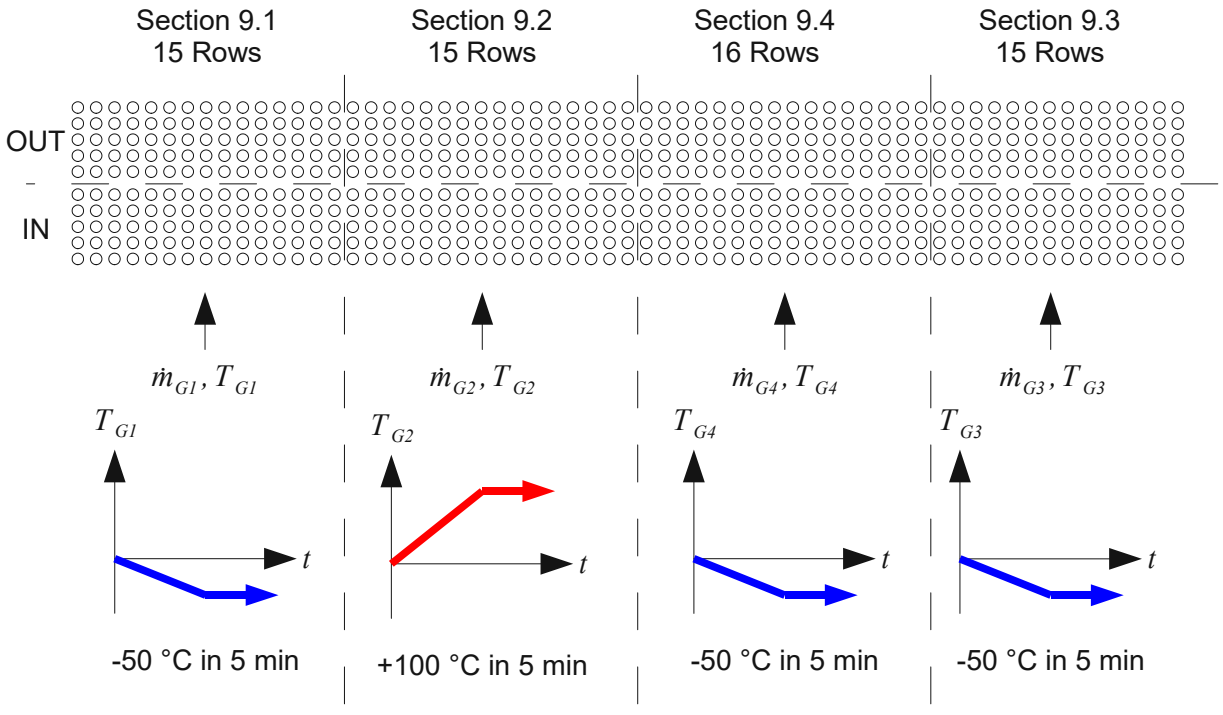

Figure 55: Experiment Configuration for a Partial Hot Stream of Flue Gas at section 9.2

- *Drum pressure variations:* To investigate the influence of drum pressure variations, the

pressure of superheated steam at the outlet of the steam generator was lowered / raised over a period of 5 minutes by 3.75 bar, which is equal to 5 % of the outlet pressure. Figure 56 illustrates the configuration of the experiment.

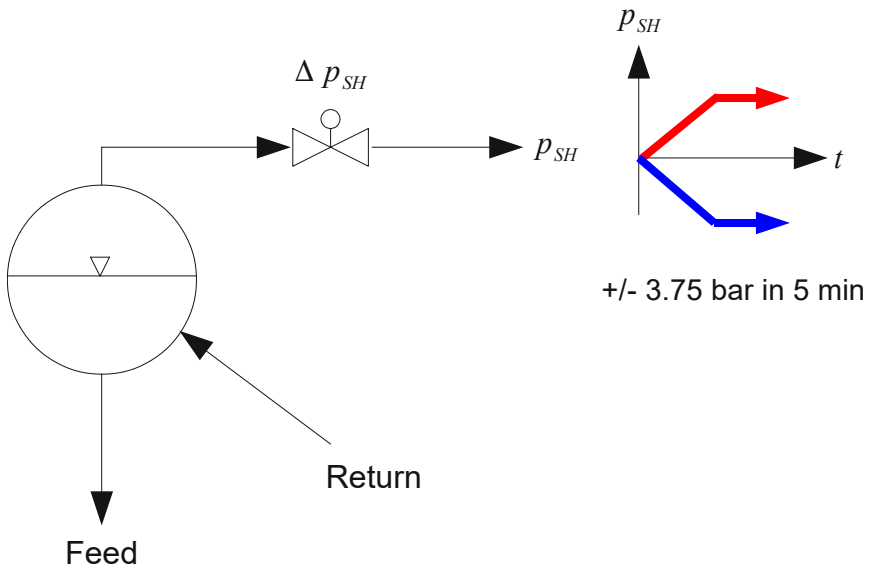

Figure 56: Experiment Configuration for Drum Pressure Variations

- *Sudden change of heat flux in residual heat exchangers:* The residual heat exchangers are those connected to the same down comers as the convective evaporator bundle. A sudden (positive) change in heat flux into one of those parts also leads to a higher mass flow in that part, which in turn could leave the convective evaporator bundle with not enough mass flow to be properly cooled. Such a sudden increase in heat flux can occur when parts of the fouling layer covering one of those heat exchangers breaks off, thereby suddenly improving the heat transfer coefficient.
  To investigate this, experiments were conducted that increased the heat flux separately by 20% of the normal heat flux in stationary status in each of the residual heat exchangers: the front water wall of the first pass, the left, right and rear water walls of the second pass and the intermediate panels. Although the front side water walls of the first pass are also connected to the same down comer, they are deemed to be too small to have any relevant influence.

- *Hot startup:* A hot startup is the process of starting the steam generator from an already "hot" status. That means that all the pipes of the steam generator are already at an elevated temperature (much higher than the ambient temperature), which makes it possible to start the steam generator faster without causing excessive thermal stresses in the tubes. Such startups are very common procedures and were also identified as a crucial cause for the emergence of instabilities, as explained in the introduction (chapter 3).

To investigate hot startups, a new stationary status had to be created to start the startup from. First, all the heat fluxes in every heat exchanger were set to zero. For the convective evaporator bundle, this was done by setting all fouling factors to zero, since setting the gas mass flow to zero leads to numeric problems with the used software.
After sufficient simulation time, all the mass flows stopped. Note that no heat losses to the environment are considered in the model, so all the water in the steam generator now was at saturation temperature. The pressure at the outlet of the steam generator was kept constant at 75 bar, and since the steam mass flow through the superheaters dropped to zero in the new stationary status, the pressure in the steam drum now was at 75 bar as well (also see figure 28). The new target value for the liquid level in the steam drum was set to 0.3 times the inner drum diameter.
To perform a startup, all the heat fluxes were linearly increased from 0% to 100% over 10, 20 or 30 minutes. At the same time, the fouling factors of the convective evaporator bundle were reset to 1 and the gas temperature was linearly increased from 290 °C (saturation temperature) to the target temperature (according to the model parameters). The gas mass flow was also linearly increased from 1 kg/s to ~63 kg/s over the same period of time. System pressure at the outlet of the steam generator and water temperature at the outlet of the economizer were kept constant at 75 bar and 264 °C respectively. In reality, the economizer temperature would be lower at the beginning of a startup and increase over time, but taking that into account would have required an unreasonable effort and additional data about the steam generator that was not available. The influence on the results is expected to be negligible. The target value for the liquid level in the steam drum was reset to 0.5 times the inner drum diameter at the beginning of the startup.

- *Foreign objects:* Due to construction errors or insufficient pipe cleaning before the first operation, foreign objects might remain inside the convective evaporator bundle, causing higher pressure losses and blocking mass flow. To investigate this, the pressure loss coefficient at the intersection of a pipe and its vertical header on the lower part of the bundle was increased to a value of 50. Additionally, the possibility was investigated that a foreign object blocks the vertical header at its connection to the bottom horizontal header below the first hanger tube. All experiments were conducted at the 8th row of the second subsection of the convective evaporator bundle (section 9.2.8). Figure 57 illustrates the different experiment configurations.

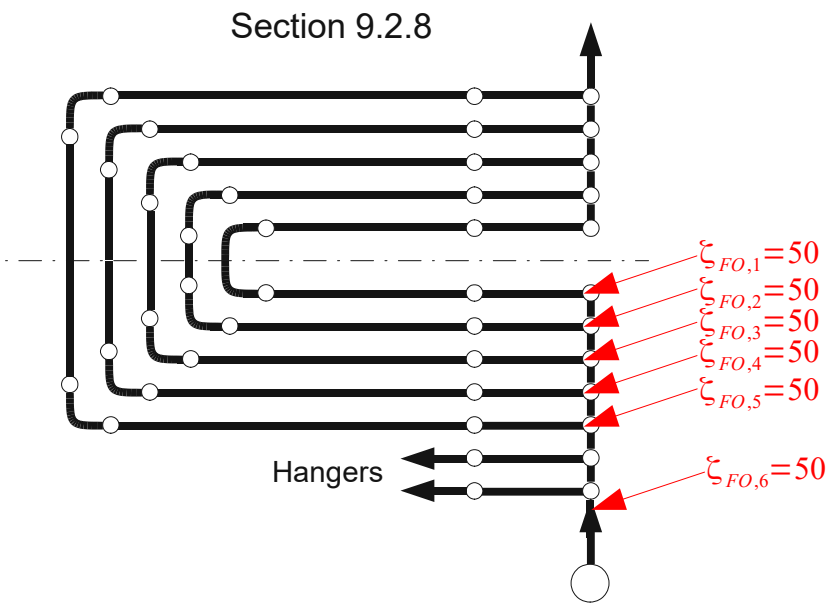

Figure 57: Experiment Configurations regarding Foreign Objects

Each experiment was conducted separately, that means a foreign object was only considered at one of the locations marked in figure 57 at a time.

All experiments were conducted as a linear increase of the respective form loss coefficient over 10 seconds, starting from a stationary state. Originally, experiments regarding foreign objects were performed as hot startups over 10 minutes, where the respective form loss coefficient was already set at the beginning of the startup. The end results were very similar and will not be presented in this work.

The following table assigns numbers to each basic experiment with short descriptions of those experiments.

exp#	Short Description
1	Section 9.1: T_G +100 °C over 5 minutes (linear increase) Sections 9.2-9.4: T_G -50 °C over 5 minutes (linear decrease)
2	Section 9.2: T_G +100 °C over 5 minutes (linear increase) Sections 9.1, 9.3, 9.4: T_G -50 °C over 5 minutes (linear decrease)
3	Section 9.3: T_G +100 °C over 5 minutes (linear increase) Sections 9.1, 9.2, 9.4: T_G -50 °C over 5 minutes (linear decrease)
4	Section 9.4: T_G +100 °C over 5 minutes (linear increase) Sections 9.1-9.3: T_G -50 °C over 5 minutes (linear decrease)
5	p_{SH} +3.75 bar over 5 minutes (linear increase)
6	p_{SH} -3.75 bar over 5 minutes (linear decrease)
7	Front water wall 1st pass (section 114): $\dot{Q}$ +20% (step)
8	Left side water wall 2nd pass (sections 31.1, 35.1, 39.1, 43.1, 47.1): $\dot{Q}$ +20% (step)
9	Right side water wall 2nd pass (sections 31.2, 35.2, 39.2, 43.2, 47.2): $\dot{Q}$ +20% (step)
10	Rear water wall 2nd pass (section 20): $\dot{Q}$ +20% (step)
11	Intermediate panels 2nd pass (section 25, 27): $\dot{Q}$ +20% (step)
12	Hot startup: 0% to 100% heating in 10 minutes (linear increase)
13	Hot startup: 0% to 100% heating in 20 minutes (linear increase)
14	Hot startup: 0% to 100% heating in 30 minutes (linear increase)
15	Section 9.2.8: Form loss coefficient between the 1st pipe and the bottom vertical header set to 50 (10 second ramp starting from stationary state)
16	Section 9.2.8: Form loss coefficient between the 2nd pipe and the bottom vertical header set to 50 (10 second ramp starting from stationary state)
17	Section 9.2.8: Form loss coefficient between the 3rd pipe and the bottom vertical header set to 50 (10 second ramp starting from stationary state)
18	Section 9.2.8: Form loss coefficient between the 4th pipe and the bottom vertical header set to 50 (10 second ramp starting from stationary state)
19	Section 9.2.8: Form loss coefficient between the 5th pipe and the bottom vertical header set to 50 (10 second ramp starting from stationary state)
20	Section 9.2.8: Form loss coefficient between the bottom vertical header and bottom horizontal header set to 50 (10 second ramp starting from stationary state)

Table 4: Experiment Numbers and Short Descriptions for Basic Experiments

Together with the permutation matrix (table 3) for the model parameters, a table of all basic experiments conducted with specific model parameters was created as follows:

exp / perm	1	2	3	4	5	6	7	8	9	10	11	12	13	14	15	16	17	18	19	20
1	✓	✓	✓	✓	✓	✓	✓	✓	✓	✓	✓	✓	✓	✓	✓	✓	✓	✓	✓	✓
2	✓	✓	✓	✓	✓	✓	✓	✓	✓	✓	✓	✖	✖	✖	✓	✓	✓	✓	✓	✓
3	✓	✓	✓	✓	✓	✓	✓	✓	✓	✓	✓	✓	✓	✓	✓	✓	✓	✓	✓	✓
4	✓	✓	✓	✓	✓	✓	✓	✓	✓	✓	✓	C1	C1	✖	✓	✓	✓	✓	✓	✓
5	✓	✓	✓	✓	✓	✓	C2	C2	C2	C2	C2	✓	✓	✓	C3	C3	C3	C3	C3	C3
6	✓	✓	✓	✓	✓	✓	C2	C2	C2	C2	C2	C1	C1	C1	C3	C3	C3	C3	C3	C3
7	✓	✓	✓	✓	✓	✓	C2	C2	C2	C2	C2	✓	✓	✓	C3	C3	C3	C3	C3	C3
8	✓	✓	✓	✓	✓	✓	C2	C2	C2	C2	C2	C1	C1	C1	C3	C3	C3	C3	C3	C3
9	✓	✓	✓	✓	✓	✓	✓	✓	✓	✓	✓	✓	✓	✓	✓	✓	✓	✓	✓	✓
10	✓	✓	✓	✓	✓	✓	C2	C2	C2	C2	C2	C1	C1	✖	✓	✓	✓	✓	✓	✓
11	✓	✓	✓	✓	✓	✓	C2	C2	C2	C2	C2	✓	✓	✓	✓	✓	✓	✓	✓	✓
12	✓	✓	✓	✓	✓	✓	✓	✓	✓	✓	✓	C1	C1	✖	✓	✓	✓	✓	✓	✓
13	✓	✓	✓	✓	✓	✓	✓	✓	✓	✓	✓	✓	✓	✓	✓	✓	✓	C4	C4	✓
14	C5	C5	C5	C5	C5	C5	C2	C2	C2	C2	C2	✓	✓	✓	✓	✓	✓	C4	C4	✓
15	C5	C5	C5	C5	C5	C5	C2	C2	C2	C2	C2	✓	✓	✓	✓	✓	✓	C4	C4	✓
16	✓	✓	✓	✓	✓	✓	✓	✓	✓	✓	✓	✖	✖	✖	✓	✓	✓	C4	C4	✓
17	C5	C5	C5	C5	C5	C5	C2	C2	C2	C2	C2	C5	C5	C5	C3	C3	C3	C4	C4	C3
18	C5	C5	C5	C5	C5	C5	C2	C2	C2	C2	C2	✓	✓	✓	C3	C3	C3	C4	C4	C3
19	C5	C5	C5	C5	C5	C5	C2	C2	C2	C2	C2	C5	C5	C5	C3	C3	C3	C4	C4	C3
20	C5	C5	C5	C5	C5	C5	C2	C2	C2	C2	C2	✖	✖	✖	C3	C3	C3	C4	C4	C3
21	✓	✓	✓	✓	✓	✓	✓	✓	✓	✓	✓	✓	✓	✓	✓	✓	✓	C4	C4	✓
22	C5	C5	C5	C5	C5	C5	C2	C2	C2	C2	C2	✓	✓	✓	✓	✓	✓	C4	C4	✓
23	C5	C5	C5	C5	C5	C5	C2	C2	C2	C2	C2	✓	✓	✓	✓	✓	✓	C4	C4	✓
24	✓	✓	✓	✓	✓	✓	✓	✓	✓	✓	✓	✖	✖	✖	✓	✓	✓	C4	C4	✓

Table 5: Combination Matrix of Permutation Numbers / Experiment Numbers for Basic Experiments

✓	Stable system
✖	Experiment caused instabilities. Detailed information in following chapters.
C*	Experiment canceled. The number denotes the cause for cancellation in table 6.

canc#	Cause for cancellation
C1	Hot startups without separated feeding / rising systems caused heavy oscillations (chapter 8.2.4). Most hot startups with that configuration were therefore canceled.
C2	Perturbations in the residual heat exchangers barely have any effect on the convective evaporator bundle (chapter 8.2.3). Therefore, those experiments were canceled.
C3	Lower temperatures do not seem to have a remarkable effect on experiments with foreign objects (chapter 8.2.5). Experiments at medium temperatures were therefore canceled.
C4	New bundle geometry only has 3 tubes per vertical row. Experiments 18 and 19, investigating foreign objects in tubes 4 and 5 of section 9.2.8, are therefore not possible.
C5	Experiments with the new bundle geometry show fairly similar results and the most significant effects were already found with the old bundle geometry. Therefore, many of the experiments with the new bundle geometry were canceled.

Table 6: Cancellation Numbers and Causes for Basic Experiments

8.1.2 Experiments regarding local circulation

The vertical headers of the convective evaporator bundle could theoretically function as a water/steam separator. This could lead to circulation within a vertical row of the convective evaporator bundle, as illustrated in figure 58.

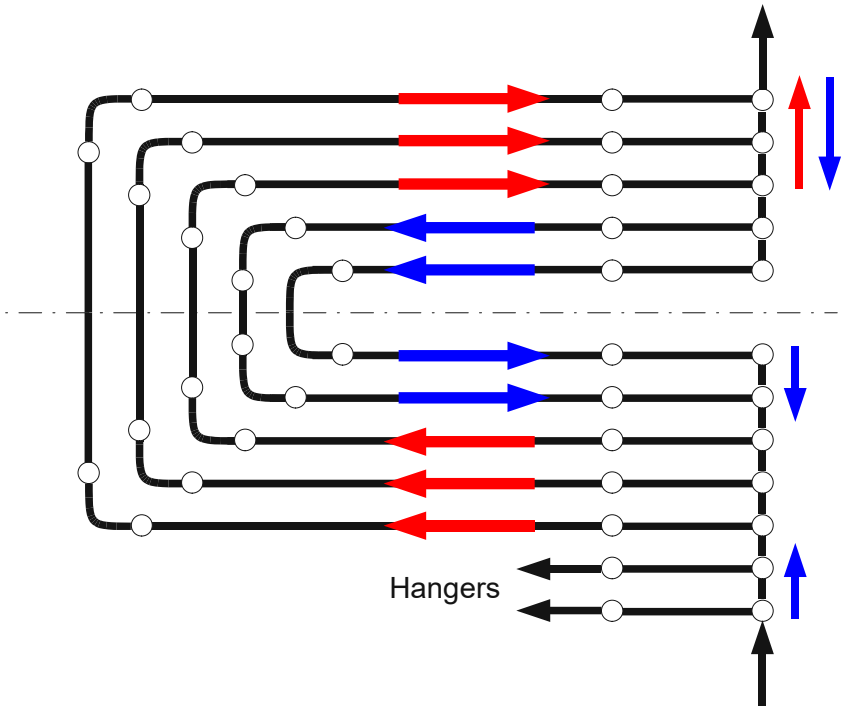

Figure 58: Possible local Circulation within a vertical Row

Blue arrows represent mass flows of subcooled or saturated liquid and red arrows mass flows of water/steam mixtures. An operation like this is most likely when some tubes are not heated as well as others. To investigate this possibility, experiments were conducted where the fouling factors of the outermost or innermost pipes of a single vertical row of the convective evaporator bundle were set to 0, as illustrated in figure 59. Setting the fouling factors to 0 makes those parts unheated.

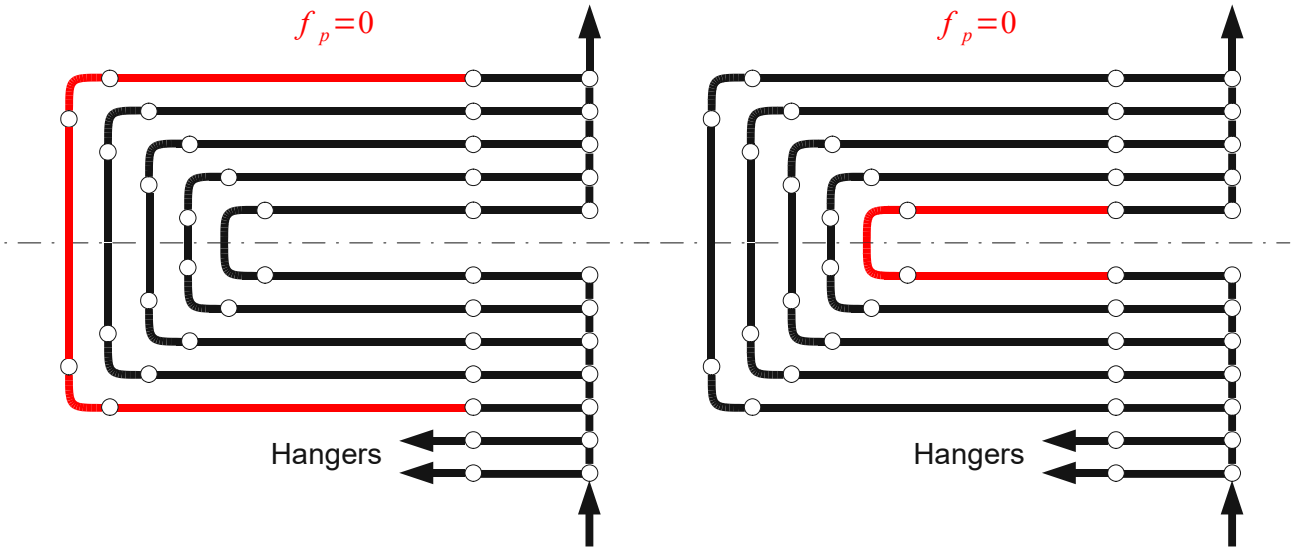

Figure 59: Illustration of Experiment Conditions to investigate local Circulations

Similar to circulations within a single vertical row, circulations between vertical rows are also imaginable when some of these rows are less heated than others. Figure 60 shows a possible flow pattern of such an operation when one subsection of the convective evaporator bundle is unheated.

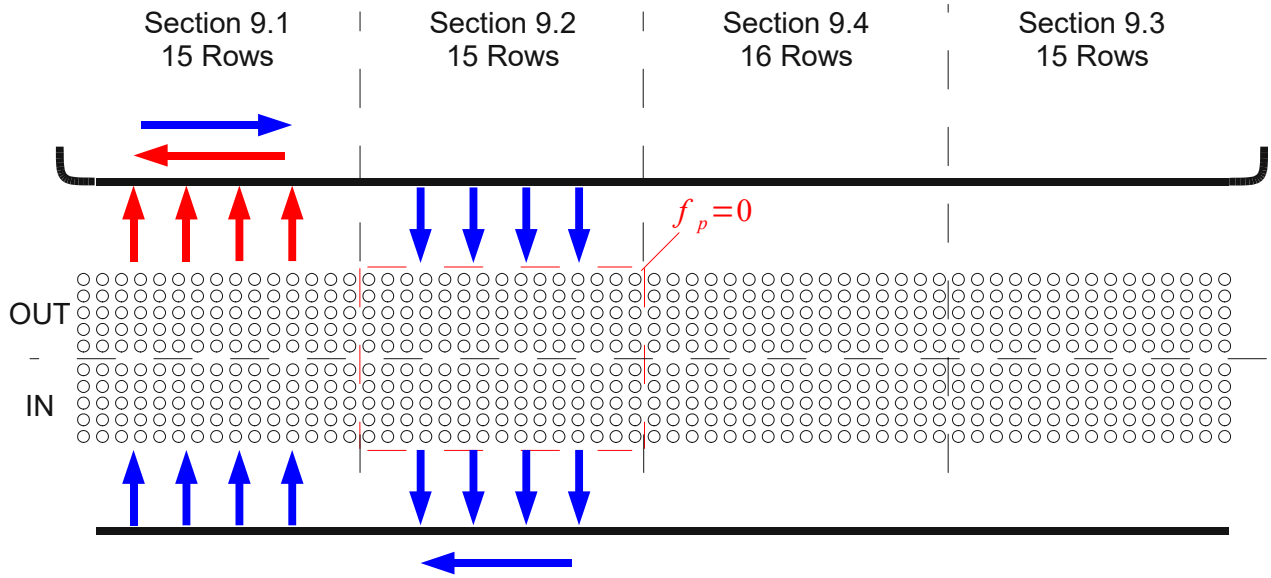

Figure 60: Illustration of possible Flow Patterns between vertical Rows

Experiments were conducted where the fouling factors of subsections of the convective evaporator bundle were set to 0. The setting of fouling factors, both at a whole subsection and at single tubes within a row, was done linearly over 10 seconds from a stationary status. Although not very realistic, it is expected to enhance any possible effect.

Table 7 summarizes the experiments regarding local circulation. The assigned experiment

numbers are continued from table 4. “Section 9.n.8” describes the 8th vertical row in the nth subsection of the convective evaporator bundle, which is in the middle of the respective subsection.

exp#	Short Description
21	Section 9.1: Fouling factors of all pipes set to 0 (ramp over 10 seconds)
22	Section 9.2: Fouling factors of all pipes set to 0 (ramp over 10 seconds)
23	Section 9.3: Fouling factors of all pipes set to 0 (ramp over 10 seconds)
24	Section 9.4: Fouling factors of all pipes set to 0 (ramp over 10 seconds)
25	Section 9.1.8: Fouling factor of the 1st pipe set to 0 (ramp over 10 seconds)
26	Section 9.2.8: Fouling factor of the 1st pipe set to 0 (ramp over 10 seconds)
27	Section 9.3.8: Fouling factor of the 1st pipe set to 0 (ramp over 10 seconds)
28	Section 9.4.8: Fouling factor of the 1st pipe set to 0 (ramp over 10 seconds)
29	Section 9.1.8: Fouling factor of the 5th pipe set to 0 (ramp over 10 seconds)
30	Section 9.2.8: Fouling factor of the 5th pipe set to 0 (ramp over 10 seconds)
31	Section 9.3.8: Fouling factor of the 5th pipe set to 0 (ramp over 10 seconds)
32	Section 9.4.8: Fouling factor of the 5th pipe set to 0 (ramp over 10 seconds)

Table 7: Experiment Numbers and Short Descriptions for Experiments regarding local Circulation

Table 8 shows the combination of experiment numbers with permutation numbers similar to table 5.

exp / perm	21	22	23	24	25	26	27	28	29	30	31	32
1	✓	✓	✓	✓	✓	✓	✓	✓	✓	✓	✓	✓
2	✓	✓	✓	✓	✓	✓	✓	✓	✓	✓	✓	✓
3	✓	✓	✓	✓	✓	✓	✓	✓	✓	✓	✓	✓
4	✓	✓	✓	✓	✓	✓	✓	✓	✓	✓	✓	✓
5	C1	C1	C1	C1	C1	C1	C1	C1	C1	C1	C1	C1
6	C1	C1	C1	C1	C1	C1	C1	C1	C1	C1	C1	C1
7	C1	C1	C1	C1	C1	C1	C1	C1	C1	C1	C1	C1
8	C1	C1	C1	C1	C1	C1	C1	C1	C1	C1	C1	C1
9	✓	✓	✓	✓	✓	✓	✓	✓	✓	✓	✓	✓
10	✓	✓	✓	✓	✓	✓	✓	✓	✓	✓	✓	✓
11	✓	✓	✓	✓	✓	✓	✓	✓	✓	✓	✓	✓
12	✓	✓	✓	✓	✓	✓	✓	✓	✓	✓	✓	✓
13	✓	✓	✓	✓	✓	✓	✓	✓	✓	✓	✓	✓
14	✓	✓	✓	✓	✓	✓	✓	✓	✓	✓	✓	✓
15	✓	✓	✓	✓	✓	✓	✓	✓	✓	✓	✓	✓
16	✓	✓	✓	✓	✓	✓	✓	✓	✓	✓	✓	✓
17	C1	C1	C1	C1	C1	C1	C1	C1	C1	C1	C1	C1
18	C1	C1	C1	C1	C1	C1	C1	C1	C1	C1	C1	C1
19	C1	C1	C1	C1	C1	C1	C1	C1	C1	C1	C1	C1
20	C1	C1	C1	C1	C1	C1	C1	C1	C1	C1	C1	C1
21	✓	✓	✓	✓	✓	✓	✓	✓	✓	✓	✓	✓
22	✓	✓	✓	✓	✓	✓	✓	✓	✓	✓	✓	✓
23	✓	✓	✓	✓	✓	✓	✓	✓	✓	✓	✓	✓
24	✓	✓	✓	✓	✓	✓	✓	✓	✓	✓	✓	✓

Table 8: Combination Matrix of Permutation Numbers / Experiment Numbers for Experiments regarding local Circulation

✓	Stable system
✖	Experiment caused instabilities. Detailed information in following chapters.
C*	Experiment canceled. The number denotes the cause for cancellation in table 9.

canc#	Cause for cancellation
C1	Lower temperatures do not seem to have a remarkable effect on experiments regarding local circulation (chapters 8.2.6 and 8.2.7). Experiments at medium temperatures were therefore canceled.

Table 9: Cancellation Numbers and Causes for Experiments regarding local Circulation

8.1.3 Special and Requested Experiments

Some additional experiments were requested by CNIM or were added to investigate the influence of a special configuration:

- *Extra-long startups:* There was some concern that the startup times were too short to yield any results achievable in practice. Therefore, additional hot startup experiments with startup times of 2 hours were conducted. All other configurations stayed the same as with the other hot startup experiments.
- *Extra-long startups with uneven heating and imperfect blind plates:* To further investigate the influence of imperfect blind plates on hot startups, while simultaneously making sure that the startup time is not too small (as mentioned before), hot startup experiments over 2 hours with a severe disparity in heat flux between the left and right side were conducted, as illustrated in figure 61.

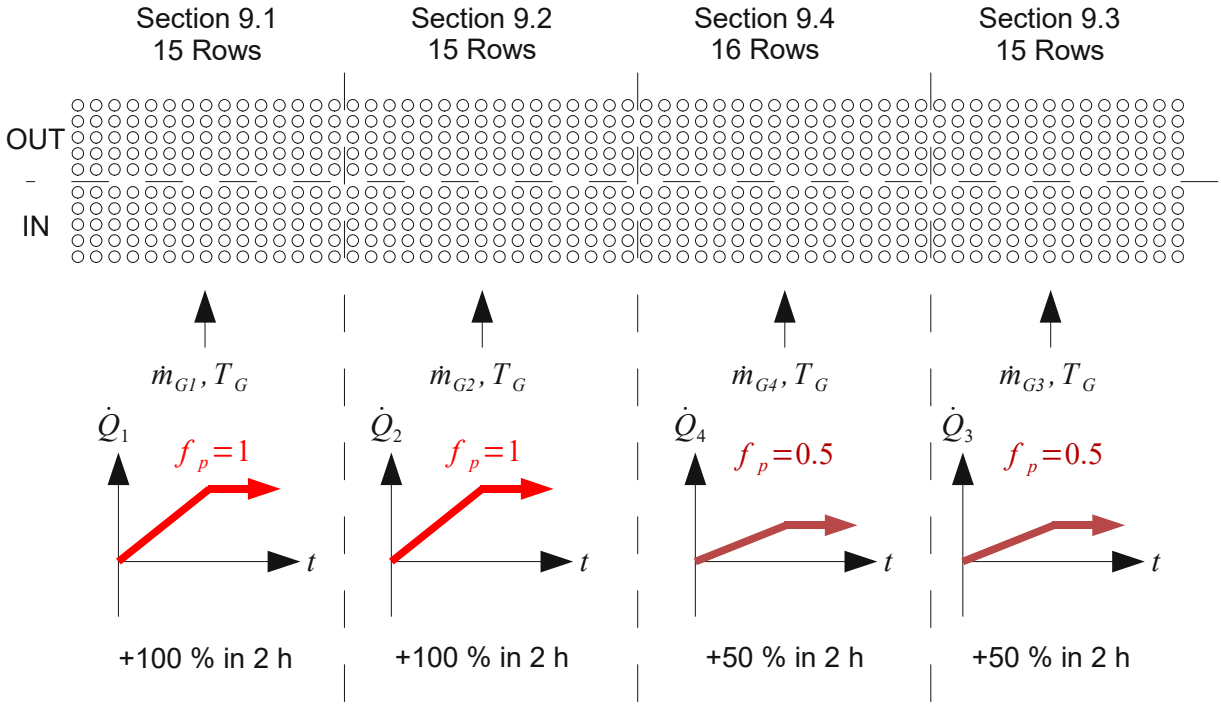

Figure 61: Experiment Configuration for Extra-Long Startups with Uneven Heating and Imperfect Blind Plates

The disparity was chosen to be 50 % of the nominal heat flux. Inlet gas temperatures were kept the same for all subsections of the bundle, but the fouling factors of the pipes on one side were set to half the value, resulting in about half the heat flux. Experiments were conducted with lower heat fluxes in either the left or the right side.

Table 10 sums up the experiment configurations and assigns experiment numbers to them.

exp#	Short Description
33	Hot startup: 0% to 100% heating in 2 hours (linear increase)
34	Hot startup: 0% to 100% heating on left side (sections 9.1, 9.2), 0% to 50% heating on right side (sections 9.3, 9.4), both in 2 hours (linear increases)
35	Hot startup: 0% to 50% heating on left side (sections 9.1, 9.2), 0% to 100% heating on right side (sections 9.3, 9.4), both in 2 hours (linear increases)

Table 10: Experiment Numbers and Short Descriptions for Special and Requested Experiments

Table 11 shows the combination of experiment numbers with permutation numbers:

exp / perm	33	34	35
1	C1	C2	C2
2	✖	C2	C2
3	C1	✓	✓
4	✖	✖	✖
5	C1	C2	C2
6	C1	C2	C2
7	C1	C3	C3
8	C1	C3	C3
9	C1	C2	C2
10	✖	C2	C2
11	C1	✓	✓
12	✖	✖	✖
13	C1	C2	C2
14	✓	C2	C2
15	C1	✓	✓
16	✖	✖	✖
17	C1	C2	C2
18	C1	C2	C2
19	C1	C3	C3
20	C1	C3	C3
21	C1	C2	C2
22	✓	C2	C2
23	C1	✓	✓
24	✖	✖	✖

Table 11: Combination Matrix of Permutation Numbers / Experiment Numbers for Special and Requested Experiments

✓	Stable system
✖	Experiment caused instabilities. Detailed information in following chapters.
C*	Experiment canceled. The number denotes the cause for cancellation in table 12.

canc#	Cause for cancellation
C1	Extra-long startups were only performed for those model parameter configurations that also showed instabilities during startups over 30 minutes. Assuming that parameter configurations that did not show any instabilities for shorter startup times would stay stable at longer startup times as well, experiments with these configurations were canceled.
C2	Hot startups with uneven heating were primarily performed to investigate the influence of imperfect blind plates. Experiments with model configurations that include perfect blind plates were therefore canceled.
C3	As already shown with the basic experiments, lower gas temperatures at the inlet of the convective evaporator bundle do not appear to have an impact on the instabilities observed during hot startups. Therefore, experiments at medium temperatures were canceled.

Table 12: Cancellation Numbers and Causes for Special and Requested Experiments

8.2 Experiment Results

8.2.1 Partial Hot Stream of Flue Gas

These experiments did not lead to an unstable system, as table 5 shows. However, the results show the general behavior of the system for different loads and system configurations. Figures 62 to 65 show the combined mass flows of separate subsections of the convective evaporator bundle for different system configurations.

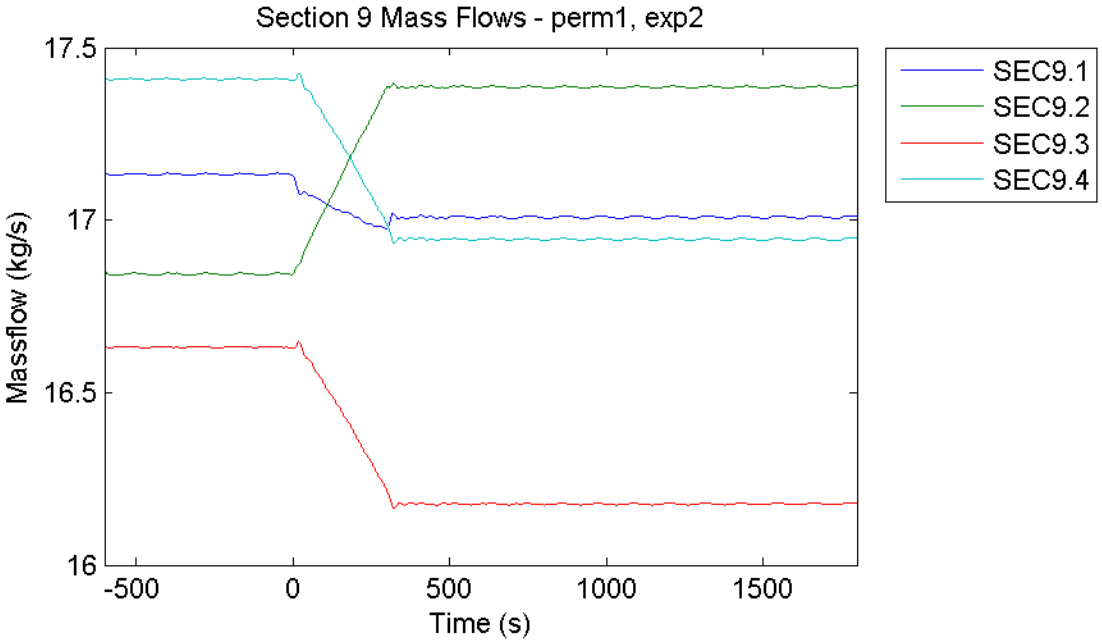

Figure 62: Mass Flows of Bundle Subsections – Perfect Blind Plates, Separated Feeding / Rising System, Initial Inlet Gas Temperature 710 °C, Partial Hot Stream of Flue Gas at Section 9.2

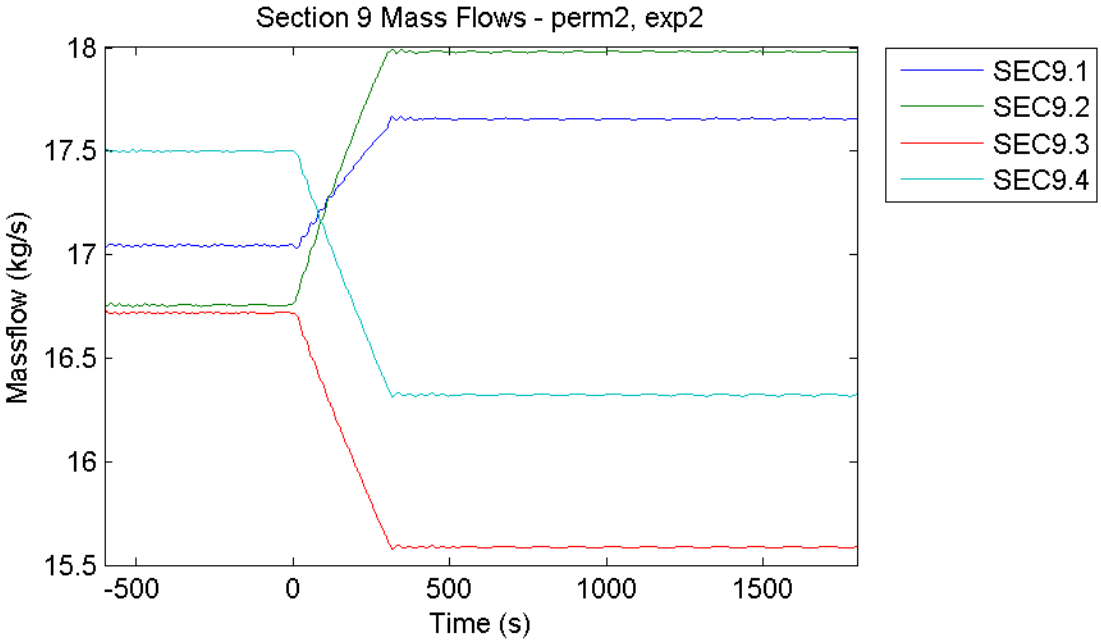

Figure 63: Mass Flows of Bundle Subsections – Perfect Blind Plates, Not Separated Feeding / Rising System, Initial Inlet Gas Temperature 710 °C, Partial Hot Stream of Flue Gas at Section 9.2

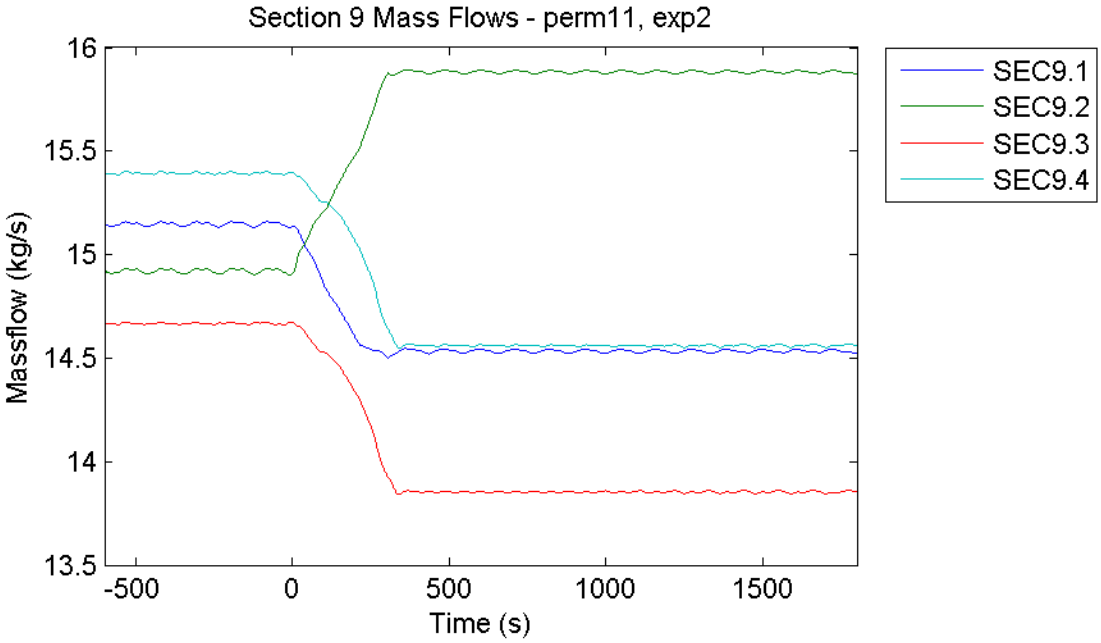

Figure 64: Mass Flows of Bundle Subsections – Imperfect Blind Plates, Separated Feeding / Rising System, Initial Inlet Gas Temperature 550 °C, Partial Hot Stream of Flue Gas at Section 9.2

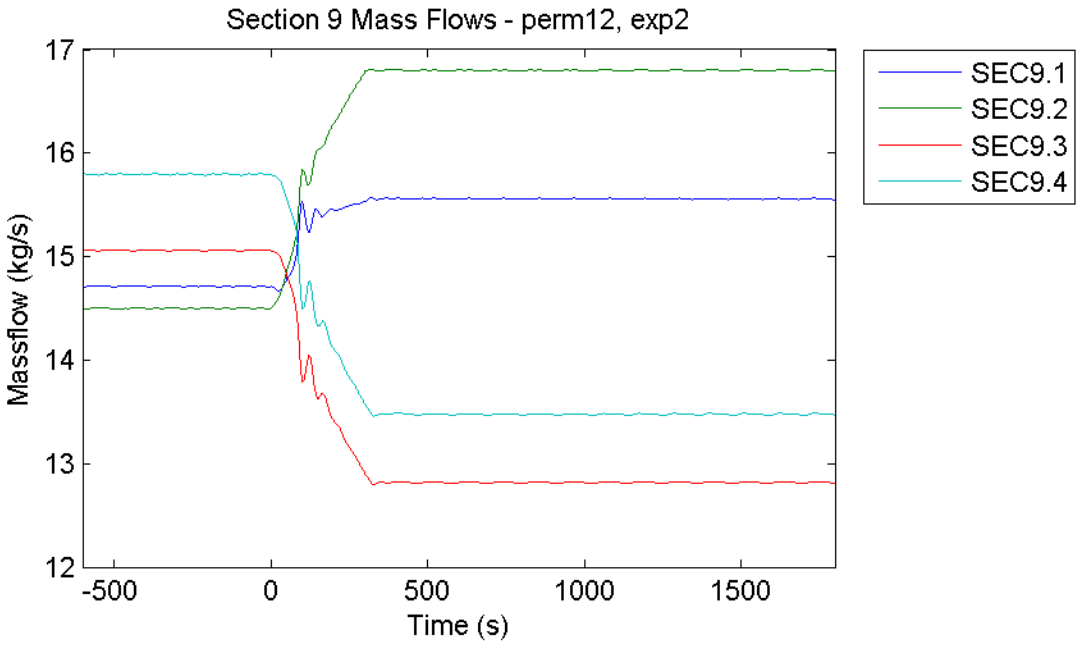

Figure 65: Mass Flows of Bundle Subsections – Imperfect Blind Plates, Not Separated Feeding / Rising System, Initial Inlet Gas Temperature 550 °C, Partial Hot Stream of Flue Gas at Section 9.2

All figures show the results from experiment number 2, which increased the gas temperature at the inlet of subsection 9.2 by 100°C while decreasing the inlet gas temperatures at all other subsections by 50 °C (see chapter 8.1.1). An increased gas temperature (and therefore heat flux) at subsection 9.2 always leads to an increased mass flow in the same subsection, as to be expected. Similarly, the mass flows decrease due to decreased gas temperatures at subsections 9.3 and 9.4. Subsection 9.1, which is on the same side as subsection 9.2, behaves differently for different system configurations: for separated feeding and rising systems (figures 62 and 64) the mass flow tends to decrease slightly, while for not separated feeding and rising systems (figures 63 and 65) the mass flow increases, even though the subsections inlet gas temperature is decreasing. This has to be accompanied by an increased mass flow from the right to the left side, as the following figures show.

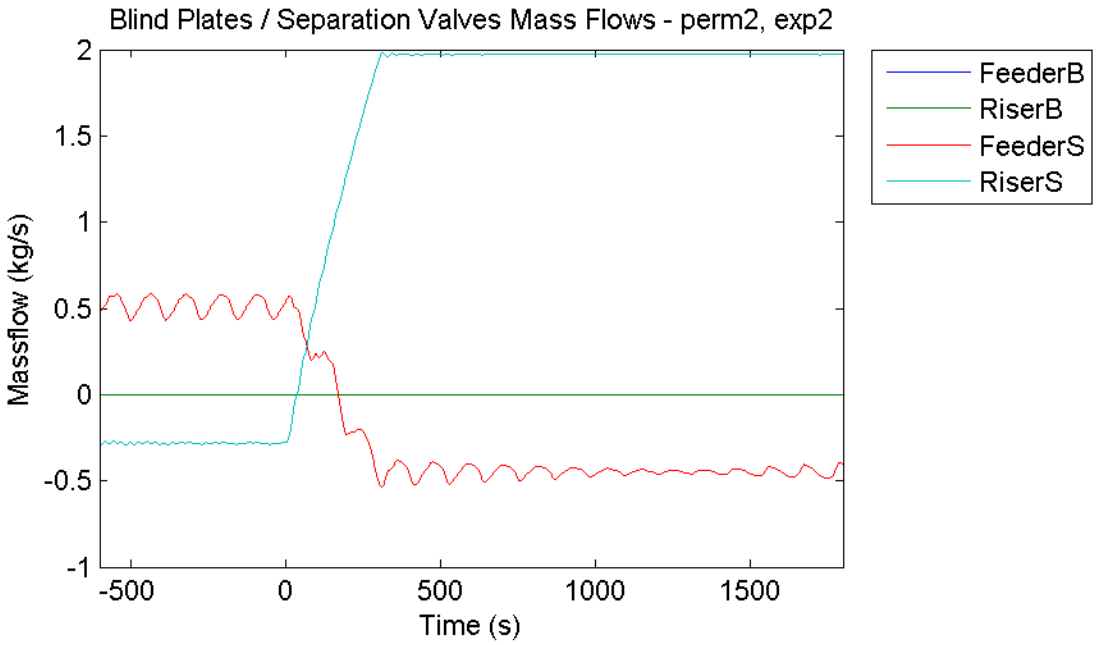

Figure 66: Mass Flows between Sides – Perfect Blind Plates, Not Separated Feeding / Rising System, Initial Inlet Gas Temperature 710 °C, Partial Hot Stream of Flue Gas at Section 9.2

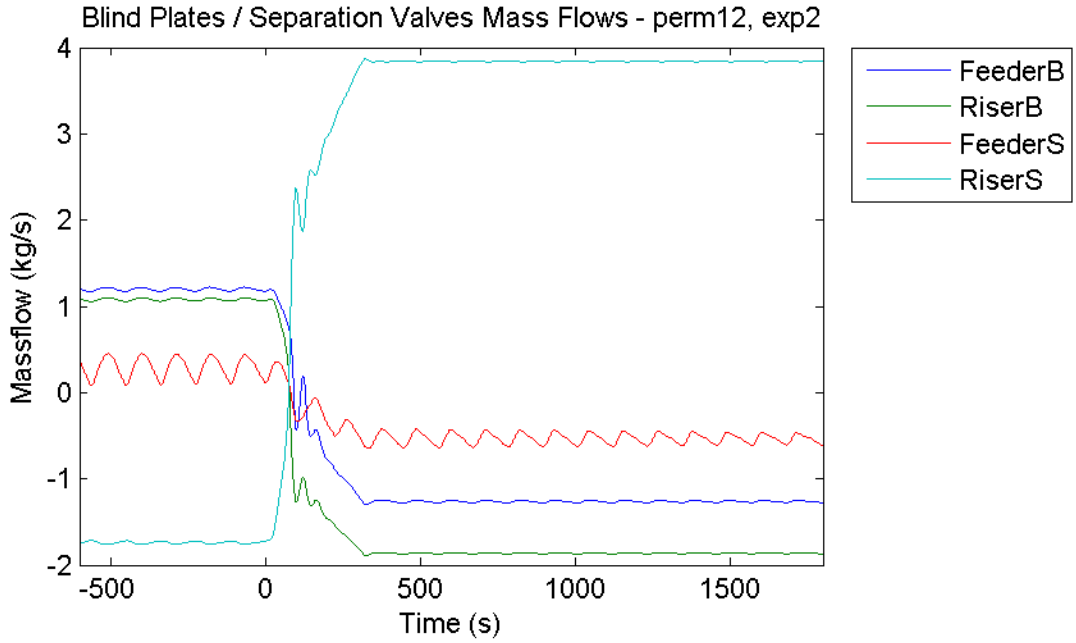

Figure 67: Mass Flows between Sides – Imperfect Blind Plates, Not Separated Feeding / Rising System, Initial Inlet Gas Temperature 550 °C, Partial Hot Stream of Flue Gas at Section 9.2

Positive mass flows denote mass flows from the left to the right side. “FeederB” and “RiserB” are the mass flows between the bottom / top blind plates and “FeederS” and RiserS” are the ones at the bottom / top points of separation of the feeding / rising system (see figure 34 on page 53). One can see that the mass flows between the feeding headers change direction and provide a higher mass flow for the left side. The mass flow at the top separation point also changes direction due to

the now higher steam production on the left side, which causes a higher pressure on the left side of the top riser than on the right side and “pushes” the fluid to the right side. This can also be observed from the mass flows and static pressure losses of section 12:

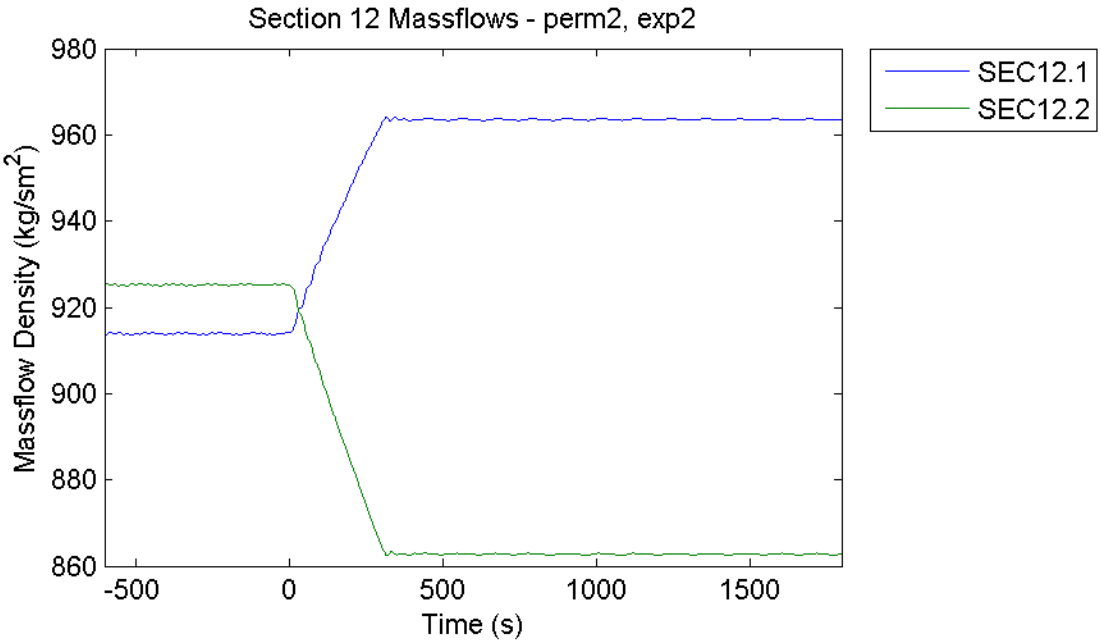

Figure 68: Mass Flows of Main Risers – Perfect Blind Plates, Not Separated Feeding / Rising System, Initial Inlet Gas Temperature 710 °C, Partial Hot Stream of Flue Gas at Section 9.2

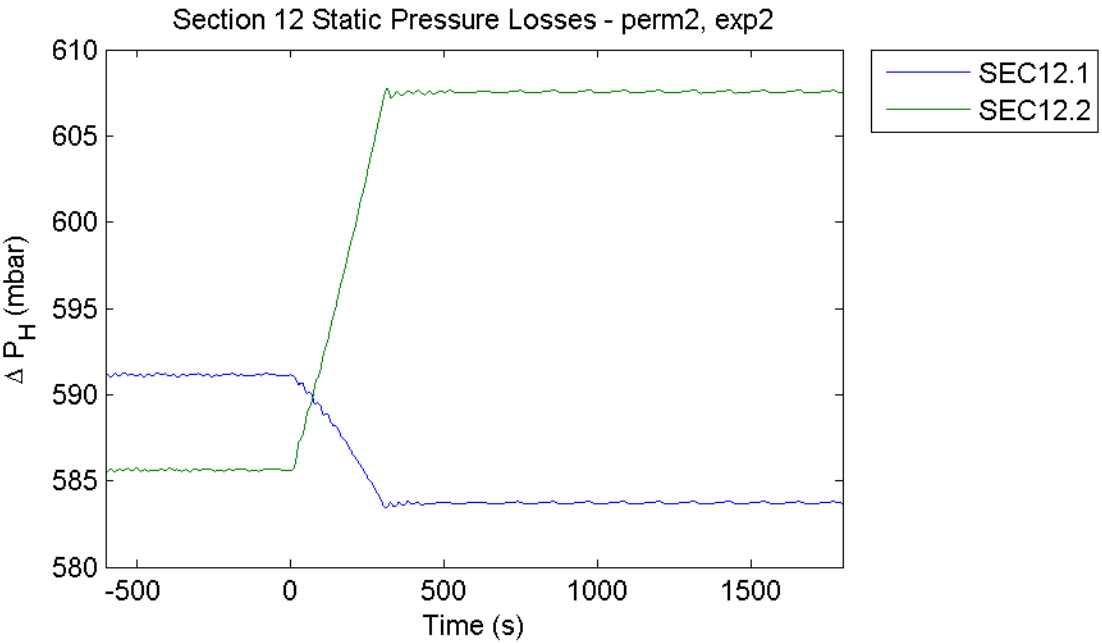

Figure 69: Static Pressure Losses of Main Risers – Perfect Blind Plates, Not Separated Feeding / Rising System, Initial Inlet Gas Temperature 710 °C

Section 12.1 and 12.2 are the left and right side main risers connecting the two horizontal headers

of the rising system for the convective evaporator bundle. As explained before, the left side mass flow increases while the right side mass flow decreases. At the same time the static pressure difference in the left riser decreases while it increases in the right riser, which can only be explained by a decreased / increased fluid density due to an increased / decreased mass fraction of steam at the respective side.

Other measurements do not show any significant results. In general, mass flows of left side feeders (sections 1.1, 200.1 and 6.1-6.5) increase while decreasing on the right side, which is not surprising. Experiments where the inlet gas temperatures at other subsections were increased (experiments 1, 3 and 4) show very similar results. Lower gas temperatures do not seem to have any major effect other than generally lower heat fluxes and mass flows.

8.2.2 Drum Pressure Variations

Drum pressure variations did not lead to instabilities per se, but they certainly had an effect on stability, as this chapter will show. As the variations were set as linear increases or decreases of the pressure of superheated steam at the outlet of the steam generator (as explained in chapter 8.1.1), the actual drum pressure showed a slightly different course, as shown in the following figure.

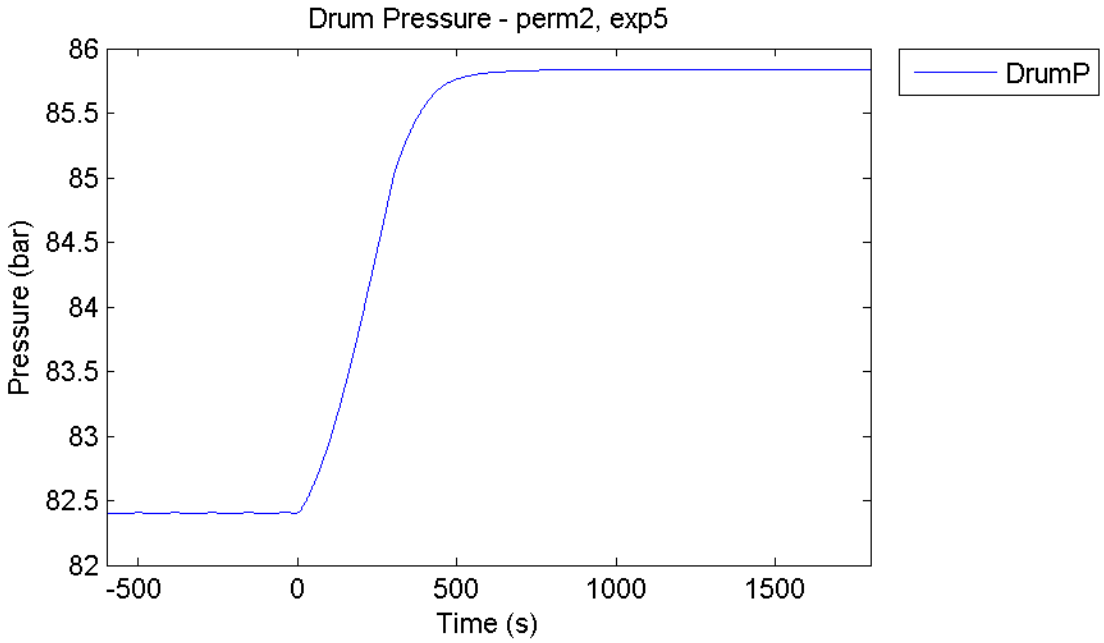

Figure 70: Drum Pressure – Perfect Blind Plates, Not Separated Feeding / Rising System, Inlet Gas Temperature 710 °C, Pressure Increase Experiment

Figure 70 shows the case of a linearly increased pressure of superheated steam (experiment 5). A decrease (experiment 6) looks practically the same but mirrored vertically. The increase in drum pressure is not quite linear, and it continues to rise for some time after the pressure increase stopped at 300 seconds. This is caused by a delayed onset of boiling: the saturation temperature rises due to the increased pressure in the steam generator. This requires all the fluid and pipe walls to be heated up to the higher saturation temperature to start evaporation again, meaning that part of the heat flux into the steam generator has to be spent on heating the system (sensible heat) rather than evaporation (latent heat). Once the pressure increase has stopped, the entire heat flux can be spent on evaporation again, which causes a higher steam production, which in turn increases the drum pressure again. That counteracts the steam production by increasing the saturation temperature. This explains the smooth transition to a constant drum pressure between 300 and about 700 seconds. The total difference in drum pressure between the two constant values before and after the pressure variation is about 3.4 bar, and is about the same in the case of an increase and a decrease, and for other gas temperatures at the inlet of the convective

evaporator bundle.

In general, pressure decreases seem to have an enhancing effect on mass flow oscillations in the whole system. The following figures show this for the convective evaporator bundle at different gas temperatures.

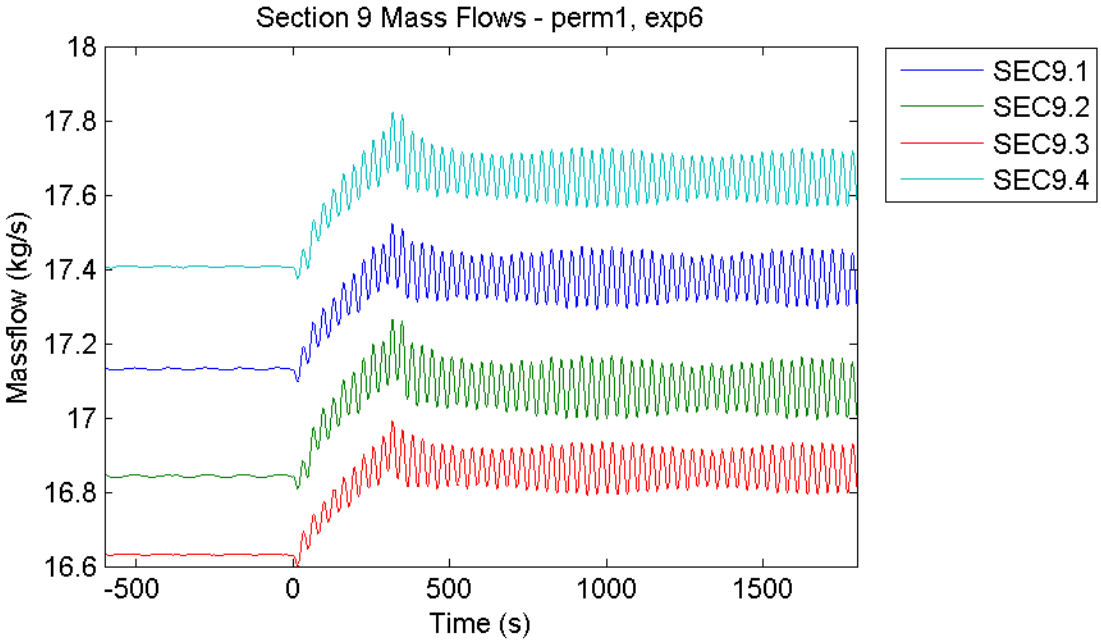

Figure 71: Mass Flows of Bundle Subsections – Perfect Blind Plates, Separated Feeding / Rising System, Inlet Gas Temperature 710 °C, Pressure Decrease Experiment

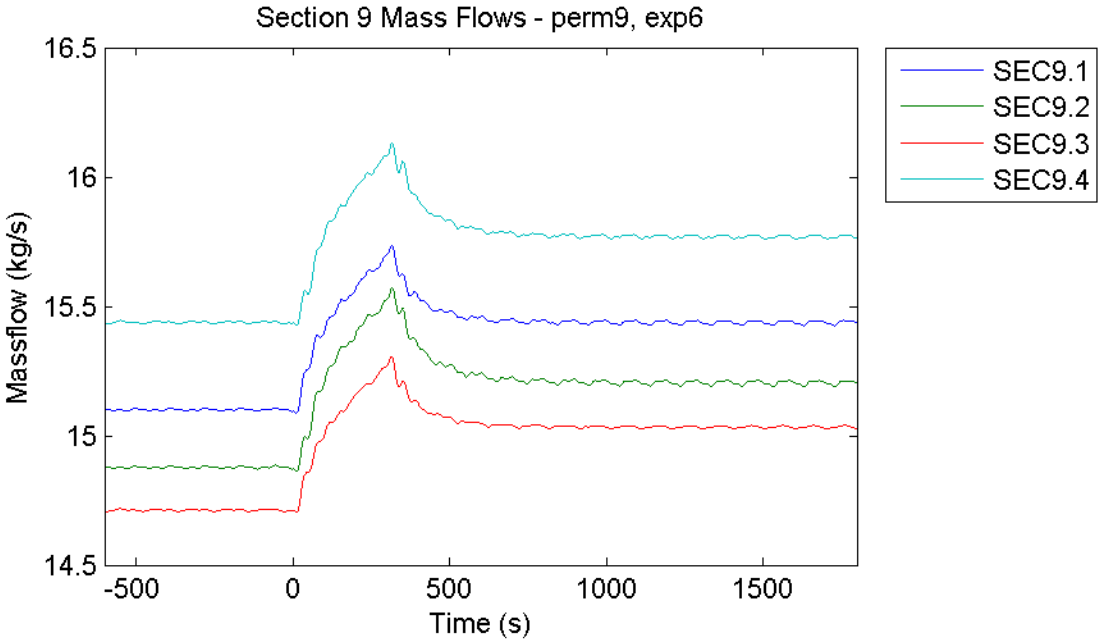

Figure 72: Mass Flows of Bundle Subsections – Perfect Blind Plates, Separated Feeding / Rising System, Inlet Gas Temperature 550 °C, Pressure Decrease Experiment

Besides the gas temperature, the model configuration for both graphs is the same. Other configurations (blind plates, etc.) do not have any effect on the results. One can see that the enhancement of oscillations is much larger at higher gas temperatures compared to lower ones. The oscillations are global and occur at the same time in all pipes of the bundle, meaning that the oscillations did not cause any local circulations.

Pressure increases seem to have the opposite effect: they rather reduce amplitudes of existing oscillations in the system. Specifically, they can almost annihilate the oscillations caused by the front side water wall of the first pass, which also causes the oscillations in the main down comers, as figure 73 shows.

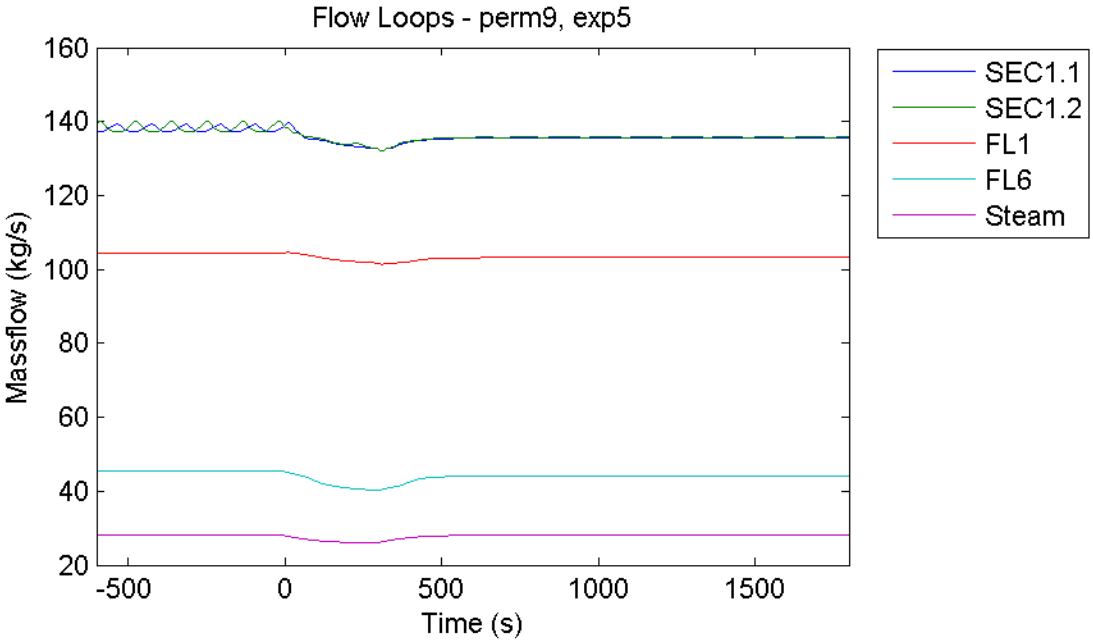

Figure 73: Mass Flows of Flow Loops – Perfect Blind Plates, Separated Feeding / Rising System, Inlet Gas Temperature 550 °C, Pressure Increase Experiment

This stabilizing effect is independent of model configuration and works for all oscillations in the entire system, although it is not as recognizable in most of the other parts. It can be observed fairly well at the blind plates and separation points of the main feeding and rising system, figure 74.

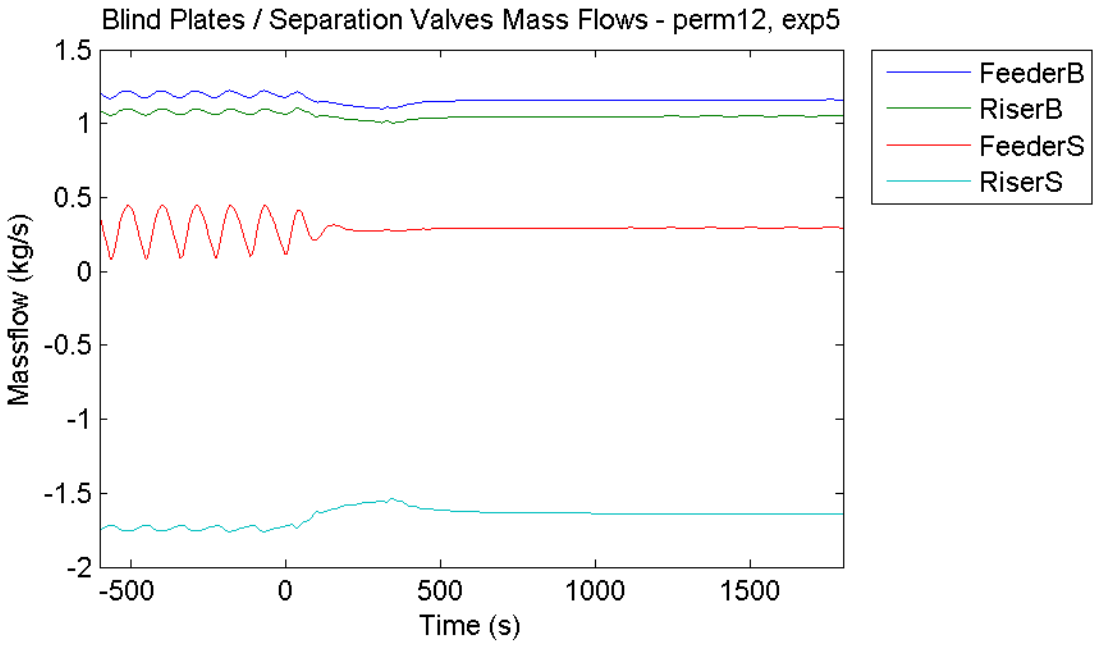

Figure 74: Mass Flows between Sides – Imperfect Blind Plates, Not Separated Feeding / Rising System, Inlet Gas Temperature 550 °C, Pressure Increase Experiment

All oscillations between the left and right side of the main feeding and rising system at the blind plates and points of separation are almost entirely stopped by the pressure increase in the system.

8.2.3 Sudden Change of Heat Flux in Residual Heat Exchangers

These experiments had very little effect on the evaporator, which is why many of them were not even conducted, as table 5 shows. This chapter demonstrates some of the results to justify the decision to largely cancel these experiments.

Every increase of heat flux at one of the residual heat exchangers also leads to a higher steam production, which increases the drum pressure. Because of that, these experiments are somewhat comparable to the previous ones directly increasing the pressure in the drum. As an example, figure 75 shows the course of drum pressure for a sudden increase in heat flux by 20 % at the front water wall of the first pass (experiment number 7).

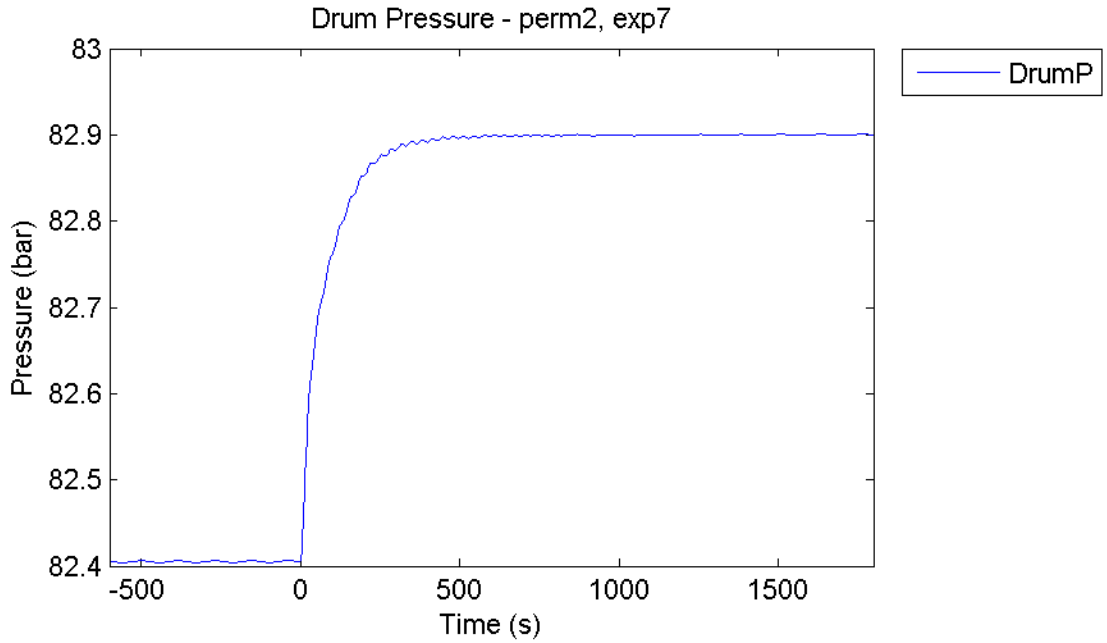

Figure 75: Drum Pressure – Perfect Blind Plates, Not Separated Feeding / Rising System, Inlet Gas Temperature 710 °C, Heat Flux Increase at Front Water Wall 1st Pass by 20 %

When comparing figure 75 to figure 70, one can see that the drum pressure increase is steeper in figure 75, but otherwise both graphs are quite similar. This is caused by the *sudden* increase (as a step function) of heat flux at the front side water wall of the first pass compared to the *linear* increase (as a ramp function over 5 minutes) of steam pressure for the other experiment.

However, the total pressure difference is only about 0.5 bar compared to 3.4 bar. Heat flux increases at other residual heat exchangers (experiments number 8-11) or at lower gas temperatures at the inlet of the convective evaporator bundle yield even lower total drum pressure increases. This is most liekly the reason why these experiments barely affected the convective evaporator bundle, as the following figures show.

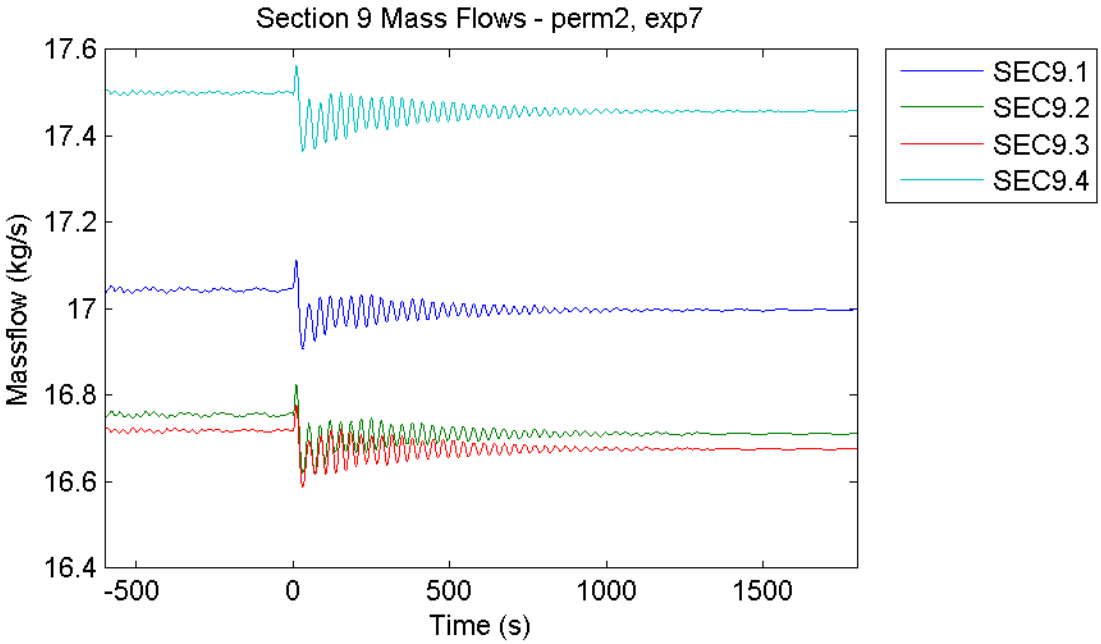

Figure 76: Mass Flows of Bundle Subsections – Perfect Blind Plates, Not Separated Feeding / Rising System, Inlet Gas Temperature 710 °C, Heat Flux Increase at Front Water Wall 1st Pass by 20 %

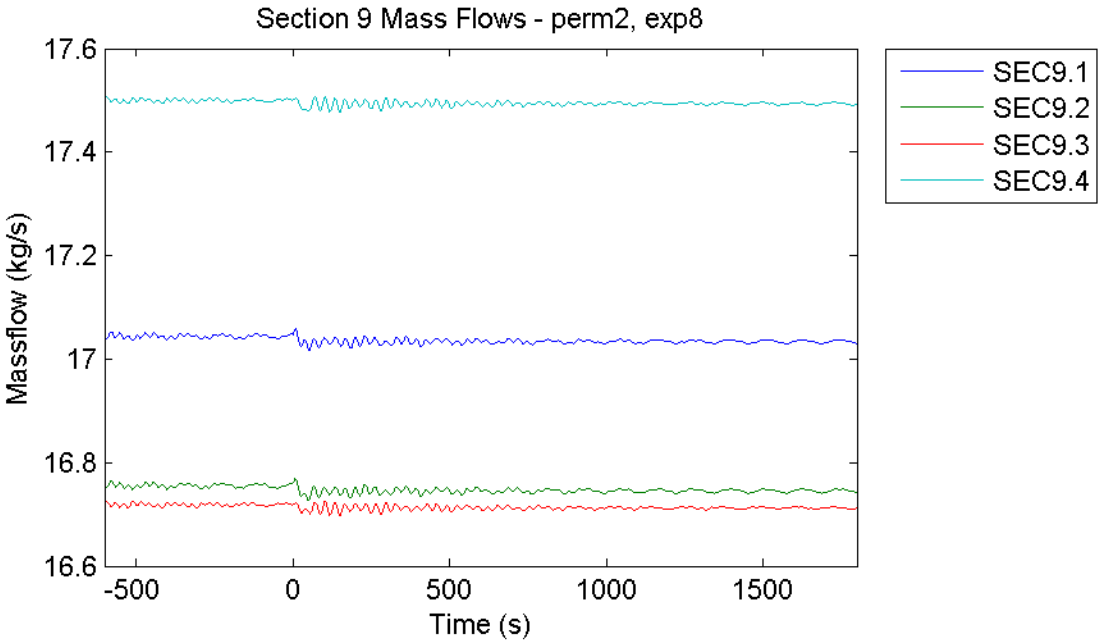

Figure 77: Mass Flows of Bundle Subsections – Perfect Blind Plates, Not Separated Feeding / Rising System, Inlet Gas Temperature 710 °C, Heat Flux Increase at Left Side Water Wall 2nd Pass by 20 %

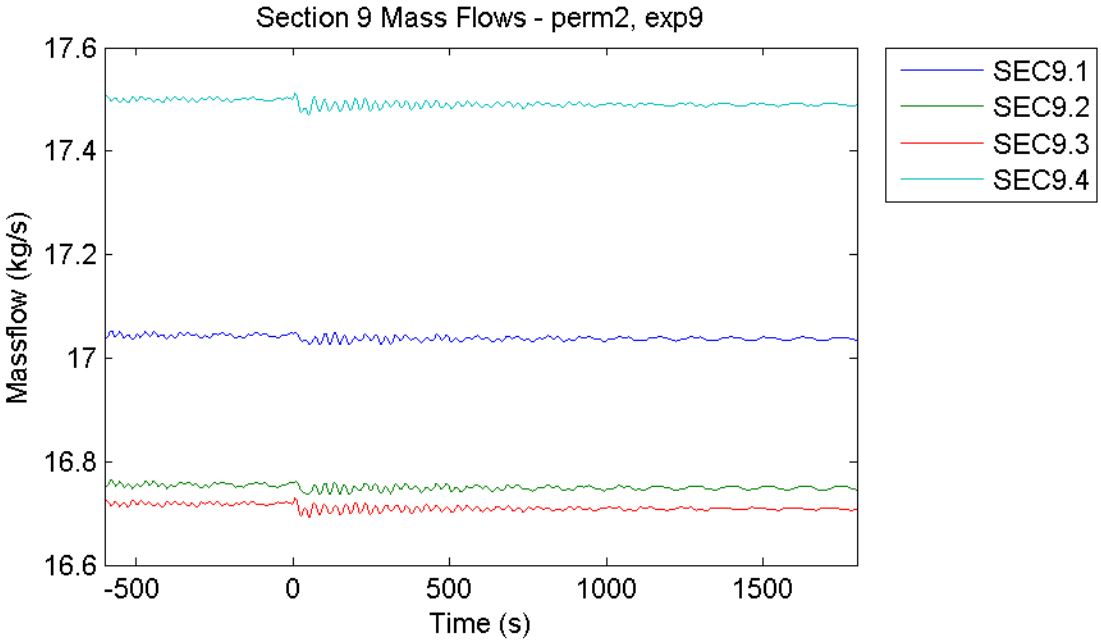

Figure 78: Mass Flows of Bundle Subsections – Perfect Blind Plates, Not Separated Feeding / Rising System, Inlet Gas Temperature 710 °C, Heat Flux Increase at Right Side Water Wall 2nd Pass by 20 %

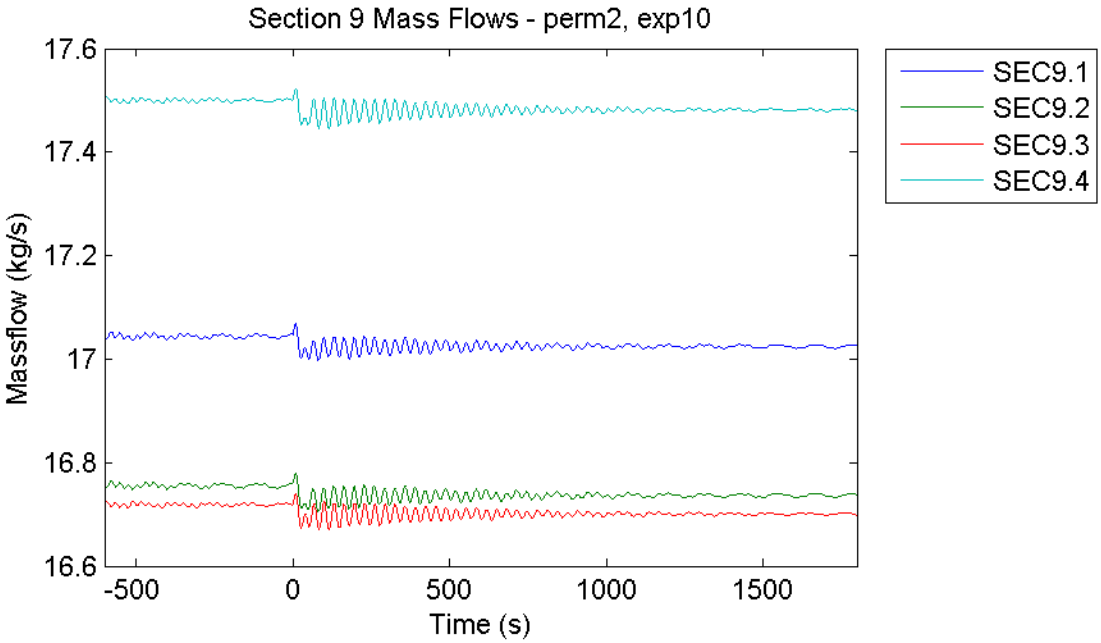

Figure 79: Mass Flows of Bundle Subsections – Perfect Blind Plates, Not Separated Feeding / Rising System, Inlet Gas Temperature 710 °C, Heat Flux Increase at Rear Water Wall 2nd Pass by 20 %

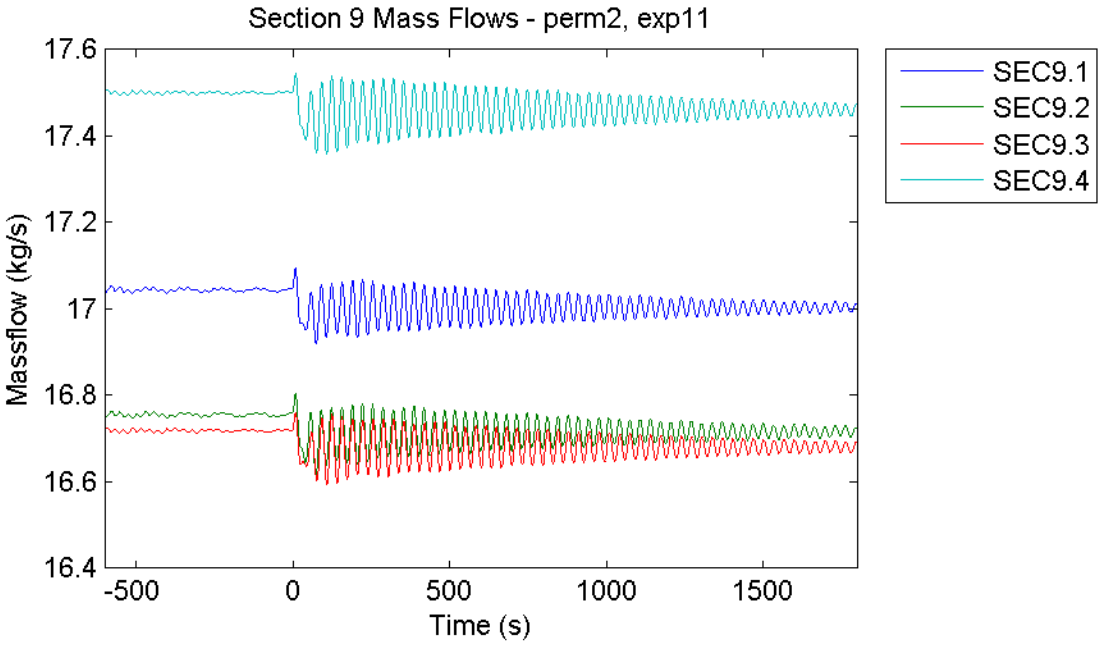

Figure 80: Mass Flows of Bundle Subsections – Perfect Blind Plates, Not Separated Feeding / Rising System, Inlet Gas Temperature 710 °C, Heat Flux Increase at Intermediate Panels 2nd Pass by 20 %

One can see that the sudden increase of heat flux in one of the residual heat exchangers causes some initial oscillations which all fade away after some time. Even the biggest amplitudes only reach about 0.1 kg/s, which is not even 1 % of the mass flow through one bundle subsection. The influence is barely recognizable when increasing the heat flux of the left or right side water wall of the second pass, experiment numbers 8 and 9 (figures 77 and 78). The results do not change when using other model configurations and become even less significant when lowering the gas temperature at the inlet of the bundle.

8.2.4 Hot Startups

8.2.4.1 Old Bundle Geometry

Experiments with hot startups lead to severe instabilities under specific circumstances, so the results are thoroughly discussed in this chapter. Since the outcome of the experiments is largely the same for all startup times and inlet gas temperatures, those experiments with a startup time of 10 minutes and at an inlet gas temperature (after the startup is finished of course) of 710°C are mainly presented here. The specifics of startups using the new bundle geometry are discussed in the next chapter.

Figure 81 shows the combined mass flows of bundle subsections for a startup without separation of the feeding and rising system (model parameter permutation number 2).

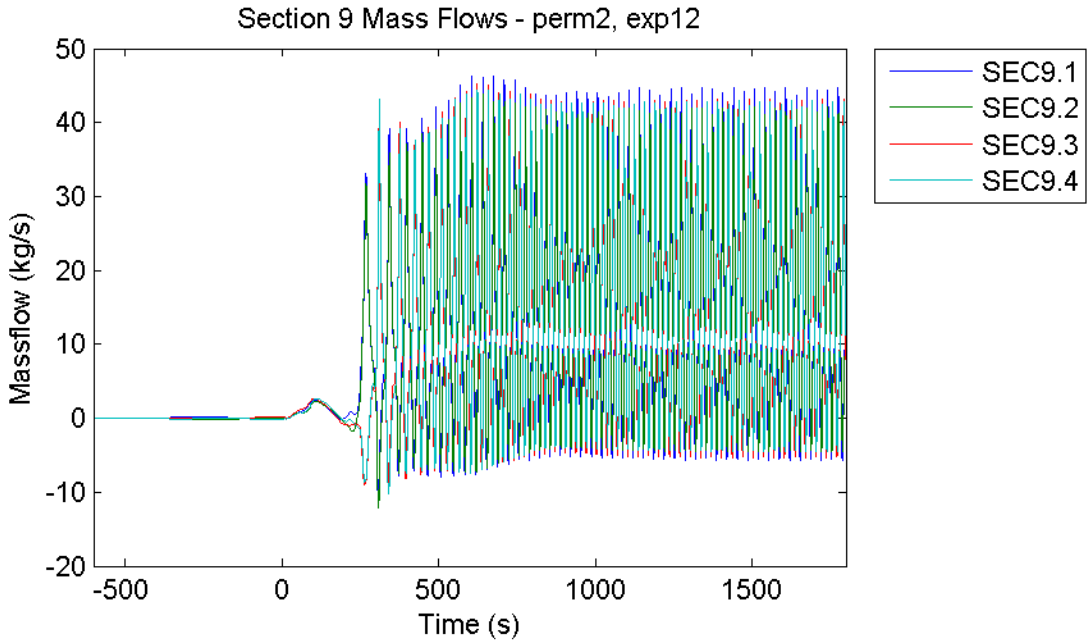

Figure 81: Mass Flows of Bundle Subsections – Perfect Blind Plates, Not Separated Feeding / Rising System, Final Inlet Gas Temperature 710 °C, Hot Startup over 10 min

One can see heavy mass flow oscillations in all subsections of the convective evaporator bundle, partially reaching negative values. This means that the mass flows in the tubes periodically stop or become very slow, leaving the tubes uncooled and vulnerable for heat damages. A closer look at the graph reveals more information, figure 82.

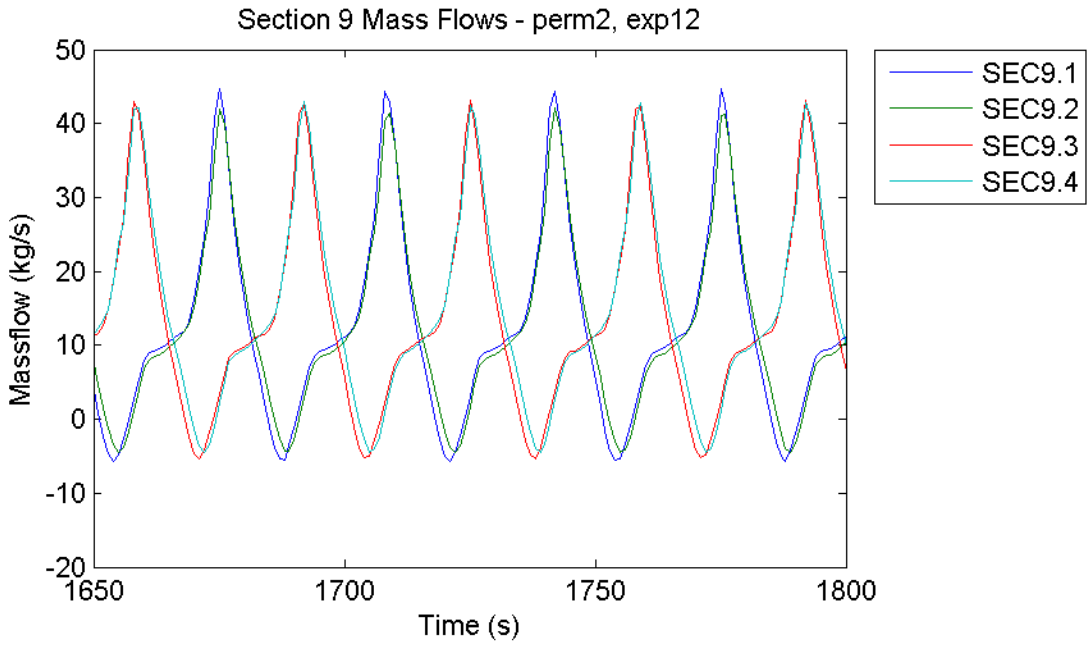

Figure 82: Mass Flows of Bundle Subsections (Detail 1) – Perfect Blind Plates, Not Separated Feeding / Rising System, Final Inlet Gas Temperature 710 °C, Hot Startup over 10 min

Figure 82 only shows the last 150 seconds of the startup experiment. One can clearly see that sections 9.1 and 9.2 (left side of the convective evaporator bundle) are almost perfectly in sync, just as sections 9.3 and 9.4 (right side) are. There are no major differences between single tubes of a subsection. The phase shift between the left and right side is 180°, meaning that higher mass flows through the bundle are alternating between the sides. This has to be accompanied by a compensating mass flow between the sides, which can only occur at the blind plates or at the points of separation. Figure 83 shows these mass flows.

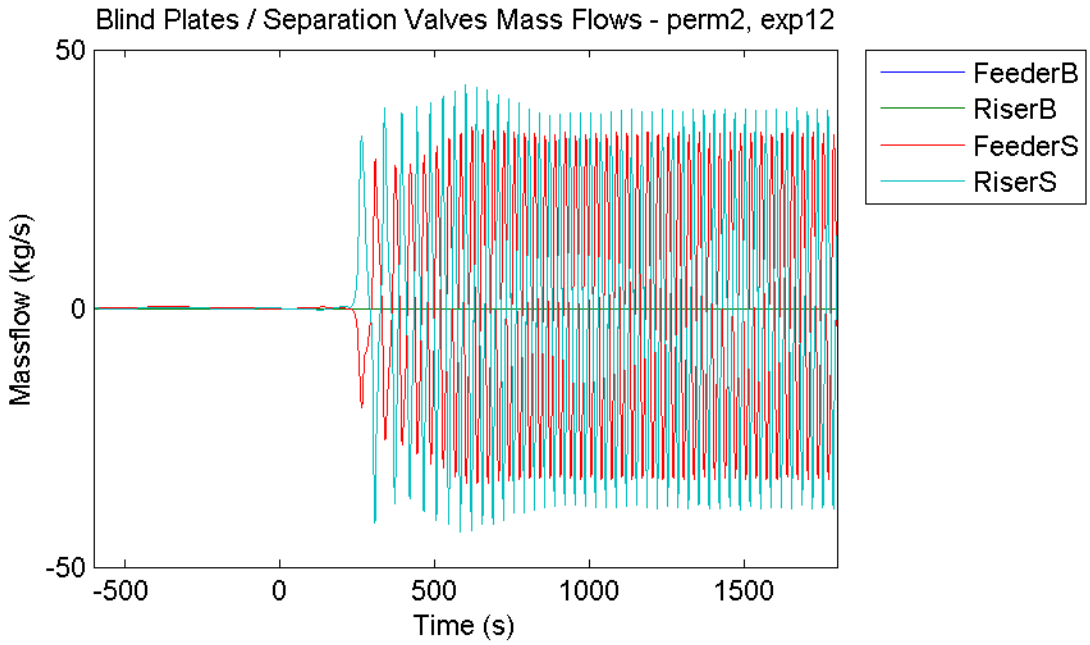

Figure 83: Mass Flows between Sides – Perfect Blind Plates, Not Separated Feeding / Rising System, Final Inlet Gas Temperature 710 °C, Hot Startup over 10 min

Positive values denote mass flows from the left to the right side. Of course, since the blind plates are considered to be perfect for model parameter permutation number 2, the mass flows at the blind plates remain zero. Otherwise, the graph confirms the previous suspicion. As the phase shift of oscillations between the top (RiserS) and bottom (FeederS) point of separation is also 180° and coincide with the mass flow oscillations of the two sides of the bundle, it is likely that negative (downward) mass flows in one side of the bundle move through the bottom point of separation to the other side. This would lead to similar oscillations at the feeder tubes between the bottom two horizontal headers of the main feeding system (sections 6.1 to 6.10). Figure 84 shows these mass flows.

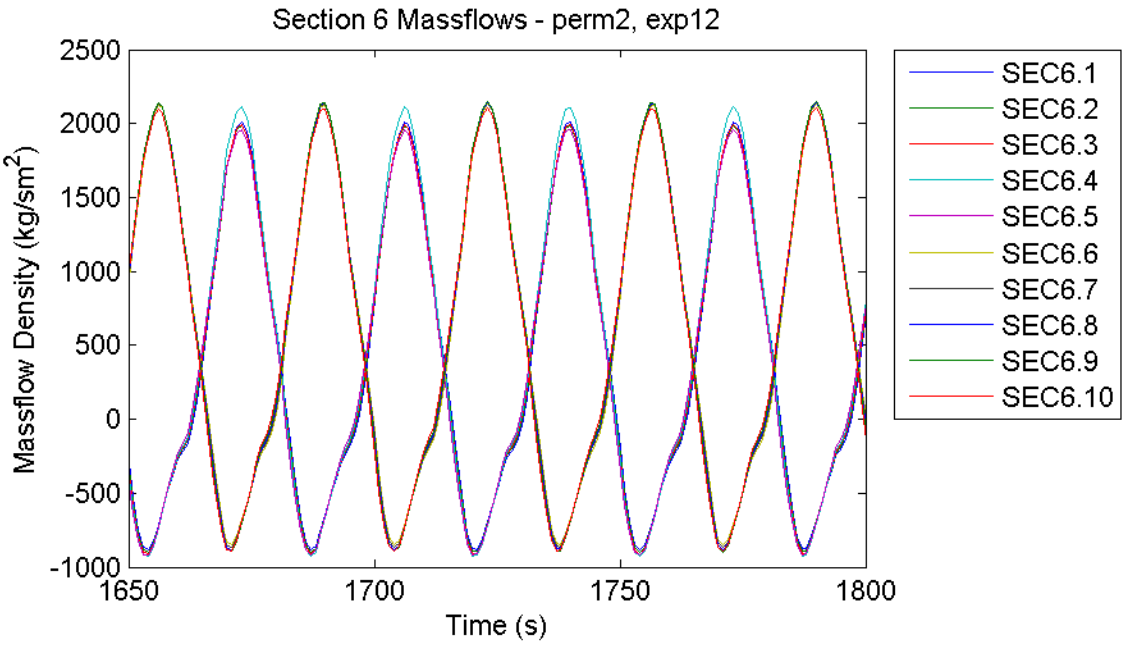

Figure 84: Mass Flows of bottom Feeder Tubes (Detail) – Perfect Blind Plates, Not Separated Feeding / Rising System, Final Inlet Gas Temperature 710 °C, Hot Startup over 10 min

Again, the graph only shows the last 150 seconds of the experiment. All the left side feeding tubes (sections 6.1-6.5) are in sync such as all the right side feeding tubes (sections 6.6-6.10). A comparison with figure 82 confirms the previous assumption that the oscillations occur globally between both sides of the convective evaporator bundle, as illustrated in figure 85.

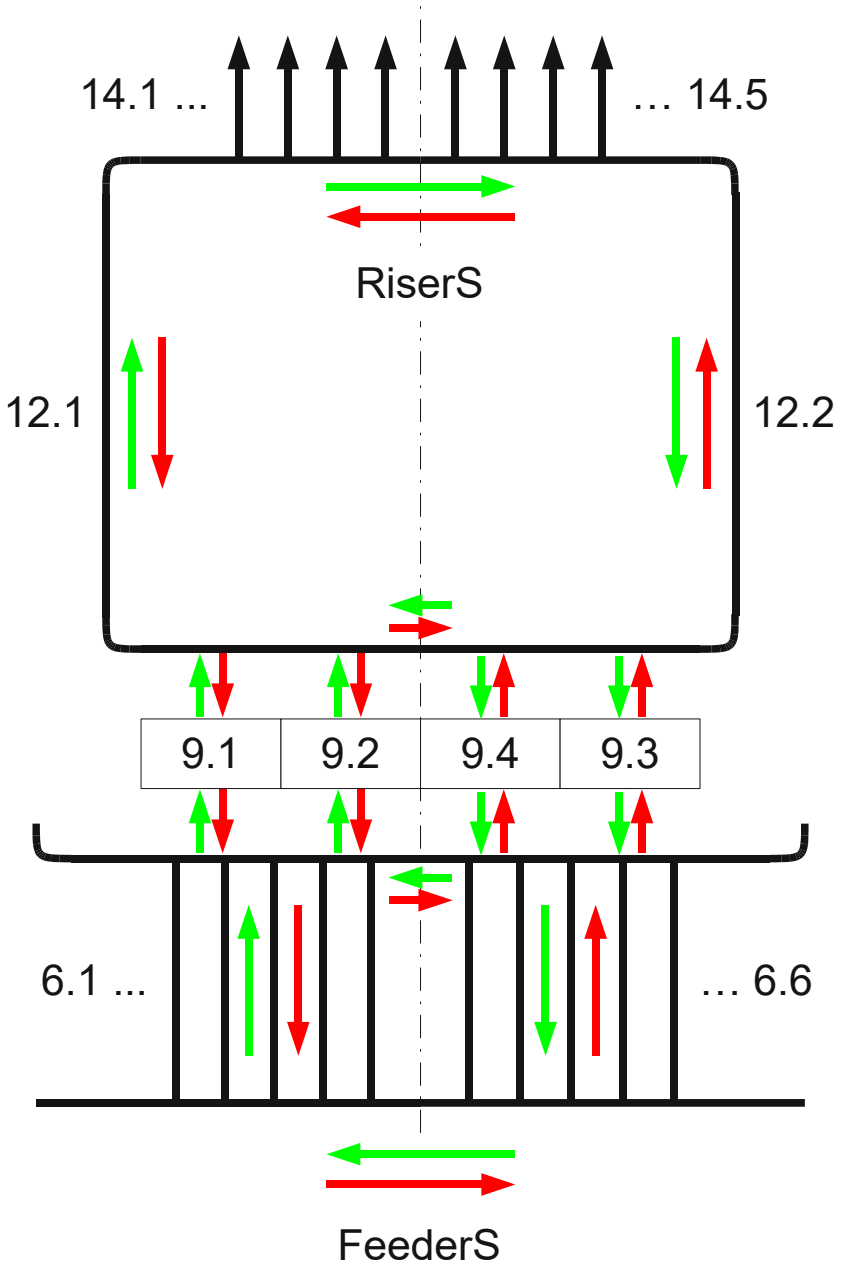

Figure 85: Illustration of Bundle Oscillations

Every color (green and red) represents one possible flow scheme. The oscillations are alternating between the two. The numbers or names of previously mentioned sections are also included. The mass flows between the blind plates at the headers directly below and above the bundle (section 9) only become relevant when using the new bundle geometry, see next chapter.

Clearly, these global circulations are only possible because both sides are connected with each other at the top and bottom horizontal header (RiserS and FeederS). When separating both sides at those points, such circulations are not possible and the outcome of a hot startup experiment is entirely different, as figure 86 shows.

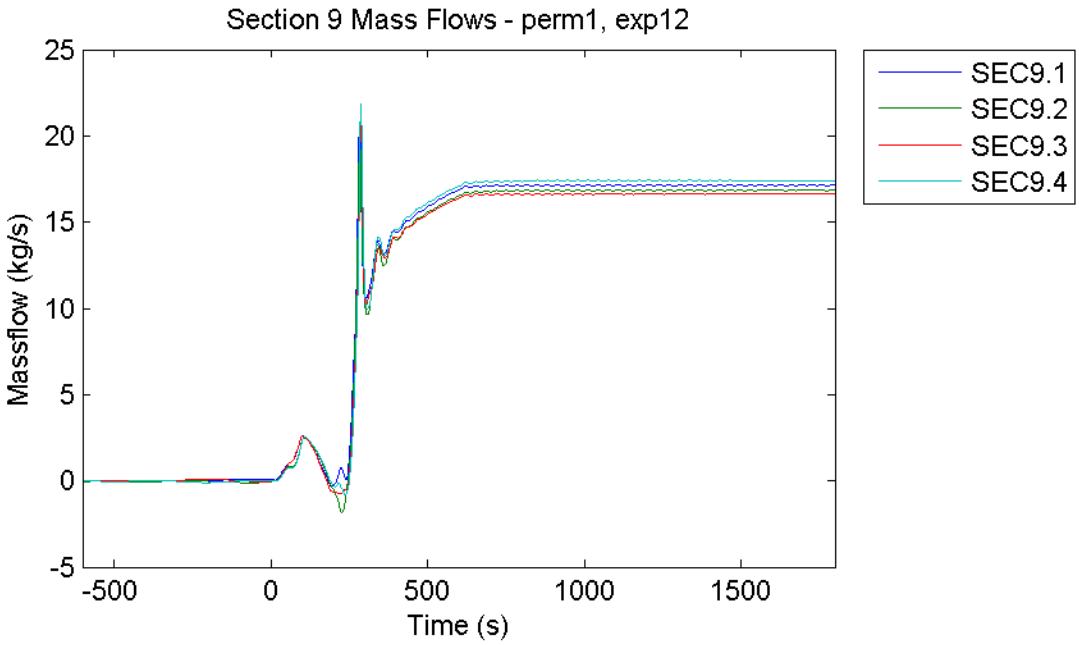

Figure 86: Mass Flows of Bundle Subsections – Perfect Blind Plates, Separated Feeding / Rising System, Final Inlet Gas Temperature 710 °C, Hot Startup over 10 min

Now all the mass flows through the subsections coincide for the most part and reach a stable state with very little oscillations. The total separation of both sides successfully suppressed the occurrence of global circulations. This is also the reason why the separation / non separation at the top and bottom horizontal headers was introduced as a model parameter.

All observations up to this point do not explain why the circulations occur when the sides are not separated. Taking a look at the pressure differences at the blind plates and points of separation can help with that, as illustrated by figure 87.

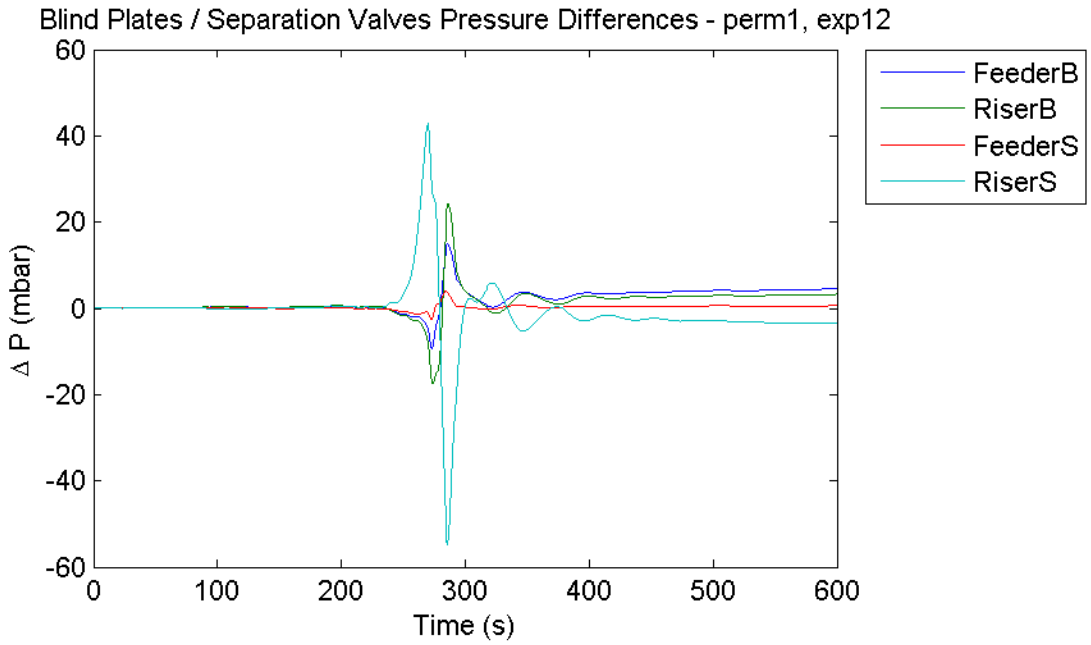

Figure 87: Pressure Differences between Sides (Detail) – Perfect Blind Plates, Separated Feeding / Rising System, Final Inlet Gas Temperature 710 °C, Hot Startup over 10 min

Positive values mean that the pressure on the left side is higher than on the right side. The graph shows the pressure differences at the blind plates and points of separation for completely separated sides (model parameter permutation number 1). One can see the very large positive spike at the top point of separation (RiserS) before turning into an even larger negative spike right after it. Pressure differences at the blind plates are similar, but not as severe and in reverse directions. Pressure differences at the bottom point of separation (FeederS) are very small in comparison to the other ones. All oscillations are muffled fairly quickly and the pressure differences stay at their respective values after about 600 seconds.

When the feeding and rising system is not separated, those pressure differences are compensated by mass flows. This is especially true for the points of separation, where the pressure loss due to friction is very small, which leads to high mass flows even at rather low pressure differences. Imperfect blind plates still have a form loss coefficient of 350, allowing them to compensate the pressure differences with very small mass flows. That is also the reason why hot startups with imperfect blind plates but an otherwise separated feeding / rising system also do not cause any instabilities. For example, a hot startup with model parameter permutation number 3 over 10 minutes looks very similar with permutation number 1 (figure 86).

The reason why those spikes in the pressure differences between the sides occur can be explained with a look at the static pressure losses of section 12, which is the two connections between the two top horizontal headers (see figure 85):

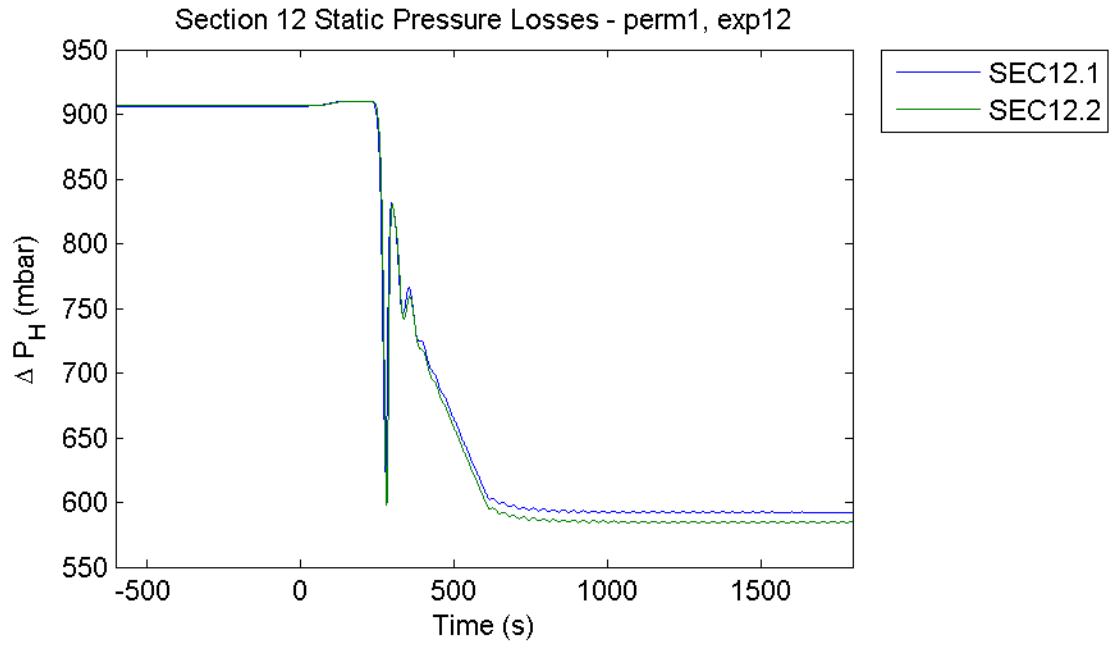

Figure 88: Static Pressure Losses of Main Risers – Perfect Blind Plates, Separated Feeding / Rising System, Final Inlet Gas Temperature 710 °C, Hot Startup over 10 min

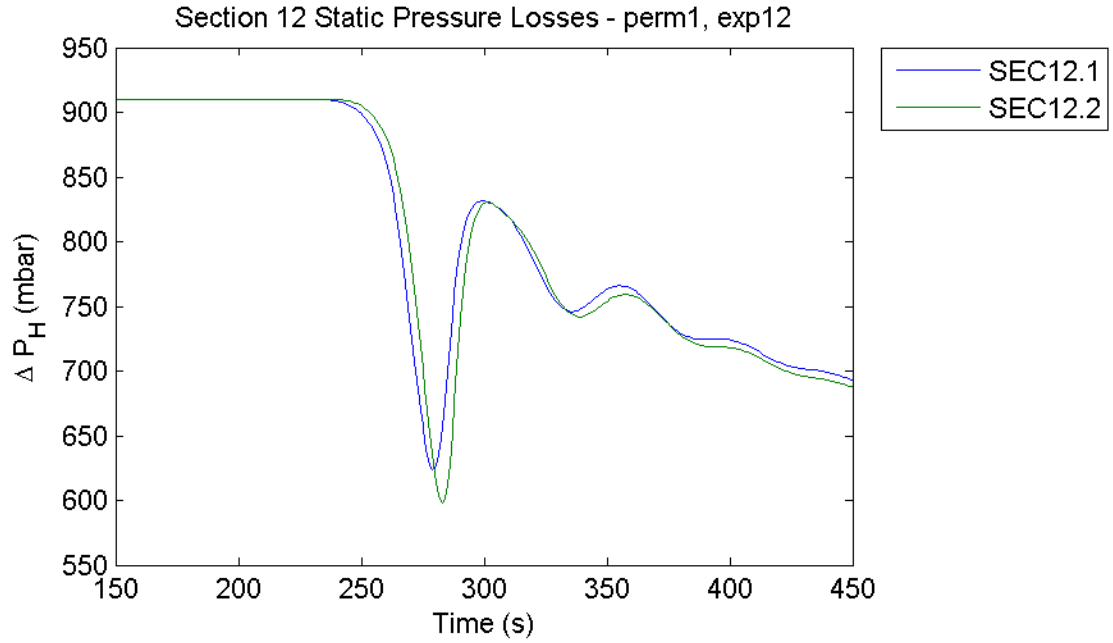

Figure 89: Static Pressure Losses of Main Risers (Detail) – Perfect Blind Plates, Separated Feeding / Rising System, Final Inlet Gas Temperature 710 °C, Hot Startup over 10 min

The first graph, figure 88, shows an overview of the static pressure differences in the main risers. The course of the static pressure loss follows the one of fluid density, as already explained in chapter 7.2 . At the start of evaporation in the convective evaporator bundle, the fluid inside the bundle is not flowing yet, which means that the created steam is not leaving the bundle fast enough and large amounts of steam are rapidly produced. This first burst of steam then leaves the

bundle through the main risers (section 12), which results in the sharp downwards spike in the static pressure difference in the figures above. The now accelerated fluid in the bundle causes the steam mass fraction to decline again, which is why the static pressure loss increases quickly after the downwards spike. After the startup is finished, a steady production of steam leads to constant static pressure losses in the main risers.

A detailed view of figure 88 between 150 and 450 seconds is shown in figure 89. One can clearly see that the downward spike occurs earlier on the left side (section 12.1) than on the right side. The time difference is about 4 seconds. So when the first burst of steam is produced on the left side, it travels up the left main riser and hits the top point of separation, increasing the pressure there. Shortly after that, the steam burst on the right side hits the point of separation from the right, increasing the pressure from the other side. That explains the sequence of spikes in pressure difference at the top point of separation (RiserS) in figure 87. Because the steam burst on the right side is stronger than on the left side (the downwards spike in figure 89 is larger on the right side), the negative spike in figure 87 is larger than the positive one.

The difference in size and chronological occurrence of steam bursts between the left and right side can only be explained by the slight geometrical asymmetry between the two sides, as, for example, shown in figure 28 on page 42: The left side of the convective evaporator bundle, sections 9.1 and 9.2, consists of 30 rows, while the right side, section 9.3 and 9.4, consists of 31 rows, so one more. The smaller total mass of fluid on the left side can be more easily accelerated while the total steam production is higher on the right side. That is why the steam burst occurs earlier on the left side, but is stronger on the right side.

If the sides are not separated at the top point of separation (RiserS in figure 85), the first steam burst from the left side pushes the liquid in the right main riser (section 12.2) back into the right side of the convective evaporator bundle. This forces the evaporating fluid to stay longer inside the bundle, causing more evaporation and increasing pressure in the bundle. Once the pressure is high enough and the pressure wave from the left side has faded, the steam bursts through the right main riser up to the horizontal header, causing another pressure wave which pushes back the fluid in the left main riser (section 12.1). That causes the fluid in the left side of the bundle to slow down, causing more evaporation and the cycle starts again with the next steam burst from the left side. This mechanism can also be observed from the static pressure losses in the main risers, figure 90.

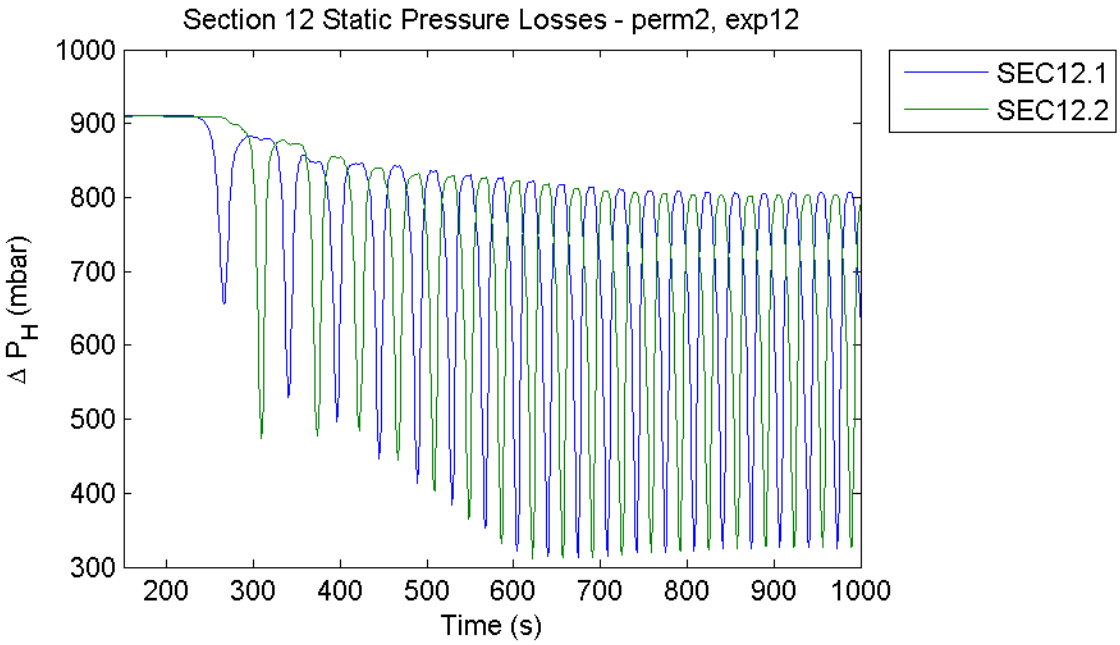

Figure 90: Static Pressure Losses of Main Risers (Detail) – Perfect Blind Plates, Not Separated Feeding / Rising System, Final Inlet Gas Temperature 710 °C, Hot Startup over 10 min

In comparison to a startup with separated sides (figure 89), it is clear to see that the first steam burst from the left side (through section 12.1) slowed down the emergence of the steam burst from the right side significantly: The first two spikes in figure 90 are now about 43 seconds apart, compared to only 4 seconds when the system is separated. The first steam burst on the right side is also much stronger than before, which is also caused by the delay. All these observations are in line with the proposed mechanism described before.

The separation of both sides at the top point of separation (RiserS) does not stop the steam bursts or the pressure waves caused by them (as one can clearly see from the spikes in figure 87), but it reflects the pressure waves to counteract them self. When the system is not separated, the pressure waves can run through the opposite side practically unopposed, which makes them more effective in stopping the fluid there.

There are some circumstances that might enhance the described effects and thereby support the emergence of this instability:

- The two top horizontal headers connected by section 12 (see figure 85) are quite far apart. The vertical distance between them is 12.645 m. Even at a stable state, the static pressure loss is still about 0.6 bar, and over 0.9 bar for pure liquid at a “cold” (unheated) state, see figure 88. When a steam burst travels through one of the main risers, the static pressure loss causes additional flash evaporation, further strengthening the burst. Therefore, a shorter distance between the two horizontal headers might improve stability.

- The design of the top horizontal header poses an inherent problem, as already mentioned in chapter 7.3 : it acts like a centrifugal separator, causing the liquid to flow further inwards than the steam. Due to this, the steam is primarily flowing from the header into the steam drum through the outer risers rather than the inner ones, as figure 91 shows.

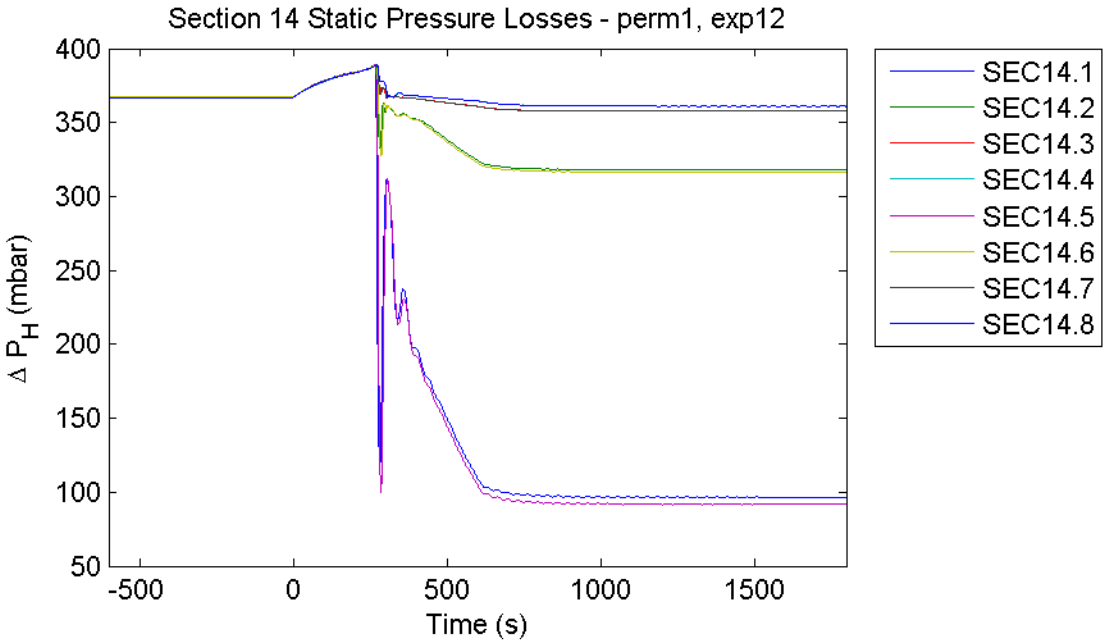

Figure 91: Static Pressure Losses of Top Risers – Perfect Blind Plates, Separated Feeding / Rising System, Final Inlet Gas Temperature 710 °C, Hot Startup over 10 min

The graph shows the static pressure losses of the risers between the top horizontal header and the drum (section 14, see figure 85) for a stable hot startup experiment. Figure 54 on page 73 shows essentially the same results for stationary status. As most of the steam leaves the top horizontal header through the outer risers, a steam burst traveling up one of the main risers (sections 12.1 and 12.2) comprises mostly of liquid when it reaches the middle of the top horizontal header and pushes into the other side (when the system is not separated). The incompressibility of the liquid makes it harder to damp the resulting pressure wave, thereby enhancing the following effects.

This centrifugal separation can also be observed in an unstable system, figure 92.

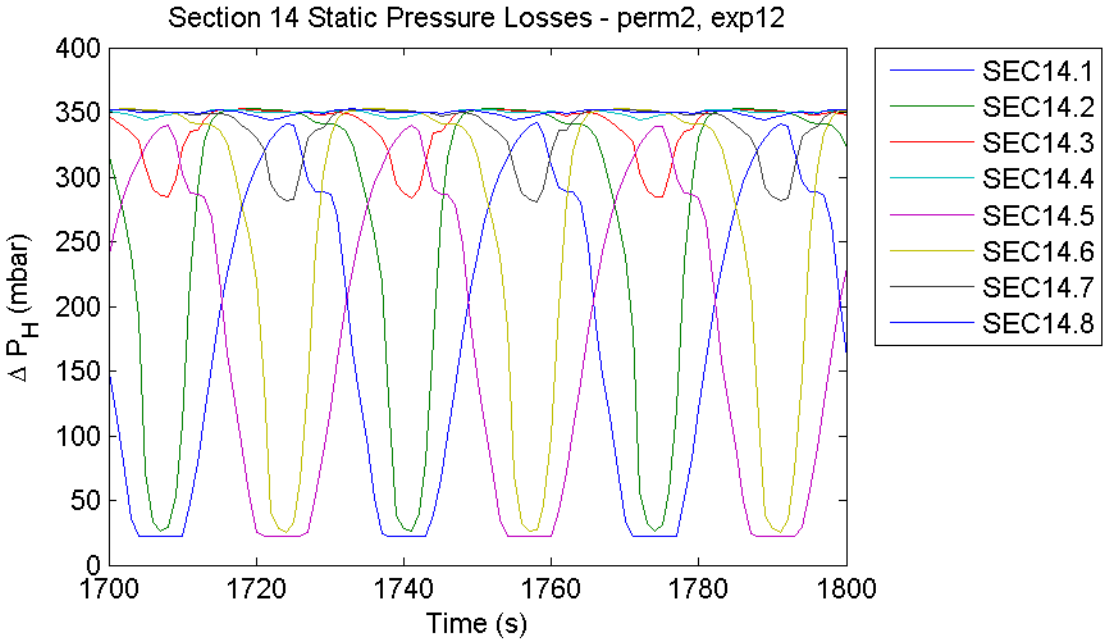

Figure 92: Static Pressure Losses of Top Risers (Detail) – Perfect Blind Plates, Not Separated Feeding / Rising System, Final Inlet Gas Temperature 710 °C, Hot Startup over 10 min

It only shows the last 100 seconds of a hot startup experiment with a not separated feeding and rising system. While the 2 outermost risers on each side, sections 14.1, 14.2, 14.5 and 14.6, transport most of the steam and the risers one spot to the middle, sections 14.3 and 14.7 transport only very small amounts of steam, the innermost risers, sections 14.4 and 14.8, transport virtually no steam. This confirms the previous assumption that the pressure waves mainly consist of incompressible liquid.

- The asymmetry between the left and right side of the convective evaporator bundle seems rather insignificant: the right side has one row more than the left side (31 instead of 30), which is only about 3.3 %. However, the fact that the difference between the left and the right side is so small might even cause more problems: if the start of evaporation and the emergence of steam bursts on either side would occur with a greater time period between them, then the first pressure wave would hit the opposite side at a time where evaporation was not yet close to starting there. Then the effect of slowing down the fluid in the bundle would not cause any additional production of steam, and the steam burst at that side would not be “amplified” that way. Then when the second steam burst occurred, its pressure wave would already hit a well-established flow system on the other side, possibly damping the pressure wave and eliminating its effects. The result would be a stable system.

  So a greater asymmetry could actually lead to a more stable system. This is partially confirmed by hot startup experiments with unequally heated sides, chapter 8.2.4.4 .

The actual influence of the oscillations on tube wall temperatures is shown in figure 93.

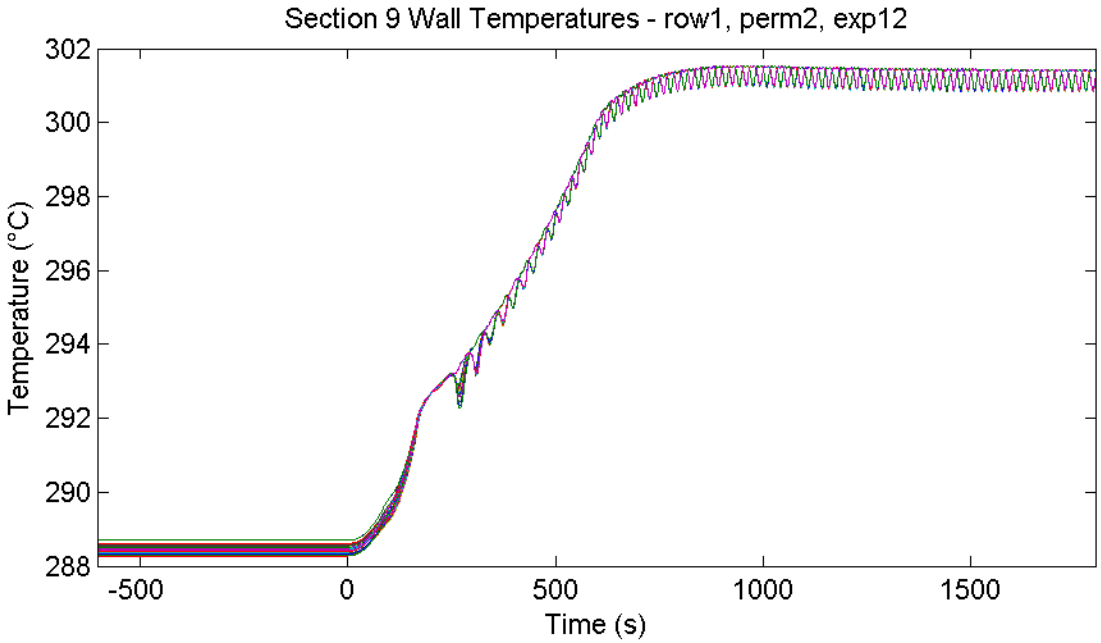

Figure 93: Collective Wall Temperatures of Bundle Tubes (Row 1) – Perfect Blind Plates, Not Separated Feeding / Rising System, Final Inlet Gas Temperature 710 °C, Hot Startup over 10 min

Each line in the figure represents the average of inside and outside wall temperatures of an entire pipe in the first (horizontal) row in the convective evaporator bundle. All 61 tubes of the row are included in the graph. Tubes in other rows show similar wall temperatures. One can see that the wall temperature oscillations are only minor, about 0.6 °C in amplitude. The reason for that lies in the high frequency of oscillations (about 3 oscillations every 100 seconds), which makes the time period where the tubes are uncooled (low mass flow) very short, but also because mass flow oscillations are shifted towards positive values, as shown in figure 82 on page 104: the time in which the mass flow is negative is significantly shorter than when it is positive.

Although the temperature variations are very small, they still result in thermal stresses that can contribute to fatigue of the tubes. It is also important to remember that different local temperatures of tube walls in radial direction (for example, upper and lower half of a pipe) can-not be detected by Apros, as described in chapter 5.1.2 . So higher wall temperatures due to stratification of the flow at low mass flows can-not be observed, but are still possible. Such low mass flows especially occur at the beginning of startups.

8.2.4.2 New Bundle Geometry

Hot startups can be very different when performing them with the new bundle geometry (chapter 6.2.1). Contrary to before, hot startups with not separated feeding and rising systems can result in a stable status as long as the blind plates are perfect (model configuration permutation numbers 14, 18 and 22), but the system can still experience heavy oscillations depending on the startup time, as the following figures show.

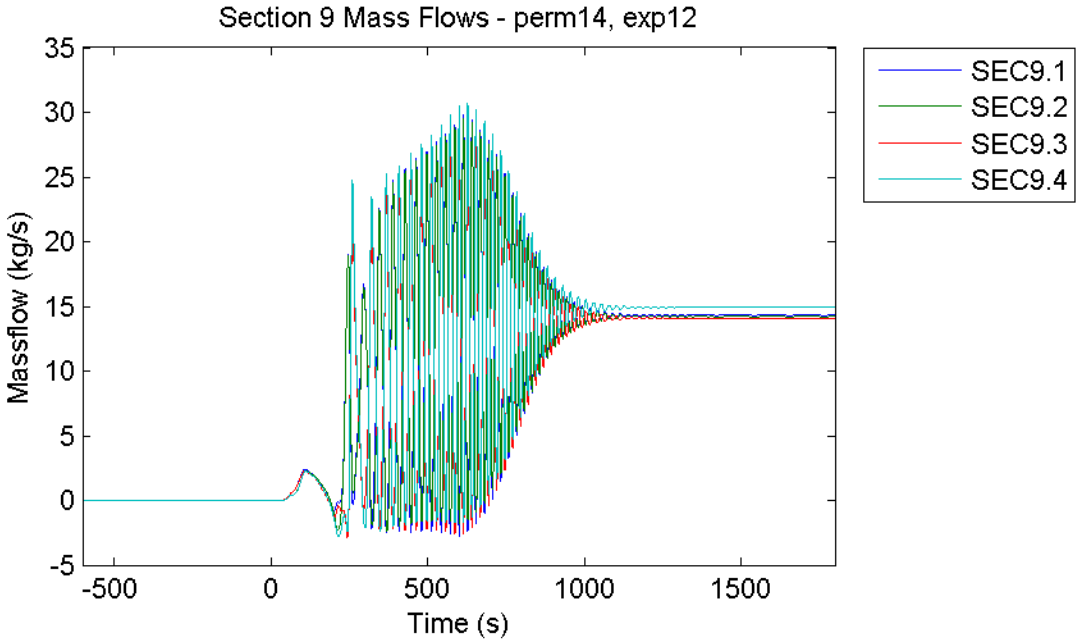

Figure 94: Mass Flows of Bundle Subsections – New Bundle Geometry, Perfect Blind Plates, Not Separated Feeding / Rising System, Final Inlet Gas Temperature 710 °C, Hot Startup over 10 min

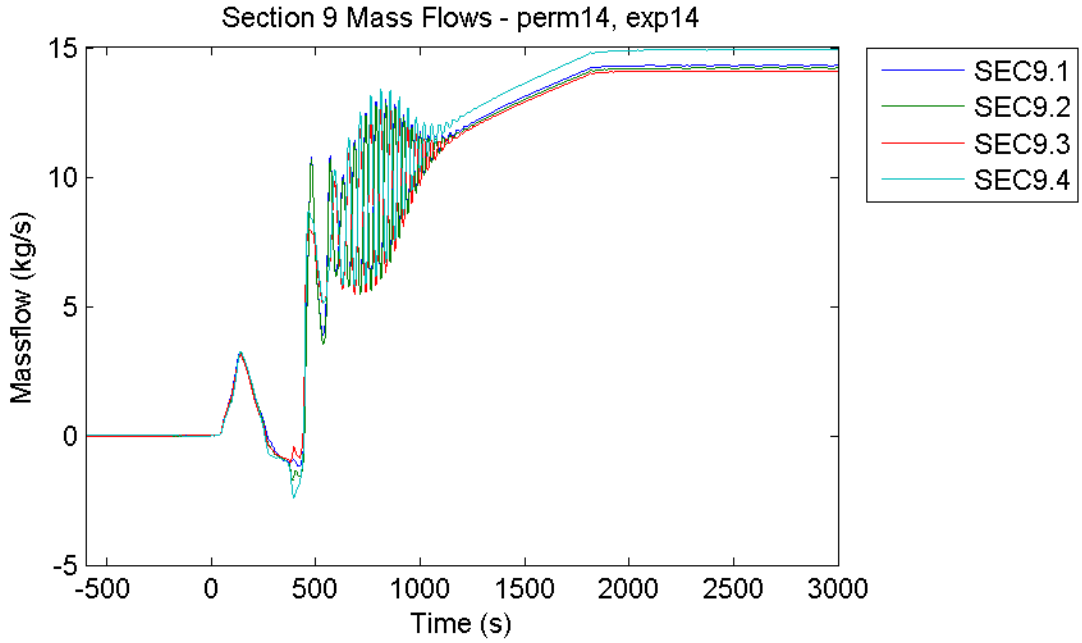

Figure 95: Mass Flows of Bundle Subsections – New Bundle Geometry, Perfect Blind Plates, Not Separated Feeding / Rising System, Final Inlet Gas Temperature 710 °C, Hot Startup over 30 min

One can see that a fast startup over 10 minutes, figure 94, causes much more oscillations than a slow startup over 30 minutes, figure 95, but they both still lead to stable systems in the end. Startups with a medium startup time of 20 minutes show only slightly worse behavior than startups over 30 minutes.

Startups with imperfect blind plates still lead to an unstable system, as figure 96 shows.

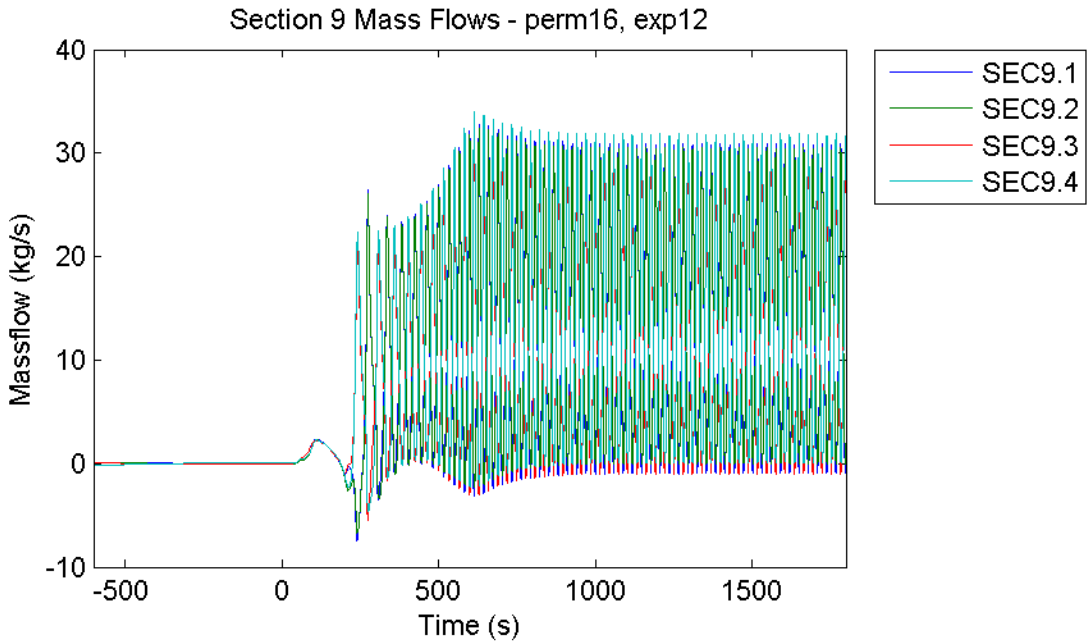

Figure 96: Mass Flows of Bundle Subsections – New Bundle Geometry, Imperfect Blind Plates, Not Separated Feeding / Rising System, Final Inlet Gas Temperature 710 °C, Hot Startup over 10 min

The oscillations, with perfect and imperfect blind plates, still follow the same mechanism described in the previous chapter with the old bundle geometry, see figure 85. So the mass flows in the left and right side of the bundle oscillate with a phase shift of 180° and become negative for short periods of time, although the negative mass flows are not as high as before. Mass flows in the feeding tubes (section 6), rising tubes (sections 12 and 14) and between the sides at the blind plates and points of separation are essentially the same as well.

A look at the pressure differences at the blind plates and points of separation for a completely separated system shows the advantages of the new bundle geometry, figure 97.

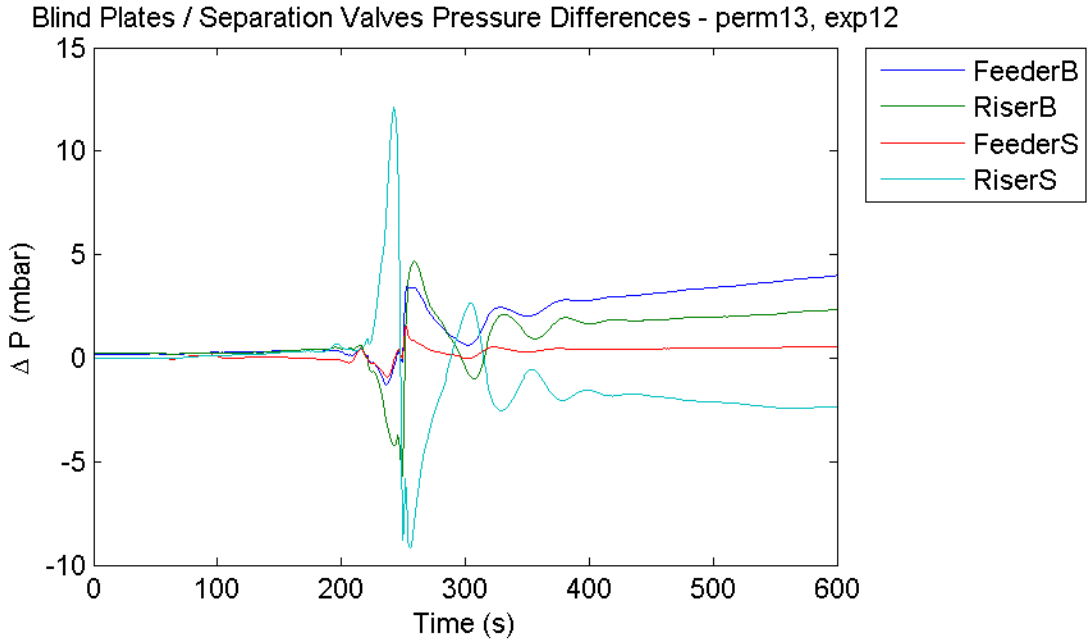

Figure 97: Pressure Differences between Sides (Detail) – New Bundle Geometry, Perfect Blind Plates, Separated Feeding / Rising System, Final Inlet Gas Temperature 710 °C, Hot Startup over 10 min

A comparison with figure 87 reveals that the spikes in pressure differences are much smaller when using the new bundle geometry, less than 27 % of the original values. For one, this is due to the generally lower steam production in the new bundle, but also because the inclined tubes make it possible that steam can flow through the tubes even in the beginning of evaporation, when the overall mass flow is still very small. This makes the steam bursts less violent, resulting in smaller pressure waves and pressure differences in the figure above.

So the new bundle geometry makes the system less vulnerable to the kind of global circulations that result from the pressure waves during startups described in the previous chapter. That leaves the question why do the oscillations still occur when both sides are interconnected via the feeding and rising system and imperfect blind plates. The explanation lies in figure 85 on page 107: the two top horizontal headers build a separate circulation system when the blind plates are imperfect. The

additional mass flow through the blind plates maintains the mass flow going up the main riser, delaying the reversal of mass flow and further enhancing the steam burst from the other side. Apparently, this effect is strong enough to cause lasting oscillations. At the old bundle geometry, suppressing the mass flow through the blind plates alone is not sufficient to stop the occurrence of global circulations when the feeding / rising system is not separated.

8.2.4.3 Extra-Long Startups

Hot startups with extra-long startup times of 2 hours were performed to ensure that the instabilities did not occur due to unrealistically short startup times, even though measurements from [9] showed comparable startup times. Figure 98 shows the mass flows in bundle subsections, comparable to figure 81 on page 103.

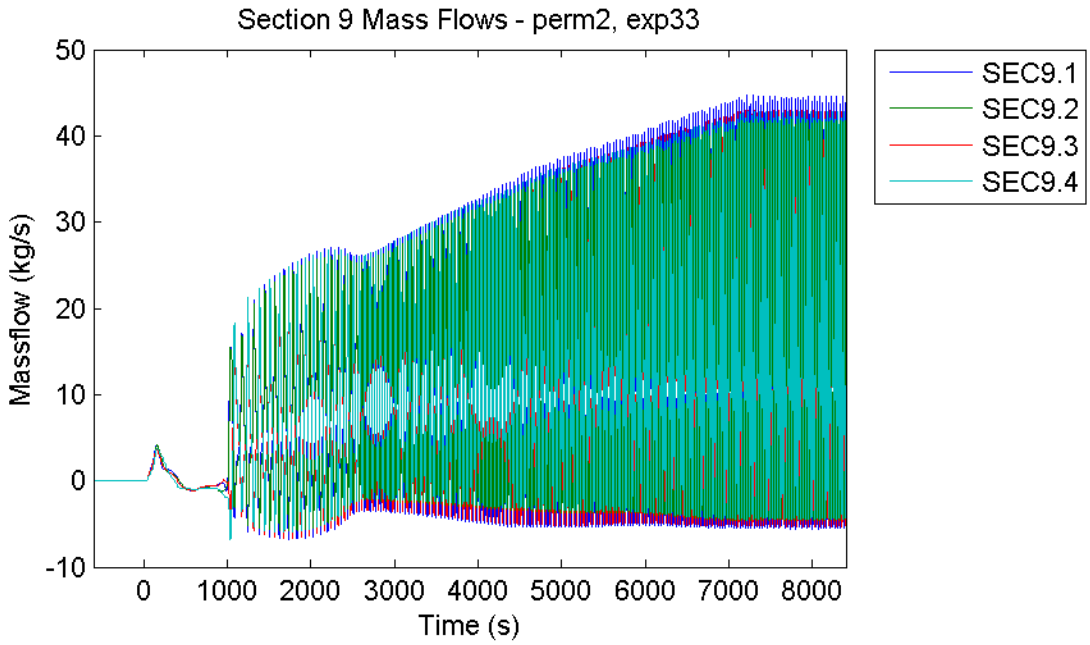

Figure 98: Mass Flows of Bundle Subsections – Perfect Blind Plates, Not Separated Feeding / Rising System, Final Inlet Gas Temperature 710 °C, Hot Startup over 2 h

It is clear to see that the same oscillations occur at the same severity, they only start at a later time. The reason for this is that the main event that starts the oscillations, the first steam burst, is independent of the speed at which the water gets heated, so the oscillations occur no matter how long the startup time is.

8.2.4.4 Extra Long Startups with Uneven Heating and Imperfect Blind Plates

These experiments were performed to further investigate the influence of imperfect blind plates. They did not lead to any new conclusions regarding the blind plates, but they were (at least partially) able to confirm a theory proposed in chapter 8.2.4.1 : that a greater asymmetry between the left and right side could make the system more stable. Figure 99 shows the mass flow in each subsection of the convective evaporator bundle for a startup where the heat flux on the right side (sections 9.3 and 9.4) was reduced to about 50 % the nominal value.

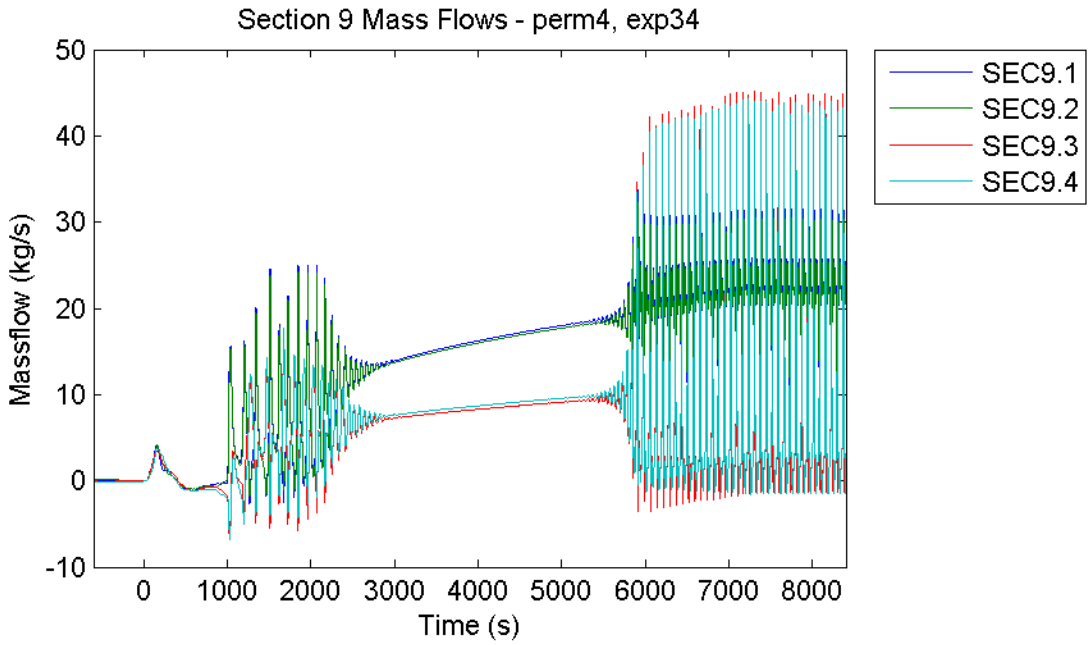

Figure 99: Mass Flows of Bundle Subsections – Imperfect Blind Plates, Separated Feeding / Rising System, Final Inlet Gas Temperature 710 °C, Hot Startup over 2 h, 50 % Heat Flux on Right Side

It is clear to see that the oscillations in the beginning stabilize after some time before restarting again. The initial oscillations also have a significantly lower frequency than usual. This confirms the assumption that, due to the greater asymmetry, the time difference between the steam bursts from both sides is so large that they do not have an enhancing effect on each other anymore.

However, the oscillations then restart again with the same mechanism as usual, even though there is no steam burst to start the oscillations anymore. Apparently, the ever growing discrepancy in steam production between the sides can result in high enough pressure differences to slow down mass flow in the weaker heated system and restart the cycle again. This can also be shown by a detailed look at the oscillations, figure 100.

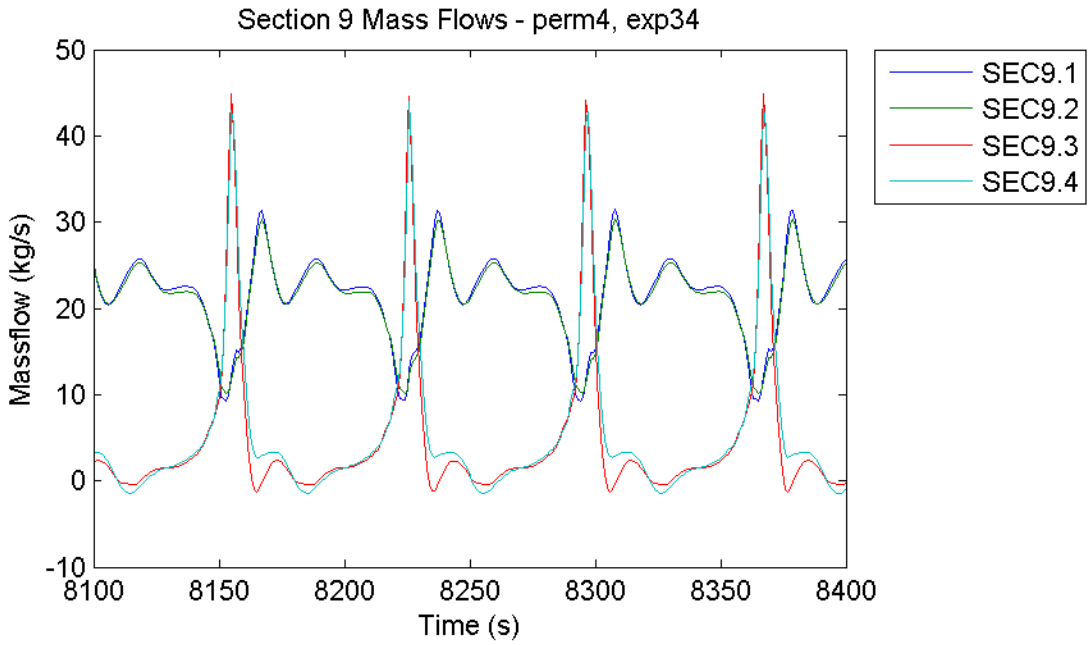

Figure 100: Mass Flows of Bundle Subsections (Detail) – Imperfect Blind Plates, Separated Feeding / Rising System, Final Inlet Gas Temperature 710 °C, Hot Startup over 2 h, 50 % Heat Flux on Right Side

Figure 100 shows only the last 300 seconds of figure 99, when the oscillations are already well established. One can see that the mass flow on the weaker heated side (sections 9.3 and 9.4) is kept very low by the other side, resulting in a steam burst represented by a large spike. Because of the generally lower steam production of that side, the steam burst does not affect the other side as much as it did at previous experiments with equally heated sides. The mass flow on the left side never reaches negative values and no larger steam burst emerges from that side, but its higher steam production suppresses major mass flows at the other side, resulting in another steam burst and the cycle starts again.

In conclusion, hot startup experiments with unequally heated sides of the convective evaporator bundle did not lead to any new information about the influence of imperfect blind plates, but they were able to show that a great imbalance of heating between the sides can lead to similar oscillations as encountered before.

8.2.5 Influence of Foreign Objects

Experiments with foreign objects did not show any instabilities. Foreign objects only affected the tubes that they were placed in and did not slow down mass flow severely enough to cause overheating. Figure 101 shows the mass flows of all pipes in the first (horizontal) row of the convective evaporator bundle when a foreign object is placed in the first pipe of section 9.2.8 (experiment number 15, see figure 57).

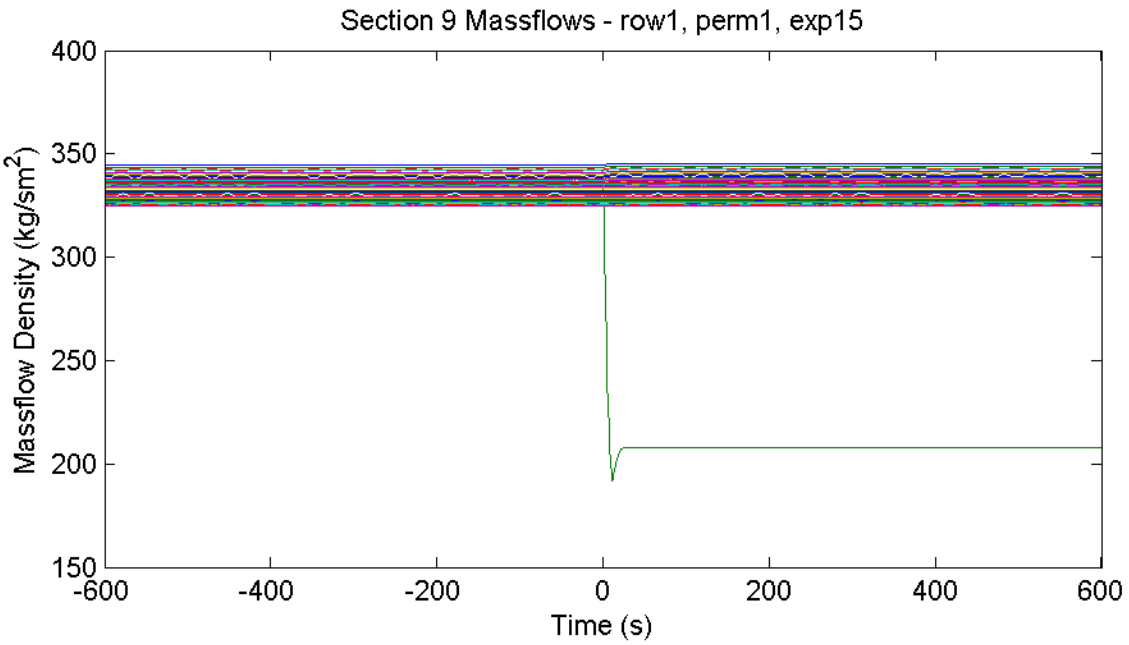

Figure 101: Collective Mass Flow Densities of Bundle Tubes (Row 1) – Perfect Blind Plates, Separated Feeding / Rising System, Final Inlet Gas Temperature 710 °C, FO in Section 9.2.8.1

The line with the lower mass flow represents the tube where the foreign object was placed in (section number 9.2.8.1). Apart from this one, no other tubes showed any unusual behavior. Since the outside conditions (gas temperature) did not change, the lower mass flow led to a higher steam quality, as figure 102 shows.

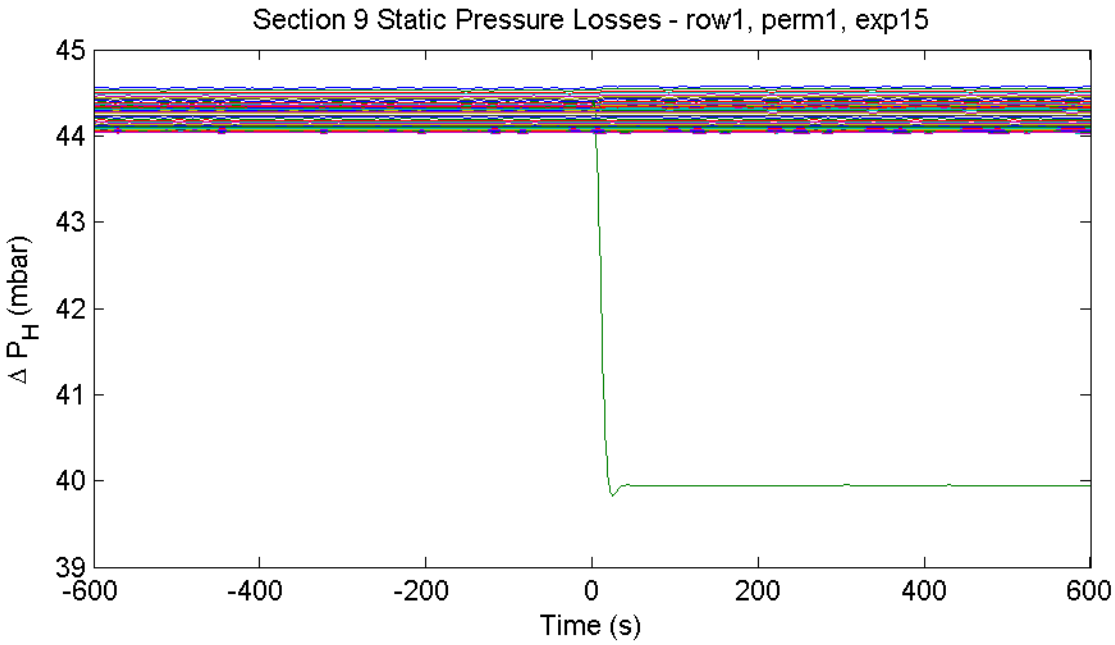

Figure 102: Collective Static Pressure Losses of Bundle Tubes (Row 1) – Perfect Blind Plates, Separated Feeding / Rising System, Final Inlet Gas Temperature 710 °C, FO in Section 9.2.8.1

The static pressure difference of 40 mbar in the first tube indicates an average steam mass fraction of about 2 %, corresponding to a volume fraction of about 24 %, compared to the mass and volume fractions in the other tubes of 1.2 % and 16 % respectively. The critical mass fraction for the occurrence of boiling crisis is about 60 % in a vertical pipe under the same conditions, according to [4], but the reduced mass flow makes it more susceptible to stratification, as shown by the Froude numbers in figure 103.

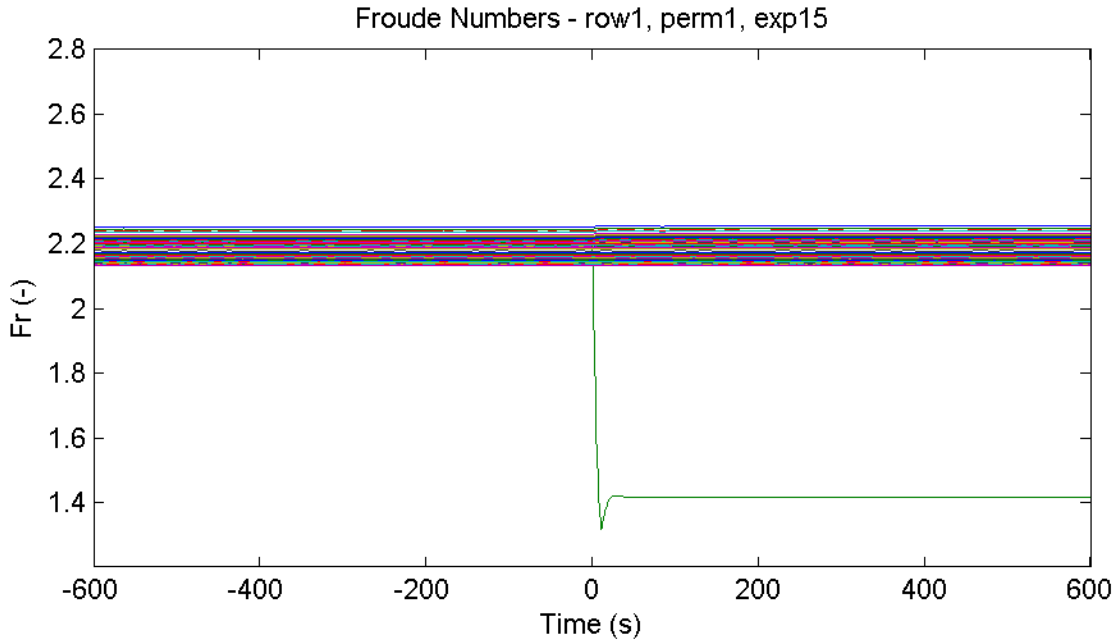

Figure 103: Collective Froude Numbers of Bundle Tubes (Row 1) – Perfect Blind Plates, Separated Feeding / Rising System, Final Inlet Gas Temperature 710 °C, FO in Section 9.2.8.1

According to [4], the very low Froude number of the blocked pipe results in a critical mass fraction of steam at the upper half of the pipe of 0, meaning that boiling crisis at the upper half would always occur due to stratification. However, the still rather low volume fraction of steam means that pipe temperatures do not necessarily reach critical values. Additional turbulence caused by the foreign object and the transitions between the horizontal and vertical parts of the pipe might also reduce stratification. In any case, Apros did not detect any (global) overheating of the pipe, as the following figure shows.

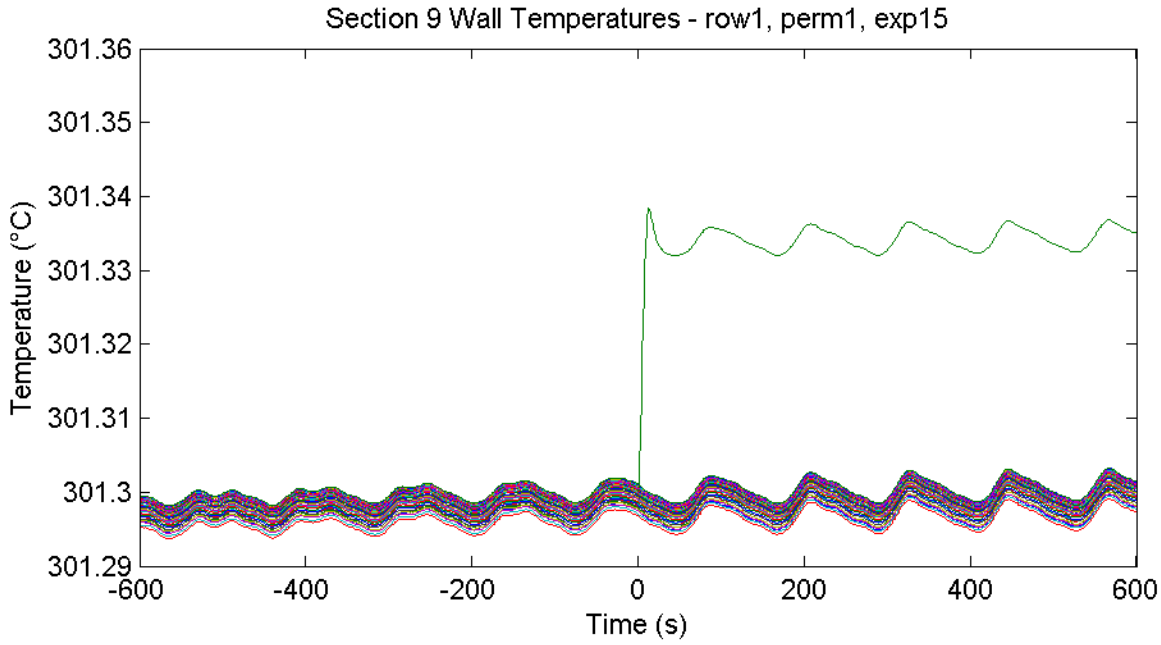

Figure 104: Collective Wall Temperatures of Bundle Tubes (Row 1) – Perfect Blind Plates, Separated Feeding / Rising System, Final Inlet Gas Temperature 710 °C, FO in Section 9.2.8.1

Although the wall temperature of the pipe was affected by the foreign object, the increase is only minimal. An increase in local wall temperatures at different parts of the pipe in radial direction (such as upper and lower half due to stratification) can not be detected by the simulation software, as described in chapter 5.1.2 .

The generally lower mass flows in inner tubes of the bundle also increase the possibility of stratified flow there. The same goes for lower mass flows due to lower heat fluxes at lower gas temperatures, although lower gas temperatures make the threat of subsequent overheating less severe. Other than lower mass flows, experiment results for other tubes or at other model parameter configurations are largely the same.

Assuming a foreign object at the connection between the vertical header of a row and the bottom horizontal header (experiment number 20, see figure 57 on page 77) did not produce any unexpected results either. While the static pressure loss through the row decreased due to the higher steam quality, the total pressure loss stayed the same, as the following figures illustrates.

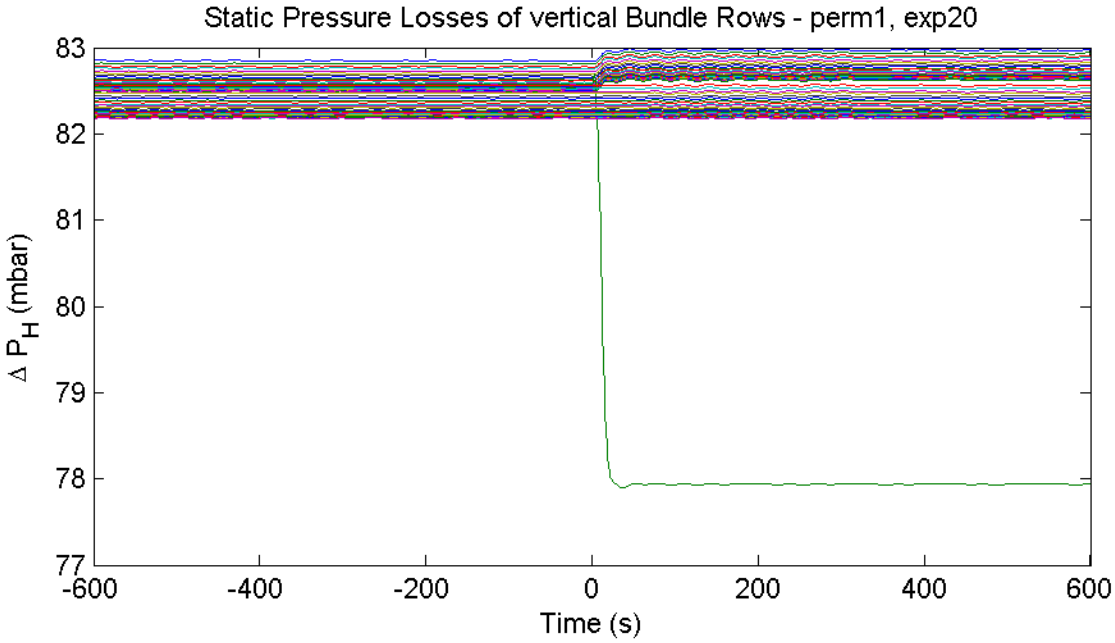

Figure 105: Collective Static Pressure Losses of Bundle Rows – Perfect Blind Plates, Separated Feeding / Rising System, Final Inlet Gas Temperature 710 °C, FO in Section 9.2.8.1

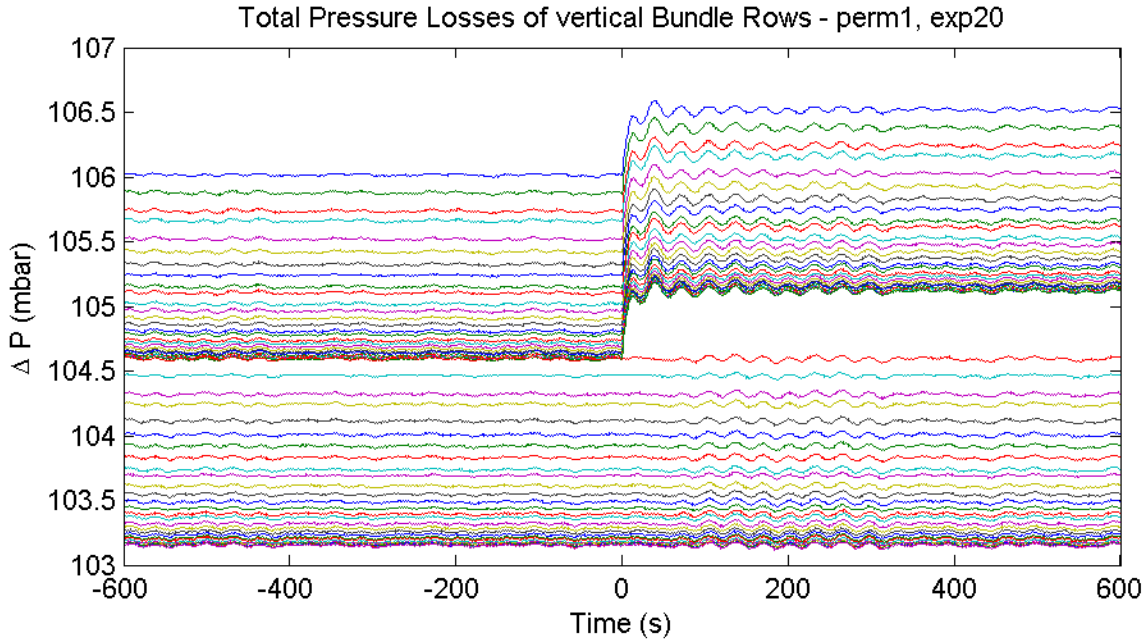

Figure 106: Collective Total Pressure Losses of Bundle Rows – Perfect Blind Plates, Separated Feeding / Rising System, Final Inlet Gas Temperature 710 °C, FO in Section 9.2.8.1

Figure 105 shows that the static pressure losses in all rows that are not affected by a foreign object but are on the same side as the row with the foreign object increase slightly. This is due to a minor increase in mass flow in those rows. This also leads to a slightly increased total pressure difference through the rows.

The total pressure difference through the rows is equal to the pressure difference between the two horizontal headers directly below and above the bundle that the vertical headers of each row are connected to. As the total pressure difference between those headers is dominated by all the other rows, the total pressure difference of the row with the foreign object has to follow the pressure difference between the horizontal headers, as figure 106 shows.

This means that a foreign object in one of the vertical headers can only shift the static pressure difference in that row towards its frictional pressure difference, but the total pressure difference (sum of static and frictional pressure differences) stays (almost) the same. Therefore, a foreign object in one of the vertical headers can never decrease the total pressure difference to 25-30 mbar in that row, as suggested by [9].

The fact that a foreign object (an increased form loss coefficient) reduces mass flow in the affected pipe(s) which could increase the risk of stratification in a horizontal pipe is not very surprising. As no other flow instabilities were detected, the experiments regarding foreign objects are considered to be stable.

8.2.6 Circulations between vertical Rows

Although the configuration of these experiments is not a realistic scenario for any real life system, they could clearly show that circulations between vertical rows of the convective evaporator bundle are highly unlikely. As an example, figure 107 shows the mass flows of the subsections of the convective evaporator bundle when setting the fouling factor of the third subsection (section 9.3, at the outer right side) to 0 over a 10 second ramp.

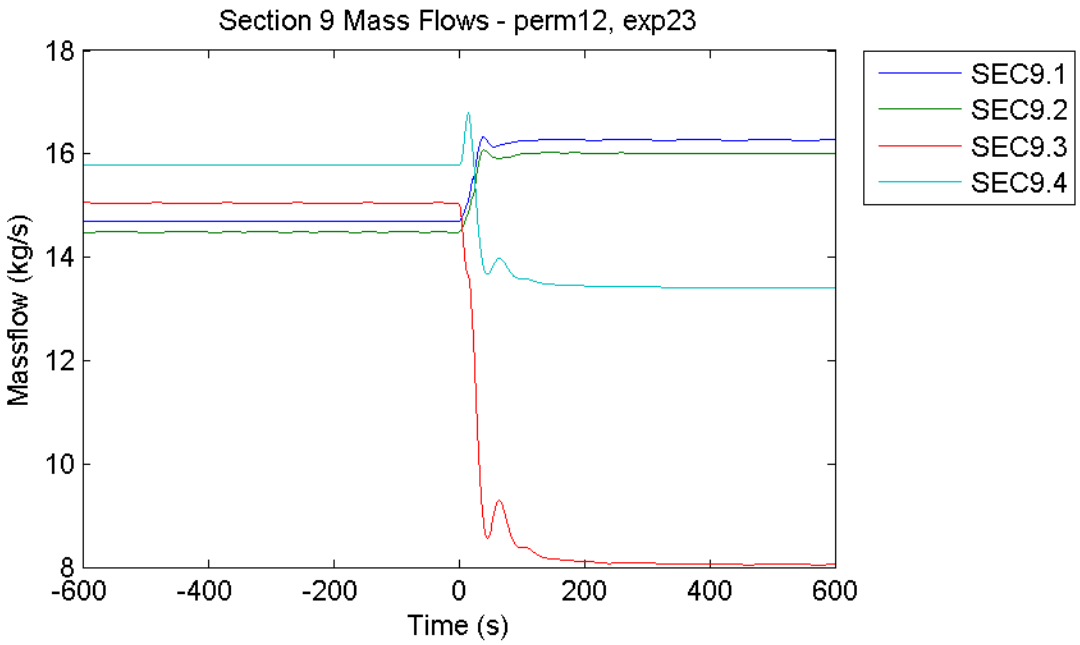

Figure 107: Mass Flows of Bundle Subsections – Imperfect Blind Plates, Not Separated Feeding / Rising System, Inlet Gas Temperature 550 °C, Fouling Factor at Section 9.3 set to 0 (10 sec Ramp)

One can see that, despite of the section being completely unheated, the mass flow in section 9.3 still remains at about 8 kg/s (collectively). Experiments at higher gas temperatures at the inlet of the bundle show a lower drop in mass flow at the affected subsection. The neighboring subsection (9.4 in this case) also shows a reduced mass flow while the subsections on the other side (9.1 and 9.2) experience an increased mass flow. This increase is reduced in the case of separated feeding and rising systems. All tubes of the respective subsections show the same behavior, so no local instabilities were detected.

The only way that a mass flow ca be maintained even through an unheated subsection is when the pressure difference between the horizontal headers directly above and below the bundle (see figure 60 on page 82) is still higher than the static pressure difference of the pure liquid in the subsection. The following figures show that this is the case.

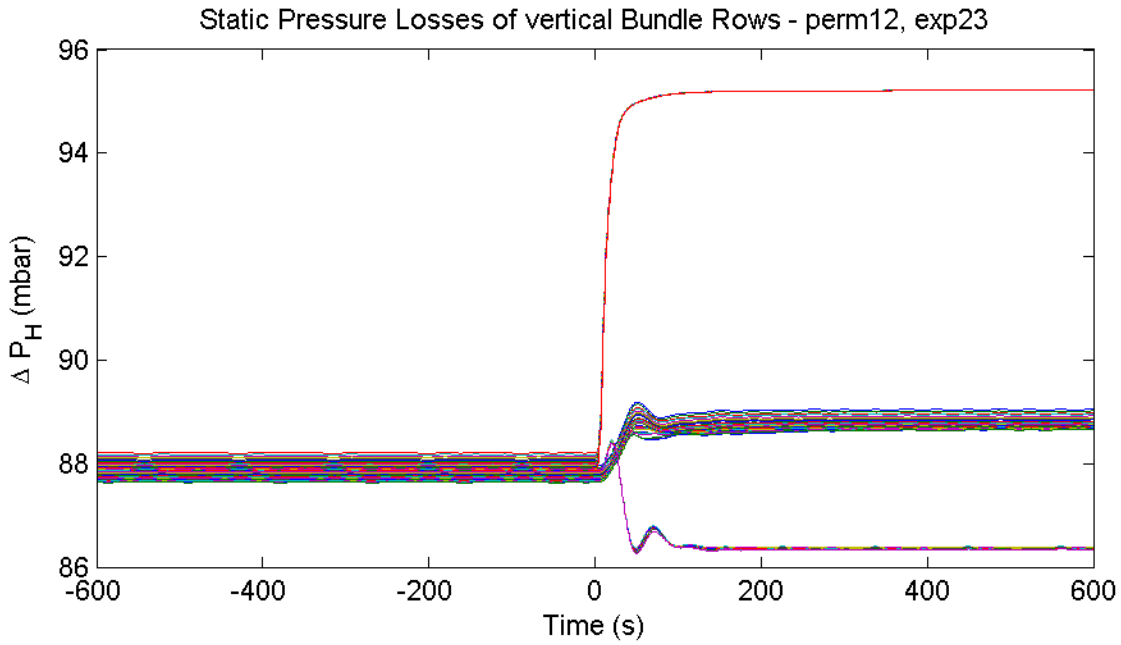

Figure 108: Collective Static Pressure Losses of Bundle Rows – Imperfect Blind Plates, Not Separated Feeding / Rising System, Inlet Gas Temperature 550 °C, Fouling Factor at Section 9.3 set to 0 (10 sec Ramp)

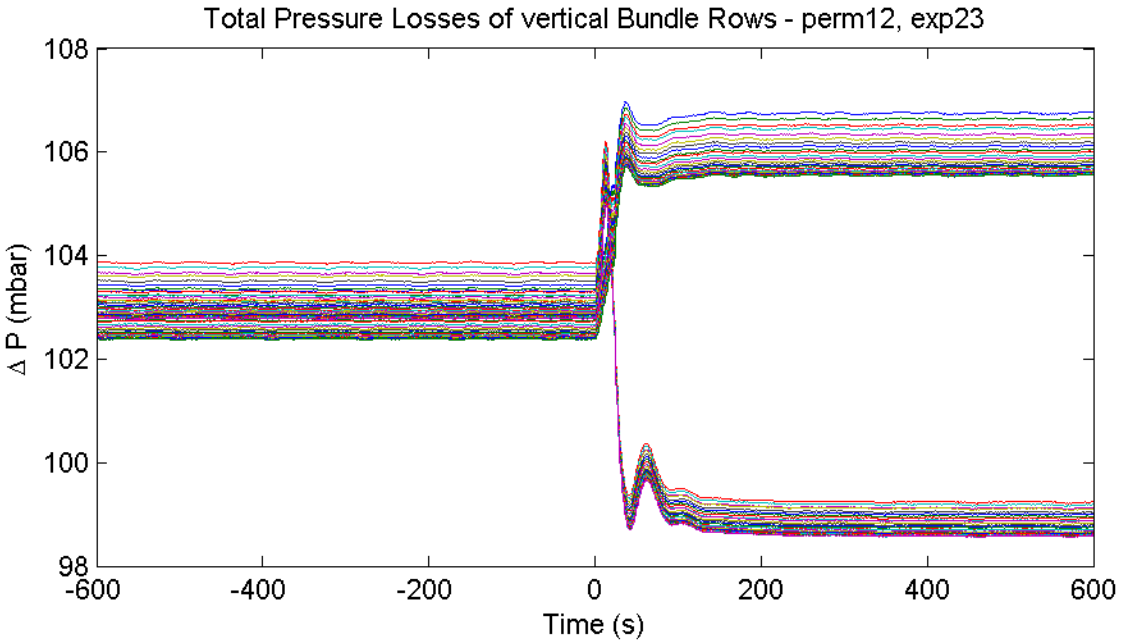

Figure 109: Collective Total Pressure Losses of Bundle Rows – Imperfect Blind Plates, Not Separated Feeding / Rising System, Inlet Gas Temperature 550 °C, Fouling Factor at Section 9.3 set to 0 (10 sec Ramp)

Figure 108 shows the increase of static pressure loss in the tubes of the unheated subsections due to the increase in fluid density. As the heating of this subsection was shut down, the steam quality reduces to 0 and only liquid is present in the subsection, thereby increasing fluid density and static

pressure loss. However, because the steam mass fraction was rather low to begin with, the increase is only about 7 mbar. The lower / higher mass flows in the other subsections increase / decrease their steam mass fractions at constant heat fluxes which slightly decreases / increases their static pressure losses.

Figure 109 shows the total pressure losses (static and friction) between the horizontal headers. Although the total pressure loss on the right side (containing sections 9.3 and 9.4) drops by about 4 mbar to around 99 mbar, it is still above the static pressure difference in the unheated subsection of about 95 mbar (see figure 108). The only way to compensate the additional 4 mbar is by a frictional pressure loss in the same size, which causes the mass flow in section 9.3 despite the absence of heating.

So, the heating of a single subsection is sufficient to cause a pressure difference between the horizontal headers that exceeds the static pressure difference of pure liquid between those headers, creating a mass flow even in completely unheated pipes. This shows that circulating mass flows between vertical rows of the convective evaporator bundle, which would have to be accompanied by an uneven heating of the rows, are very unlikely.

8.2.7 Circulations within a vertical Row

Similarly to the previous chapter, the experiments presented here do not cover very realistic scenarios, but they show that circulations within a vertical row of the convective evaporator bundle are not likely to occur. The following figures show the mass flows in all pipes of the respective (horizontal) row when linearly decreasing the fouling factors of the outermost (1st) or innermost (5th) pipe in the middle of subsection 9.4 to zero over 10 seconds, see figure 59 on page 82 for the configuration.

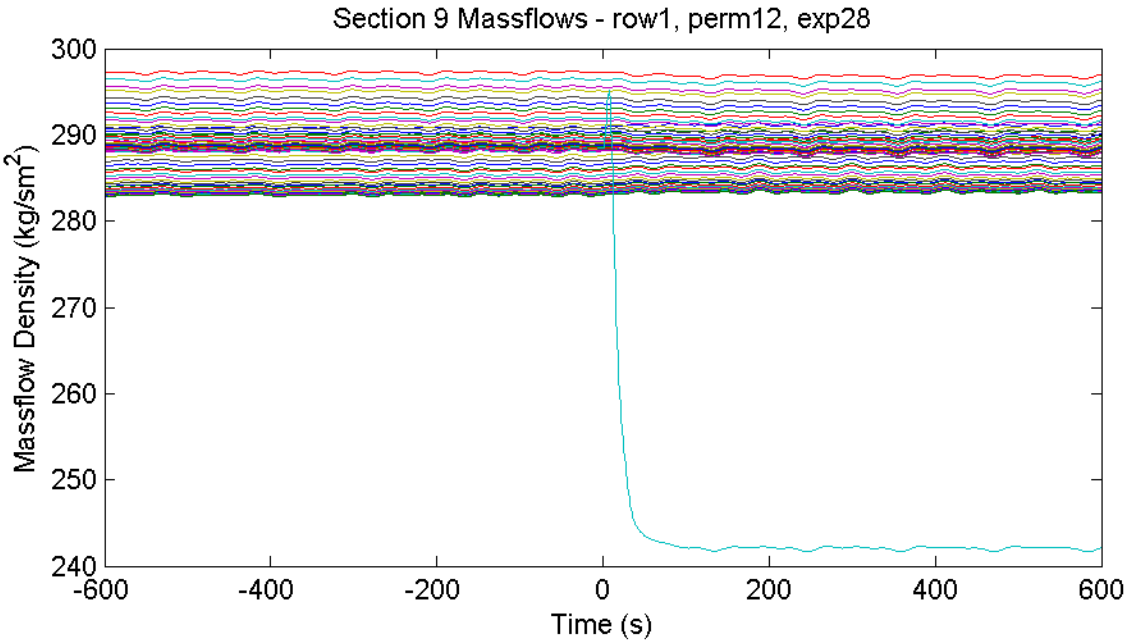

Figure 110: Collective Mass Flow Densities of Bundle Tubes (Row 1) – Imperfect Blind Plates, Not Separated Feeding / Rising System, Inlet Gas Temperature 550 °C, Fouling Factor at Section 9.4.8.1 set to 0 (10 sec Ramp)

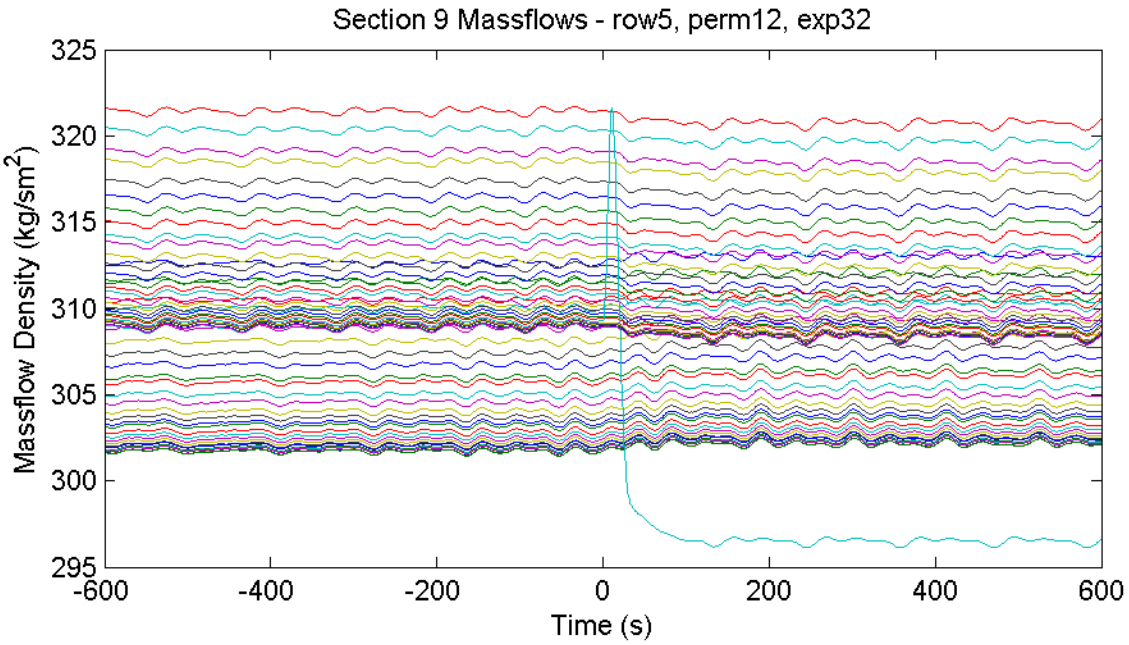

Figure 111: Collective Mass Flow Densities of Bundle Tubes (Row 1) – Imperfect Blind Plates, Not Separated Feeding / Rising System, Inlet Gas Temperature 550 °C, Fouling Factor at Section 9.4.8.5 set to 0 (10 sec Ramp)

The affected sections have the numbers 9.4.8.1 (1st pipe of the 8th vertical row in the 4th subsection of the convective evaporator bundle, figure 110) and 9.4.8.5 (figure 111). One can see that none of the mass flows in any of the affected tubes change direction. Turning off the heating at the innermost pipe (figure 111) barely has any effect at all. Mass flows in other horizontal rows did not show any significant changes. The configuration of the blind plates or the separation of the feeding and rising system does not seem to have any effect on the outcome of the experiments. Experiments at higher inlet gas temperatures at the bundle are very similar as well, accept for the generally higher mass flows.

A look at the absolute pressures in the vertical headers reveals more information, figure 112. It shows the results of turning off the heat flux into the innermost pipe of section 9.4.8, experiment number 32 (same as figure 111).

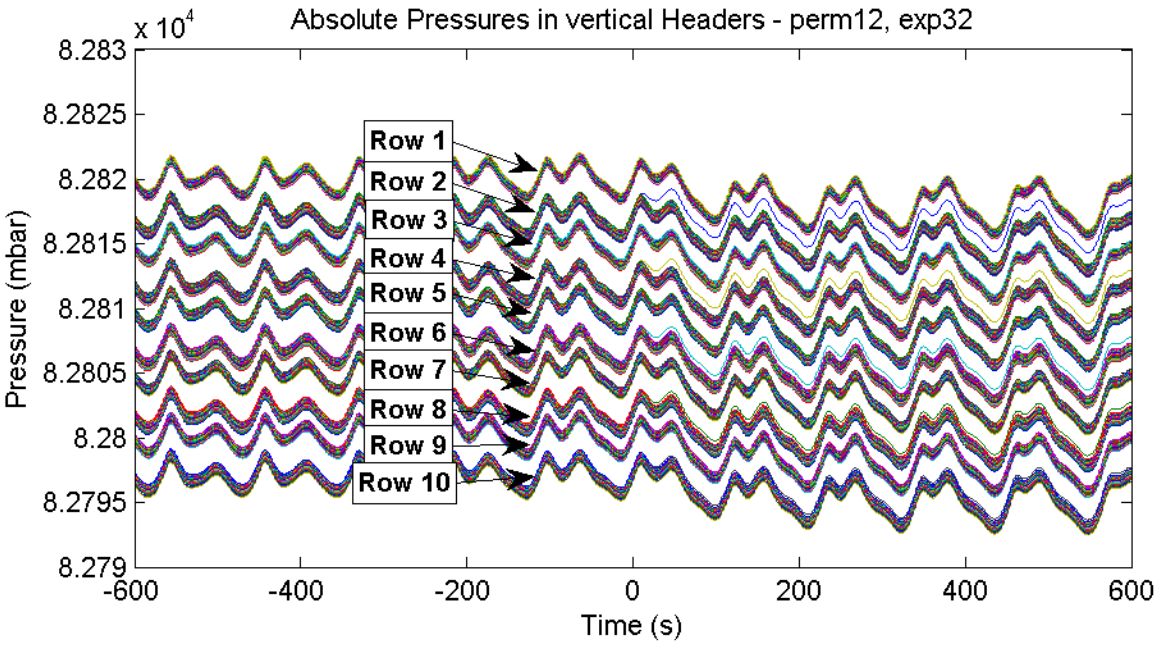

Figure 112: Absolute Pressures in vertical Headers – Imperfect Blind Plates, Not Separated Feeding / Rising System, Inlet Gas Temperature 550 °C, Fouling Factor at Section 9.4.8.5 set to 0 (10 sec Ramp)

The figure shows the absolute pressures inside all vertical headers at their connections to the bundle pipes. As all connections are at slightly different heights, the pressures of connections at the same height all bundle up closely, making the different connections distinguishable from each other: the connections in the bottom (Row 1) have the highest pressure, followed by the connections above them (Row 2), and so on. The rows (heights of connection points) are numbered from bottom to top, which means that the first (outermost) pipes of the bundle are connected between rows 1 and 10, the second pipes between rows 2 and 9, and so on. Also see figure 59 on page 82 or the design drawings for an illustration.

One can see that the pressures at some of the connection points of the affected (vertical) row increase, but all of the lines stay parallel. If one of the mass flows in the bundle tubes changed direction, it would require the pressure gradient between its connection points at the vertical headers to change direction too, meaning that the lines of absolute pressures at the connection points in the graph above would have to cross each other. This is clearly not the case, so mass flows never change direction.

It is interesting to see that the pressures at all connection points of the affected vertical row, not just at rows 5 and 6, have a tendency to increase, none of them decrease. This makes it even harder for lines to cross (mass flows to change direction) and improves stability.

Overall the system is regarded to be stable when it comes to circulations within a vertical row.

9 Discussion and Possible Problem Solutions

The convective evaporator bundle proves to be stable in most scenarios and configurations, as the experiment tables 5 and 8 show. Overheating due to excessive flue gas temperatures is unlikely, since uneven flue gas temperatures did not lead to any flow instabilities (chapter 8.2.1) and actual flue gas temperatures appear to be lower than expected anyway. The influence of any of the residual heat exchangers connected to the same down comers as the convective evaporator bundle is negligible as well (chapter 8.2.3) and should not be of concern.

Drum pressure variations do seem to have a general impact on stability of the steam generator (chapter 8.2.2). Since all experienced instabilities occurred after startups and disappeared again after another startup, and all startups are accompanied by drum pressure variations, they are likely playing a role in the emergence and disappearance of instabilities. However, in the case of lower flue gas temperatures, the influence of drum pressure variations is much smaller.

Lower flue gas temperatures generally do not seem to have a negative effect on stability.

Global circulations were detected during experiments with hot startups (chapter 8.2.4), but they depend on the configuration used: separated feeding and rising systems always lead to a stable status with minimal oscillations, not separated feeding and rising systems always cause heavy oscillations, but they can stabilize themselves as long as the blind plates are perfect and the new bundle geometry is used. The new bundle geometry generally improves the behavior of the system when it comes to suppressing the global circulations.

Besides startups, the new bundle geometry does not lead to significantly different results than the old bundle geometry.

Unfortunately, local instabilities were not detected, although they are likely the cause for the experienced issues. Experiments with foreign objects (chapter 8.2.5) did not reveal any unexpected results or instabilities. Other experiments were unable to create any local flow instabilities between the rows or single pipes (chapters 8.2.6 and 8.2.7).

There are several possible improvements to the evaporator in general and the convective evaporator bundle in particular:

- It is questionable if the convective evaporator bundle is even necessary at all. The usual purpose of such an additional heat exchanger as part of the whole evaporator of the steam generator is to cool down the flue gas sufficiently enough before it reaches any superheaters. The first superheater in the pass after the convective evaporator bundle is already designed to withstand a flue gas temperature at its inlet of 670 °C. If the measurements performed by CNIM are correct and the flue gas temperature at the outlet of the convective evaporator bundle is consistently below 570 °C, that would mean that the

inlet temperature at the bundle is not greater than 610 °C, so already cool enough for the following superheater. If the flue gas temperature goes as low as 500 °C at the inlet of the first superheater (last superheater the steam goes through before it reaches the steam turbine), it could even become problematic to maintain the required steam temperature of 460 °C at the outlet of the steam generator.

As long as fouling at the heat exchangers is not massively lower than expected, it is likely that the intermediate panels in the second pass are simply overpowered, cooling down the flue gas more than expected.

- The results of the hot startup experiments clearly show that a very easy and cost effective solution to avoid any global circulations is separating the main feeding and rising system at its very top and bottom horizontal headers by implementing perfect blind plates (see figure 34 for the respective locations).
- As explained at the end of chapter 8.2.4.1 , the long distance between the two upper horizontal headers and the general design of the very top horizontal header are likely to contribute to instabilities. Reducing the distance between the two or completely removing the very top horizontal header and directly connecting the horizontal header right above the convective evaporator bundle to the steam drum is likely to improve stability.
- The long, unheated section connecting the convective evaporator bundle to the steam drum is problematic in general: such configurations are known to cause density wave oscillations, as explained in chapter 2.3.2 . This problem could be solved by a self-carrying bundle, where the hanger tubes go through the pass a couple of times (building the bundle) before going up the pass and functioning as hanger tubes for all the superheaters. By attaching the horizontal parts to the hanger tubes above the bundle becomes self-carrying. That way, the larger part of the distance to the steam drum would be heated and density wave oscillations become unlikely.

  A self-carrying bundle would also increase mass flow in the tubes due to the higher heating, reducing stratification. This is the most probable cause for the overheating of the tubes.
- It is very likely that density wave oscillations are also the cause for the oscillations in the front side water wall of the first pass (see chapter 7.2). Again, the problem lies in the long unheated section following the heated one. The solution could be to integrate the tubes of the front side water wall into the front water wall of the first pass, which functions as a roof over the grate in the area of the front side water wall. So the front side water wall could transition into the front water wall, which would make the tubes heated for a much longer distance than before and thereby suppress density wave oscillations.

10 Conclusion

Unfortunately, no conclusive evidence was found that could explain the experienced temperature excursions at the tubes of the convective evaporator bundle. They are most likely caused by a stratification of the flow, leaving the top of the tubes poorly cooled. The fairly low Froude numbers showed that stratification is likely to occur, at least during startups. The measurements of tube wall temperatures also showed not severely increased temperatures in most cases, which would be in line with a stratified flow, where major parts of the tube are still wetted and properly cooled which can help cool the hotter parts due to heat conduction.

While Apros takes stratified flow into account when calculating the pressure losses, it does not consider different tube wall temperatures in radial direction due to stratification because tubes are only discretized axially. It was therefore not possible to show the effect of any possible stratification on tube wall temperatures.

However, by transforming the convective evaporator bundle into a self-carrying bundle, it is likely to reduce stratification by forcing a higher mass flow and suppress the temperature excursions.

Even though local instabilities were not directly found, global instabilities were discovered. It could be shown that certain pressure systems such as the one present in the investigated evaporator have a general tendency to be unstable due to their feedback mechanism. Even though the temperature oscillations of the tube walls were too small to be a direct cause for overheating, their frequency is high enough to enhance material fatigue. A simple separation of the feeding and rising system of the bundle was able to remove the problematic pressure system and made the instabilities disappear.

Additional instabilities were discovered at the front side water wall of the first pass. Since they are most likely caused by density wave oscillations due to the long unheated section following the heated part, they could be avoided by integrating the front side water wall into the front water walls of the first pass, removing the unheated part.

11 Bibliography

[1] Helmut Effenberger: *Dampferzeugung*, 2000

[2] Verein Deutscher Ingenieure e.V. (Publ.): *VDI-Wärmeatlas*. 11th Edition, 2013. Chapter L1.

[3] Leonardo Carlos Ruspini, Christian Pablo Marcel, Alejandro Clausse. Two-phase flow instabilities: A review. *International Journal of Heat and Mass Transfer*, **71**, (1): 521–548, 2014

[4] Verein Deutscher Ingenieure e.V. (Publ.): *VDI-Wärmeatlas*. 11th Edition, 2013. Chapter H3.

[5] Katto Y, Ohno H. An Improved Version of the Generalized Correlation of Critical Heat Flux for the Forced Convective Boiling in Uniformly Heated Vertical Tubes. *International Journal of Heat and Mass Transfer*, **27**, (9): 1641-1648, 1984

[6] Heimo Walter. Ein Beitrag zur statischen und dynamischen Stabilität von Naturumlaufdampferzeugern. *Fortschritt-Berichte VDI*, **546**, (6): 13-15, 2006

[7] MVV Energie: *Information about our plant*. https://www.mvvenergie.de/en/uiu/uiu_mvv_environment/ridham_dock/about_our_plant/aboutourplant.jsp (24.07.2016, 12:18)

[8] C. Bonnefoi: *Boiler Thermal Calculation Note*. CNIM Document Number: 47 19 1103/95 I001, 03.10.2013

[9] R. Charreire: *Circulation Issues in Vaporizer Tube Banks*. CNIM Document Number: 7 191102/65 I100, 13.09.2016

[10] Unknown Author: *Boiler Evaporator Leak Ridham*. CNIM Document Number: None (PPT Presentation), 03.11.2015

[11] L. Michel: *Flow Calculations*. CNIM Document Number: 47 19 1103/95 I0002 - F, 29.04.2015

[12] Markku Hänninen, Jukka Ylijoki (VTT Finland): *The Constitutive Equations of the Apros Six-Equation Model*, 2007

[13] DIN Deutsches Institut für Normung e.V. (Publ.): *Gasförmige Brennstoffe und sonstige Gase*. DIN 1871: 1999-05

[14] I.E. Idelchik: *Handbook of Hydraulic Resistance*. Edition 3, 1996.

[15] Verein Deutscher Ingenieure e.V. (Publ.): *VDI-Wärmeatlas*. 11th Edition, 2013. Chapter G7.

[16] Markus Haider: *Thermal Engineering 2* Lecture Notes. 2015. Chapter 3.5.